DOE/DP/40003--T1

MASTER

THEORETICAL STUDIES OF PLASMA TURBULENCE AND HYDRODYNAMIC INSTABILITY IN FUSION TARGETS

by

R. L. Morse

University of Arizona
Tucson, Arizona 85721

November 1979

PREPARED FOR THE

U.S. Department of Energy
Nevada Operations Office

Under Contract DE-AS08-77DP40003

DISCLAIMER

DISCLAIMER

Printed in the United States of America

Available from:

National Technical Information Service
U.S. Department of Commerce
5285 Port Royal Road
Springfield, Virginia 22161

Price: Printed Copy $11.00
Microfiche $3.50

DOE/DP/40003-T1

ACCOMPLISHMENTS AND ACTIVITIES
UNDER CONTRACT DE-AS08-77DP40003,

Theoretical Studies of Plasma Turbulence and Hydrodynamic Instability in Fusion Targets

by R. L. Morse

University of Arizona

Under this contract, which ended November 14, 1979, the following items have been completed or carried to the point of obtaining useful results:

1. Development of the steady-flow model of ablation to include:
   a) Implosion of thin spherical shells
   b) Charged particle beam-driven ablation
   c) Calculation of exhaust velocities for comparison with long pulse experiments and simulations
   d) Inverse bremstrahlung absorption
   e) Ablative flows with critical/sonic point discontinuities for application to low power and/or high Z target cases

2. Calculation of linear instability growth rates in planar and spherical geometry using the steady flow model of ablatively accelerated shells to provide zero-order solutions. Comparisons of results of these calculations with full two-dimensional simulations shown good agreement of instability growth rates.

3. Analytic theory of the maximum ion velocity found in expanding laser-produced plasmas. This work has contributed to an understanding of hot electrons produced by laser light absorption.

4. Development of a triangular zone, two-dimensional hydrodynamics and thermal conduction code for study of the nonlinear development of Taylor instability.

5. Studies with the triangular code (Item 4 above) of the nonlinear development of Taylor instability and the mechanics of large amplitude saturation phenomena. These studies have suggested recently that under some conditions of interest ablation-driven

Taylor instability in ablation-accelerated shells saturates without destroying the integrity of the shell. This area is believed to be very important to the future of the ICF program.

6. Analytic basis of the steady-flow theory of nonlinear saturation of Taylor instability.

7. Analytic theory of the scaling of large compressions ablatively driven by highly shaped pulses.

8. Time development of ablation from the short to long pulse regimes and the identification of a signature of ablation that can be seen experimentally in ion diagnostics. This work, which was done with colleagues at Sandia showed good agreement with Thompson parabola data from long pulse experiments done at Sandia.

9. Inclusion of rates of growth and transport of ion acoustic microturbulence in macroscopic models of laser-produced plasmas. This work contributes to an understanding of flux-limiting phenomena.

10. In addition, the author has helped with various programatic tasks at DOE Laboratories.

Included here as a part of this report are reprints of two papers written under this contract and preprints of two other papers which are to be published.* These papers contain the principal technical results obtained under this contract.

* reprints and preprints removed

JSW 8/15/83

Stationary Flow Model of Ablatively Imploded Spherical Shells

by

L. Montierth and R. Morse
University of Arizona
Tucson, Arizona 85721

Abstract

The stationary flow model of spherical ablation is extended to shells, solutions with a density discontinuity at the critical surface, and charged particle beam driven ablation. Parameter studies of the shell solutions show the relationship between shell aspect ratio, relative ablative mass removal or burn thru, laser power, and shell material type. The discontinuous solutions are shown to occur when the critical surface and sonic surface coalesce. The relationship of these solutions to particular physical situations is shown to be ambiguous in a way that must be resolved by microscopic transport calculations. Charged particle driven ablative implosion processes are shown to resemble laser driven ablation. However, qualitatively different ablation processes occur in different regimes of the power and range of the incident beam. Procedures are described by which stationary solutions can be used to interpret and predict the results of experiments and numerical simulations.

STATIONARY FLOW MODEL OF ABLATIVELY IMPLODED SPHERICAL SHELLS

by
L. Montierth & R. Morse
Department of Nuclear Engineering
University or Arizona
Tucson, Arizona 85721

I. Introduction

Compression by ablation pressure is needed in the implosion process to obtain the large target compression ratios required for inertial confinement fusion (I.C.F.).[1] Ablation applies continuous pressure to the outside of the dense, compressed core of a target in a narrow region called the ablation front which may be thought of as constituting the surface of the core. This continuous ablation pressure compresses the core by causing one or more inward moving shocks and by adiabatic compression, which usually follows the shock compression and heating. By far the most effective schemes for obtaining large compressions use ablative compression of a target consisting of one or more thin spherical shells inside of which there is either a low density gas or a void.[1,2]

Most studies of I.C.F. implosion systems are done with time dependent numerical simulation codes. Such computations are essential to detailed understanding of particular target and pulse systems. However, the large number of different physical phenomena involved makes it difficult to do sufficiently thorough parameter studies to identify and understand regions of optimum performance. Analytic, or at least partially analytic, models of implosion processes can, therefore, be very helpful not only because of the general qualitative insight that they give, but also because the scaling laws that they yield can indicate optimum performance regions. The latter can then be studied in more detail by simulation methods and experimentation.

An additional important use of analytic models of spherically symmetric imploding shells is as a starting point for hydrodynamic stability analysis. Because of their continuous inward acceleration, ablatively imploded thin shells are usually hydrodynamically unstable near the ablation front in a way that is basically the Rayleigh-Taylor instability but is considerably complicated by heat flow. The authors have begun a perturbation analysis of this stability problem using the model of imploding shells presented below as the zeroth order solution.

In a previous paper, Gitomer, Morse & Newberger[3] have developed a stationary flow model of laser driven spherical ablation. The basic assumption of this stationary flow model is that an ablated element of fluid passes through the ablation front, and as far beyond as is necessary for the problem of interest, in a time short compared with the time during which the ablation front moves inward by a significant fraction of its radius. Under these conditions ablation is viewed as coupled stationary heat and fluid flow in the frame of the ablation front. The ablation pressure, mass ablation rate, and other properties of the implosion system are then calculated from the laser power and wavelength, and the stationary energy, momentum and continuity equations. It is shown in that paper that physical solutions that are relevent to I.C.F. can only be obtained in the presence of acceleration, i.e., an effective gravity in the model, and/or the nozzling effect of diverging flow such as is produced by the spherically symmetric geometry that is considered. It is also shown that continuous solutions cannot be obtained in which the critical density, ρ_c, at which the laser energy is deposited, is greater than the density, ρ_s, at the sonic point in the flow.

Numerically integrated solutions of the stationary flow equations are shown for spherically symmetric cases with no inward acceleration. The family of these solutions has two parameters, a parameter M characterizing the ablation front profiles, and ρ_c. This family of solutions shows several approximate scaling laws, including a $\lambda^{-\frac{1}{2}}$ dependence of energy transfer efficiency on laser wavelength, λ, in addition to the exact scaling laws derived from putting the stationary flow equations in dimensionless form. These solutions without the gravity term correspond to implosion cases in which there is no void inside of the target and inward acceleration forces are not significant. It is pointed out that solutions with a gravity term in the momentum equation comparable to or greater than the spherical divergence term correspond to imploding spherical shells; the effect of gravity in the stationary model is to make the density decrease inside of the ablation front.

An analytic solution to the stationary flow equations with gravity has been obtained by Felber[4] with gravity and in the limit of zero spherical divergence by using different approximations in the qualitatively different regions of the flow. This case corresponds to a plane slab accelerated by ablation and is treated below in Section III-C.

The occurrence of stationary flow solutions with density and velocity discontinuities at the critical surface has been shown by C. Max[5]. This work was the beginning point for our work on discontinuous solutions in Section IV below.

This paper extends the development and application of the stationary flow model of ablation driven implosions to treat additional target types and phenomena which are important in I.C.F. The topics treated are:

1) Shell solutions and the relationship between a number of physical parameters of these solutions including shell aspect ratio, absorbed power, ablated mass fraction, critical density and exhaust velocity.

2) Solutions with a discontinuity in density and flow velocity at the critical surface. These solutions occur when the critical density, ρ_c, is made to exceed the sonic density, ρ_s, by reducing laser wavelength and/or absorbed laser power.

3) Solutions representing ablation driven by charged particle beams. It is shown that qualitatively different ablation processes occur in different regimes of the power and range of the incident beam. These differences have no parallel in laser driven ablation.

The subjects of the remaining sections are, by number,

II. Stationary Flow Model Equations and Method of Solution.

III. Shell Solutions and Parameter Studies.

IV. Solutions with Critical Surface Density Discontinuities.

V. Charged Particle Beam Driven Ablation.

VI. Scaling Laws and Applications.

VII. Acknowledgement

This paper differs from the early version, which was presented at the 1977 Anomalous Absorption Meeting in Tucson and appeared as a report, by the addition of the discontinuous solution section (IV), some new material in the charged particle section (V), and the $(A,B,\tilde{g},\tilde{\rho}_p)$ contour diagram analysis in the shell solution section (III).

II. STATIC FLOW MODEL AND METHOD OF SOLUTION

This section contains essentially the same material in the same notation as Section II of Ref. 3, with modifications to accommodate the additional phenomena treated in this paper.

In this model the flow is spherically symmetric, radially outward, and stationary. Stationary flow is a reasonable approximation in most cases of interest because the time required to establish the flow between the pellet surface and the outer, lower density region where most of the incident energy is deposited is less than the characteristic implosion time and because the pressure gradient forces in the ablation region are larger than the forces associated with the average inward acceleration.

A. The Model and Scaling

For our purposes, very little generality is lost and considerable simplicity is gained by assuming a single temperature instead of separate electron and ion temperatures. The steady state hydrodynamic equations are then

continuity:

$$\frac{d}{dr}\ (\rho v r^2) = 0, \tag{1}$$

momentum:

$$\rho v \frac{dv}{dr} = - \frac{dP}{dr} - \rho \frac{d\psi}{dr}, \tag{2}$$

energy:

$$\frac{1}{2} v^2 + \left(\frac{\gamma}{\gamma-1}\right)\frac{P}{\rho} + \psi - \frac{a}{S} K \frac{dT}{dr} - \frac{W}{S} = \frac{1}{2} v_b^2 , \tag{3}$$

where ρ is the fluid mass density, v is the radial fluid velocity, r is the radius, P is the pressure, ψ is the gravitational potential which represents the inward acceleration of a shell, γ is the ratio of specific heats which will be 5/3 in all that follows, $a \equiv 4\pi r^2$ is the cross sectional area, and $v_b^2 (>0)$ is the Bernoulli energy flow

constant. An inward acceleration corresponds to an outward directed gravity $g \equiv -d\psi/dr > 0$. Although in treating the high density part of a shell g might better be taken to increase with r, an increasing g(r) tends to make the lower density region near the sonic point and beyond less realistic. On balance for the calculations presented here, we have chosen $\psi = (r_s - r)g$, where r_s is the sonic radius (see below), with g(r) = constant.

The model requires a non-zero value of v_b^2 to be consistent with the stationary flow from inside the ablation region. However, in cases of interest v_b^2 is much smaller than the values of v^2 which occur in the ablation region and beyond. The term $(a\kappa/S)(dT/dr)$ represents thermal conduction. Here $a \equiv 4\pi r^2$ is the surface area at r, $S \equiv \rho v_a$ is the mass flow rate, a constant of the motion by Eq. (1), T is temperature, and κ is the thermal conductivity coefficient given by

$$\kappa = G(Z) T^{\alpha} \rho^{-\beta}, \tag{4}$$

Here Z is the ion charge number. Following Spitzer[6] we take $\alpha = 5/2$ and $\beta = 0$, where numerical solutions are obtained below.

Although $G(Z) = \kappa_0/Z$ is valid for $Z \gg 1$, and this form will be used in some scaling discussions below, it should be borne in mind that for smaller Z, G(Z) is more complex.[6]

$W(\geq 0)$ is the inward energy flow rate represented by the flux of incident laser radiation or charged particles. In the laser case, in which the incident energy is taken to be deposited at the critical radius, r_c, W increases discontinuously from zero inside r_c to W_∞, the incident laser power, outside of r_c. In the charged particle beam case W increases continuously from zero at the smallest radius which particles reach, to W_∞ as $r \to \infty$.

P is related to ρ and T through the ideal gas equation of state, $P = R\rho T$, where $R \equiv (1+Z)k/m_i$; and k and m_i are the Boltzman constant and ion mass respectively. After some manipulation, Eqs. (1), (2), and (3) become

$$\rho v a = S, \tag{5}$$

$$v\left(1 - \frac{RT}{v^2}\right)\frac{dv}{dr} = RT\left(\frac{2}{r} - \frac{1}{T}\frac{dT}{dr}\right) - \frac{d\psi}{dr}, \tag{6}$$

$$\frac{1}{2}v^2 + \left(\frac{\gamma}{\gamma-1}\right)RT + \psi - \frac{a}{S}\kappa\frac{dT}{dr} - \frac{W}{S} = \frac{1}{2}v_b^2. \tag{7}$$

In the charged particle beam case in which W varies continuously with r, we use the simplified relationship

$$\frac{dW}{dr} = \frac{\rho}{\sigma_\infty}\frac{W_\infty^2}{W} \tag{8}$$

which would be satisfied by a monoenergetic beam of particles with range inversely proportional to energy squared. Here W_∞ is the incident beam power, i.e., the beam power at infinity, and σ_∞ is the range in mass per unit area of the incident particles. A more complex range energy relationship could be used, including such effects as a temperature dependent range or a spread of incident particle energies, but many of the charged particle beam phenomena of interest can be modeled with Eq. (8).

Because transonic solutions are of particular interest to us, it is useful to scale the equations in the following way. Define $\tilde{\rho} = \rho/\rho_s$, $\tilde{T} = T/T_s$, $\tilde{v} = v/v_s$, $\tilde{\psi} = \psi/v_s^2$, $\tilde{g} = gr_s/v_s^2$, $\tilde{W} = 2W/Sv_s^2$, $\tilde{\sigma}_\infty = \sigma_\infty/\rho_s r_s$ where ρ_s, T_s, and v_s are the values of the flow variables at the isothermal sonic point, r_s; that is, at r_s, $v_s = (RT_s)^{\frac{1}{2}}$. Using this scaling, Eqs. (6), (7) and (8) become

$$\frac{d\tilde{v}}{d\tilde{r}} = \frac{1}{\tilde{v}}\left[\frac{\tilde{T}\left(\frac{2}{\tilde{r}} - \frac{1}{\tilde{T}}\frac{d\tilde{T}}{d\tilde{r}}\right) + \tilde{g}}{(1 - \tilde{T}/\tilde{v}^2)}\right] , \tag{9}$$

$$\frac{d\tilde{T}}{d\tilde{r}} = \frac{M\left[\frac{1}{2}(\tilde{v}^2 - \tilde{v}_b^2) + \frac{\gamma}{\gamma-1}\tilde{T} + \tilde{\psi} - \frac{\tilde{W}}{2}\right]}{\tilde{r}^2(1+\beta)\ \tilde{T}^{\alpha}\tilde{v}^{+\beta}} , \tag{10}$$

$$\frac{d\tilde{W}}{d\tilde{r}} = \frac{\tilde{W}_\infty^2\tilde{\rho}}{\tilde{W}\tilde{\sigma}_\infty} . \tag{11}$$

The dimensionless quantity M is defined as

$$M = \frac{r_s\rho_s v_s^3}{\kappa_s T_s} = \frac{r_s\rho_s^{1+\beta} v_s^3}{G(Z)T_s^{1+\alpha}} = \frac{r_s\rho_s^{1+\beta}\ R^{1+\alpha} v_s^{1-2\alpha}}{G(Z)} = \frac{r_s\rho_s^{1+\beta} R^{3/2}}{G(Z)T_s^{\alpha-\frac{1}{2}}} \tag{12}$$

and is the only place in the equations where dimensional parameters appear explicitly.

B. Methods of Integration and Limits on Solution Parameters

The numerical solution of Eqs. (9), (10) and (11) is accomplished by integrating inward ($\tilde{r}<1$) and outward ($\tilde{r}>1$) from the singularity of Eq. (9) at $\tilde{r} = 1$. The flow is seen to be supersonic for $\tilde{r}>1$ and subsonic for $\tilde{r}<1$, except that there is in general a second sonic point, $\tilde{r}_{s2}$, between $\tilde{r} = 0$ and $\tilde{r} = 1$. However, the stationary flow model is not applicable at radii this small and smaller. We will discuss this point below in connection with specific solutions of Eqs. (9), (10) and (11). In the solutions that are continuous at $\tilde{r} = 1$, $d\tilde{v}/d\tilde{r}$ is finite there. Thus, since the value of the denominator of the right-hand side of Eq. (9) becomes zero at $\tilde{r} = 1$, the numerator must also be zero there.

The value of the temperature derivative at $\tilde{r}=1$ must then be

$$d\tilde{T}/d\tilde{r}\Big|_{\tilde{r}=1} = 2 - d\tilde{\psi}/d\tilde{r}\Big|_{\tilde{r}=1} = 2 + \tilde{g}, \tag{13}$$

and from Eq. (13) and Eq. (10) a relationship between $\tilde{v}_b^2$ and M is obtained;

$$M = \frac{2+\tilde{g}}{(1-\tilde{v}_b^2)/2 + \eta - \tilde{W}_s/2}, \tag{14}$$

where $\eta=\gamma/(\gamma-1)$, and $\tilde{W}_s$ is the value of $\tilde{W}$ at $\tilde{r}=\tilde{r}_s=1$, which is only non zero for those charged particle beam cases in which particles penetrate inside of r_s. In order to obtain values of $d\tilde{v}/d\tilde{r}$ at the singular point, $\tilde{r}=1$, to begin the inward and outward integrations, L'Hospital's rule is applied there and with Eq. (11) gives

$$\frac{d\tilde{v}}{d\tilde{r}}\Big|_{\tilde{r}=1} = \frac{1}{4}\left[-B+(B^2-8C)^{\frac{1}{2}}\right] \tag{15}$$

where $B = M - (1+\beta)(2+\tilde{g})$

$$C = (2+\tilde{g})\left[M\eta-4-2\beta-\alpha(2+\tilde{g})\right] - M\left(\frac{\tilde{W}_\infty^2}{2\tilde{W}_s\tilde{\sigma}_\infty}\right) + 2$$

C differs slightly from Ref. 3 because different forms of ψ are used. In those cases in which $\tilde{W}_s=0$, $d\tilde{W}/d\tilde{r}=0$, and the $\tilde{W}_\infty^2/2\tilde{W}_s\tilde{\sigma}_\infty$ term in C above, which comes from Eq. (11), is absent.

Limits When $\tilde{W}_s=0$

When $\tilde{g}=0$ the lower limit on $\tilde{v}_b^2$ is zero, and it will be seen that this limit corresponds to vanishingly small specific entropy and, therefore, infinite density at the pellet surface. However, when $\tilde{g}>0$ the net energy in the flow at the sonic point must be greater than zero if it is to have the limiting zero value at the pellet surface because the fluid falls through a difference in potential, ψ, (Eq.(7)) between the shell and the sonic point. The lower limit on $\tilde{v}_b^2$ is

then determined by setting $\tilde{v}_b^2/2$ equal to this potential energy difference. Consequently for $\tilde{g}>0$ the lower, $\tilde{v}_{bL}^2(\tilde{g})$, is of the form $0<v_{bL}^2(\tilde{g})\ \tilde{v}_b^2$. Values of $\tilde{v}_{bL}^2(\tilde{g})$ cannot be known a priori because the distance between the pellet surface and the sonic point must be found by solving Eqs. (9), (10), and (11). Values of $\tilde{v}_{bL}^2$ will be found below in practice by seeking the lowest value of $\tilde{v}_b^2$ for a given $\tilde{g}$ for which solutions exist. The upper limit on $\tilde{v}_b^2$ is set in principle by the requirement that $d\tilde{v}/d\tilde{r}>0$ at $\tilde{r}=1$. From Eq. (15), this is equivalent to $C<0$, or

$$M< \frac{(2+\tilde{g})\ [4+2\beta+\alpha(2+\tilde{g})]\ -2}{2\eta+\tilde{g}(\eta-1)\ -\ \dfrac{\tilde{W}_\infty^2}{2\tilde{\sigma}_\infty \tilde{W}_s}} \tag{16}$$

Therefore, from Eq. (14)

$$\left.\begin{array}{ll}\tilde{g}=0, & 0\\ \tilde{g}>0, & \tilde{v}_{bL}\end{array}\right\} <\tilde{v}_b^2<1\ +\ 2\left\{\eta-\tilde{W}_s/2\ -\ \frac{(2+\tilde{g})\ \left[2\eta+\tilde{g}(\eta-1)-\dfrac{\tilde{W}_\infty^2}{2\tilde{\sigma}_\infty \tilde{W}_s}\right]}{(2+\tilde{g})\ [4+2\beta+\alpha(2+\tilde{g})]\ -2}\right\} \tag{17}$$

For the parameter values $\alpha=5/2$, $\beta=0$, $\gamma=5/3$ so that $\eta=5/2$, $\tilde{g}=0$, and $\tilde{W}_s=0$, Eq. (17) gives $0<\tilde{v}_b^2<19/4$. For the same values except for $\tilde{g}=1$, $\tilde{v}_b^2<24/5$. For the same values except for $\tilde{g}=\infty$, $\tilde{v}_b^2<24/5$. These upper limit values of $\tilde{v}_b^2$ are equivalent to the convective energy flow from the origin being a major fraction of the convective energy flow through the sonic point (see Eq. 7). Hence it will not be surprising that in cases for which these parameter values are representative the upper limit values of $\tilde{v}_b^2$ will not be of physical interest and are in fact near the burn through, or exploding pusher, limit where the concept of ablation does not apply.

Limits When $\tilde{W}_s \neq 0$

In those particle beam cases in which $\tilde{W}_s > 0$, a slightly different situation occurs. The upper limit values of $\tilde{v}_b^2$ can be of interest because the upper limit can be much less than one and can in fact go to zero, for the following reason. It is unphysical to have $M<0$ because from Eq. (12) it can be seen that this is equivalent to $\tilde{\kappa}_s<0$. Thus the limiting physical case is $\kappa_s \to +0$, $M \to +\infty$. From Eq. (14), $M < +\infty$ is equivalent to

$$\tilde{v}_b^2 < 1 + 2\eta - \tilde{W}_s . \tag{18}$$

Consequently, since $0 < \tilde{v}_{bL}^2 < \tilde{v}_b^2$, where $\tilde{v}_{bL}^2 = 0$ for $\tilde{g}=0$, (recall that $\tilde{v}_{bL}^2(\tilde{g})$ is the physical lower limit on $\tilde{v}_b^2$ for a given value of $\tilde{g}$), solutions only exist when

$$\tilde{W}_s \leq 2\eta + 1 - \tilde{v}_{bL}^2 \qquad = 6 \text{ when } \gamma = 5/3 \text{ and } \tilde{g} = 0. \tag{19}$$

Equation (19) will, therefore, be an upper limit on the particle energy flux through the sonic point in charged particle beam driven ablation. In general the upper limit given by Eq. (18), for particle beam driven cases, i.e.,

$$\tilde{W}_s = 1 - \tilde{v}_b^2 + 2\eta \tag{20}$$

will be seen to correspond to the interesting type of ablative flow in which thermal conduction plays no role ($M = +\infty$, $\kappa_s = 0$) and all energy is transported by convection and the particle beam. From Eqs. (14) and (18), as well as on intuitive grounds, for such flows to occur the beam particles must penetrate inside r_s, i.e., $\tilde{W}_s > 0$.

C. Distinguishable Intervals in $\tilde{r}$ for Laser and Particle Cases and Determination of $\tilde{W}_\infty$, $\tilde{W}_s$, $\tilde{r}_R$ and $\tilde{v}_\infty$

In the case of laser deposition, the incident power, W_∞, which is deposited at r_c, is adjusted to give a solution $T(r)$ which approaches 0 as r approaches infinity (see asymptotic solutions in Ref. 3, Sec. III). Since $d\tilde{T}/d\tilde{r}$ is positive at r_s and negative beyond r_c, laser deposition must always occur at, or at radii larger than, the isothermal sonic radius. In those laser cases

discussed below in which there is a discontinuity in ρ and v at r_c, this is still essentially true but some modifications in detail are required.

There are four distinguishable intervals in $\tilde{r}$ in the laser cases;

1. $r_{s2} < \tilde{r} < \tilde{r}_p$; $\tilde{r}_p$ is the point at which $d\tilde{v}/d\tilde{r} = 0$

and is the point which is to be identified with the pellet surface. In most cases because $d\tilde{v}/d\tilde{r}$ is a strong function of $\tilde{r}$ near $\tilde{r}_p$, and $\tilde{S} = \tilde{r}^2 \tilde{\rho} \tilde{v} = 1$, $\tilde{r}_p$ is very close to the point of maximum $\tilde{\rho}$ in a shell. Heat flow is not very important in this region.

2. $\tilde{r}_p < \tilde{r} < 1$. This is the subsonic part of the ablation front.

3. $1 < \tilde{r} < \tilde{r}_c$; asymptotic solutions can be obtained when $\tilde{r}_c$ approaches infinity (see Ref. 3) and are helpful in interpreting numerical solutions when $\tilde{r}_c >> 1$. This interval disappears in those cases in which $r_c \to r_s$ and a discontinuity occurs at r_s.

4. $\tilde{r} > \tilde{r}_c$; the asymptotic solutions in this region (Ref. 3) for $\tilde{r} \to \infty$ indicate that $T \to 0$ is the proper boundary condition. Values of the jump in $\tilde{W}$ from 0 to $\tilde{W}_\infty$ at $\tilde{r} = \tilde{r}_c$ are adjusted to satisfy this condition. Values of the asymptotic, or exhaust velocity, $\tilde{v}_\infty$ are obtained from the numerical integration for the case $\tilde{g}=0$.

In the charged particle beam cases there are also four distinguishable intervals in $\tilde{r}$. The interval scheme involves the radius r_R defined to be the end point of the particle trajectories, which is determined by the range, σ_∞ (see Eqs. (8) and (11)). The first interval, the adiabatic flow regime $\tilde{r}_{s2} < \tilde{r} < \tilde{r}_p$, is the same as interval (1) in the laser case above. If $\tilde{r}_s < \tilde{r}_R$, ie., $1 < \tilde{r}_R$, the rest of the intervals are also similar to the laser case. Intervals (2) and (3) are the same as in the laser case except that the outer end of interval (3) is $\tilde{r}_R$ instead of $\tilde{r}_c$, ie., interval (3) becomes $1 < \tilde{r} < \tilde{r}_R$. Interval (4) is then $\tilde{r}_R < \tilde{r}$, and the solution procedure here is analogous to that in the

laser case. Eq. (11) is integrated outward together with Eq. (9) and (10) starting from $\tilde{W}=0$ at the chosen point $\tilde{r} = \tilde{r}_R$. The ratio $\tilde{W}_\infty/\tilde{\sigma}_\infty$, is adjusted to give a solution that satisfies the boundary condition $\tilde{T} \to 0$ as $\tilde{r} \to \infty$. This can be shown to be a physical boundary condition from a large $\tilde{r}$ asymptotic solution which is similar to that obtained for the laser case, Eq. (13d) in Ref. 3,

$$\tilde{v}^2 = \tilde{v}_\infty^2 + \tilde{v}_m^2 \tilde{r}^m, \qquad \tilde{v}_m^2 < 0 \tag{21}$$

$$\tilde{T} = \tilde{T}_m \tilde{r}^m, \qquad \tilde{T}_m < 0$$

$$\tilde{W} = \tilde{W}_\infty + \tilde{W}_m \tilde{r}^{-1}, \qquad \tilde{W}_m < 0$$

where $$m = -\frac{(1+2\beta)}{(1+\alpha)}$$

$$\tilde{T}_m = \left[\frac{M(\tilde{v}_\infty^2 - \tilde{v}_b^2 - \tilde{W}_\infty)}{2m\ \tilde{v}_\infty^{2\beta}}\right]^{\frac{1}{(1+\alpha)}}$$

$$\tilde{v}_m^2 = \frac{2(2-m)}{m}\tilde{T}_m$$

$$\tilde{W}_m = -\frac{\tilde{W}_\infty}{\tilde{v}_\infty^2\ \tilde{\sigma}_\infty}$$

and $\tilde{v}_\infty$ is the limiting value of $\tilde{v}$ as $\tilde{r} \to \infty$. Both $\tilde{W}_\infty$ and $\tilde{v}_\infty$ are obtained as results of the integration.

In the event that $r_R < r_s$, ie., $\tilde{r}_R < 1$, the solution procedure is different. A value of $\tilde{W}_s$ is chosen, consistently with Eq. (18), and Eq. (11) is integrated inwards and outwards from the singularity at $\tilde{r}=1$, together with Eqs. (9) and (10). Again $\tilde{R}_s$ is adjusted to give the boundary condition $\tilde{T} \to o$ ar $\tilde{r} \to \infty$. The asymptotic solutions, Eq. (21), are also applicable in this case. Values of $\tilde{r}_R$, $\tilde{W}_\infty$ and, when $\tilde{g}=0$, values of $\tilde{v}_\infty$ are obtained as results of the inward and outward integrations. In the particular zero heat flow case in which $\tilde{v}_b^2$ has the limiting value in Eq. (18) and consequently, $M=\infty$ (or $\kappa_s = 0$), it will be seen that $\tilde{r}_R = \tilde{r}_p$. That is, the beam particles penetrate all the way through the ablation front, as they must because they provide all of the inward energy transport

III. SHELL SOLUTIONS AND PARAMETER STUDIES

In the laser case only Eqs. (9) and (10) are used, together with the form of W(r) that specifies total energy deposition at $\tilde{r} = \tilde{r}_c$,

$$W = 0, \quad \tilde{r} < \tilde{r}_c \qquad (22)$$
$$= W_\infty (>0), \tilde{r} > \tilde{r}_c .$$

The family of solutions of this system has three parameters $\tilde{\rho}_c \left(\equiv \rho_c / \rho_s \right)$, $\tilde{g}$, and a third parameter which was taken to be M in Ref. (3). However when we vary $\tilde{g}$, the allowed range of M changes, and M becomes a less informative parameter. Instead of M, which primarily characterizes the flow in the region $\tilde{r}<1$, we will use as the third parameter $\tilde{\rho}_p \left(\equiv \rho_p / \rho_s \right)$. The interesting range of $\tilde{\rho}_p$ is typically from about 10 up to 10^3. For smaller values the ablation rate is so large that the ablation front structure becomes indistinct and the stationary flow approximation becomes less applicable.

A. $\tilde{g} = 0$

Figures 1a and 1b show linear and logarithmic profiles of the case $\tilde{\rho}_p = 10^2$, $\tilde{g} = 0$, for various values of $\tilde{\rho}_c$. This solution is typical of those presented in Ref. (3). The second sonic point is on the left at $\tilde{r}_{s2} = 0.305$. For comparison, Fig. 1c shows logarithmic profiles for the case $\tilde{\rho}_p = 10$ and $\tilde{g} = 0$. Note that in this case $\tilde{v}_b^2$ and, correspondingly, the specific entropy of the dense pellet material are larger than in the $\tilde{\rho}_p = 10^2$ case. Figure 2 shows various ratios of quantities at $\tilde{r}_p$ and $\tilde{r}_s$ ($\equiv 1$), and other characteristics of the ablation region, for the $\tilde{g} = 0$ family of solutions. These properties are independent of $\tilde{\rho}_c$ because $\tilde{r}_c > 1$. The quantity $\tilde{m}$ is the dimensionless mass between r_{s2} on the left side of a shell and a given point $\tilde{r}$, and is defined as

$$\tilde{m} \equiv m/4\pi\rho_s r_s^3 \equiv \frac{1}{\rho_s r_s^3}\int_{r_{s2}}^{r} dr\, r^2\rho = \int_{\tilde{r}_{s2}}^{\tilde{r}} d\tilde{r}\,\tilde{r}^2\tilde{\rho} \qquad (23a)$$

The quantities $\tilde{m}_p$ and $\tilde{m}_s$ are the masses between r_{s2} on the left and r_p and r_s respectively;

$$\tilde{m}_p \equiv \tilde{m}(\tilde{r}_p),\ \tilde{m}_s \equiv \tilde{m}(\tilde{r}_s). \qquad (23b)$$

The stationary model approximation to the shell mass is, therefore, $\tilde{m}_p$. The additional mass in $\tilde{m}_s$ is mass in the ablation region which has already been removed from the shell. It will be seen that for small values of $\tilde{g}$, i.e., $\tilde{g} < 1$, $(\tilde{m}_s - \tilde{m}_p)/\tilde{m}_p \ll 1$. That is, the amount of mass at any time in the ablation region between the maximum density and sonic points, r_p and r_s is relatively small. For larger $\tilde{g}$, on the other hand, it will be seen that more than a third of the mass between r_{s2} and r_s is between r_p and r_s. This part is expected to be significant for the Taylor instability problem because the instability develops in the ablation region and additional mass there should reduce the growth rate.

A related quantity, $\Delta\tilde{r}$, which will be used below in connection with $\tilde{g}\neq 0$ solutions, is the dimensionless shell thickness defined as

$$\Delta\tilde{r} \equiv \frac{m_p}{4\pi r_s r_p^2 \rho_p} = \frac{\tilde{m}_p}{\tilde{\rho}_p \tilde{r}_p^2} \qquad (24)$$

Note from Fig. 2 that $\tilde{P}_p/\tilde{P}_s$ and $\tilde{r}_p$ $(\equiv r_p/r_s)$ are nearly independent of $\tilde{\rho}_p$ $(\equiv \rho_p/\rho_s)$ i.e., nearly the same for all members of the family of solutions. Also $\tilde{m}_p$ is nearly proportional to $\tilde{\rho}_p$ as would be expected for, $\tilde{g}=0$. By contrast in the $g \neq 0$ solutions shown below shell mass is nearly independent of $\tilde{\rho}_p$ for a given $\tilde{g}$ and larger values of $\tilde{\rho}_p$.

Figure 3 shows ratios of various quantities at $\tilde{r}_s (\equiv 1)$ and $\tilde{r}_c$ as a function of $\tilde{\rho}_c$. Also included is the dimensionless laser power $\tilde{W}_\infty$, required to support a given solution. Curves are given for several widely spaced values of $\tilde{\rho}_p$, except where the curves are indistinguishable. It is clear that except near $\tilde{\rho}_c = 1$ these quantities are essentially independent of the details of the ablation front, and, therefore, of the value of $\tilde{\rho}_p$. It can be seen that $\tilde{W}_\infty$ is approximately proportional to $\tilde{\rho}_c^{-\frac{1}{2}}$, which is to say proportional to laser wavelength, λ. This point has been confirmed by numerical simulation.[7] Figure 3 is essentially the same as Fig. 2 in Ref. (3) except for $\tilde{v}_\infty \equiv v_\infty / v_s$, the exhaust velocity, which was not shown there. The flow velocity approaches this value as $r \to \infty$ in a manner much like the exhaust of a rocket. This, therefore, is the blow off velocity that should be seen by an external ion detector such as a Faraday cup[8] or Thompson parabola analyzer, when target conditions are such that the ablation is essentially stationary. Of course, incident laser power, W_∞, is a function of time and so, therefore, is v_s and ρ_s, and therefore, $\tilde{\rho}_c (\equiv \rho_c / \rho_s)$. Consequently neither v_s nor $\tilde{v}_\infty$ will be constant throughout a target shot. However, it is shown below that T_s and, therefore, v_s are weak functions of W_∞, and it is seen in Fig. 3 that $\tilde{v}_\infty$ is a weak function of ρ_c / ρ_s. It should, therefore, be expected that in experiments in which approximately stationary ablation occurs, the ion blow off spectrum will have a clear peak in velocity. From Fig. 3 the peak should occur somewhere between $4 < v_s >$ and $8 < v_s >$, depending on ρ_c, where $< v_s >$ is a time averaged sonic velocity which will be near the value of v_s at peak power.

It may be noted that because of the scaling chosen ($\tilde{W}_\infty \equiv W_\infty/(Sv_s^2/2)$ and $\tilde{v}_\infty \equiv v_\infty/v_s$), if there were no convective internal energy transport as $r \to \infty$, then energy conservation would require $\tilde{W}_\infty = \tilde{v}_\infty^2 - \tilde{v}_b^2$. Since in most cases of interest $\tilde{v}_\infty^2 >> \tilde{v}_b^2$, we should expect to find $\tilde{W}_\infty = \tilde{v}_\infty^2$, but from Fig. 3 this is clearly not so except for larger $\tilde{\rho}_c$, i.e., smaller $\tilde{r}_c$. The reason for this can be shown from the asymptotic solutions given in Ref. 3 to be the perhaps surprising fact that there is a finite outward heat flow as $\tilde{r} \to \infty$. This heat flow loss to infinity increases as $\tilde{r}_c$ increases and is the cause of the fact that $\tilde{W}_\infty$ increases faster than $\tilde{v}_\infty^2$ with decreasing $\tilde{\rho}_c$, i.e., increasing $\tilde{r}_c$. This same effect occurs in the charged particle beam driven case and is discussed below in connection with Fig. 16.

B. $0 < \tilde{g} < \infty$

The contributions of spherical divergence and acceleration to the momentum equation, Eq. (9), are the $2\tilde{T}/\tilde{r}$ and $\tilde{g}$ terms respectively. In the ablation region, $\tilde{r}_p < \tilde{r} < 1$, the divergence term typically increases smoothly from close to zero at $\tilde{r}_p$, where $0 < \tilde{T} << 1$, to 2 at $\tilde{r} = 1$, where $\tilde{T} = 1$ (see Figs. 1 and 4). The influence of acceleration on the ablation process should then be comparable to the nozzling effect of spherical divergence when $\tilde{g} \simeq 1$. Figures 4a and b show profiles of the case $\tilde{\rho}_p = 10^2$, $\tilde{g} = 1.0$, for various values of $\tilde{\rho}_c$. The second sonic point is at $\tilde{r}_{s2} = 0.85$. Note the shell like structure of the density profile. Figure 5a shows the ablation region parameters for the $\tilde{g} = 1.0$ family of solutions. In addition to the parameters given in Fig. 2 for the $\tilde{g} = 0$ family, Fig. 5 gives the quantity $(\tilde{r}_s - \tilde{r}_p)/\Delta\tilde{r}$, which is the ratio of the distance between the maximum density point, $\tilde{r}_p$, and the sonic point to the thickness of the shell, $\Delta\tilde{r}$ (Eq. (24)). It will be seen that for a given $\tilde{\rho}_p$ this ratio increases significantly with increasing $\tilde{g}$.

In order to show the effects of different values of $\tilde{g}$, the ablation region parameters for $\tilde{g} = 10^{-\frac{1}{2}}$ and $10^{+\frac{1}{2}}$ are given in Figs. 5b and 5c respectively. Figure 6 shows the various critical to sonic ratios and other quantities which depend on $\tilde{\rho}_c$ for $\tilde{g} = 1.0$. The blow off velocity, $\tilde{v}_\infty$, given for $\tilde{g} = 0$ in Fig. 3 is not given here for the reason that $\tilde{g} = \text{const} \neq 0$ makes this quantity diverge in our calculations. Values of $\tilde{v}_\infty$ for $\tilde{g} \neq 0$ could be obtained from the steady flow model by making $\tilde{g}$ decrease to zero with increasing $\tilde{r}$. However, by comparing Figs. 3 and 6 it can be seen that behavior between the sonic and critical points is not very different for $\tilde{g} = 0$ and for $\tilde{g} = 1.0$, even for small $\tilde{\rho}_c$ and the correspondingly large values of $\tilde{r}_c$. Moreover the implosion velocities of shells are usually somewhat less than the ablation exhaust velocity.

Consequently the exhaust velocities given in Fig. 3 for $\tilde{g} = 0$ are a good approximation to these for imploding shells except for very large $\tilde{g}$ and/or very small $\tilde{\rho}_c$. Graphs like Fig. 6 of $\tilde{\rho}_c$ dependent quantities are not shown here for other values of $\tilde{g}$ except for very large values of $\tilde{g}$ (see the $\tilde{g} = \infty$ section below) since they are very similar to the $\tilde{g}$=1 curves shown in Fig. 6. The values of the shell mass, $\tilde{m}_p$ (Eq. 23)) and the shell surface pressure and radius, $\tilde{P}_p$ and $\tilde{r}_p$, shown in Fig. 5 can be seen to be almost constant in the range of interest, which is to say for $\tilde{\rho}_p \gtrsim 10$. This is especially true for $\tilde{g} = 10$ and $10^{+1/2}$. Over the same range the shell aspect ratio, which is given the usual definition

$$A \equiv \frac{r_p}{\Delta r} = \frac{\tilde{r}_p}{\Delta \tilde{r}} \qquad \text{(See Eq. (24) for } \Delta\tilde{r}\text{)} \qquad (25)$$

increases approximately in proportion to $\tilde{\rho}_p$. This behavior can be seen in Fig. 7 which shows A as a function of $\tilde{\rho}_p$ for various values of $\tilde{g}$. The linear dependence of A on $\tilde{\rho}_p$ for large $\tilde{\rho}_p$ has a simple explanation. When A is sufficiently large, the inward acceleration of the thin, dense shell of mass m_p (Eq. (23) and below) which lies between r_{s2} and r_p can be calculated by treating the shell as if it were a sheet mass. That is, for this purpose spherical corrections can be neglected. The equation of motion is then

$$m_p g \simeq 4\pi r_p^2 P_p , \qquad (26)$$

where the right side is the inward force on the outside surface of the shell and g is the magnitude of the inward acceleration. Applying the various definitions and scaling relationships above, including Eqs. (24), (25) and the fact that $P_s = \rho_s v_s^2$, gives

$$\tilde{m}_p \simeq \frac{\tilde{r}_p^2 \tilde{P}_p}{\tilde{g}} \quad , \quad (27a) \qquad A = \frac{\tilde{r}_p \tilde{\rho}_p \tilde{g}}{\tilde{P}_p} \quad (27b)$$

Since as seen above $\tilde{P}_p$ and $\tilde{r}_p$ are weak functions of $\tilde{\rho}_p$ for large $\tilde{\rho}_p$ the independence of $\tilde{m}_p$ and the approximate linear relationship between A and $\tilde{g}$ for large $\tilde{\rho}_p$ follows. Equation (27) can be seen to agree with Figs. 5 and 7 for large $\tilde{\rho}_p$. On the other hand it was shown above that for $\tilde{g}$ of the order of one, or less, spherical divergence effects in the ablation region are comparable to or larger than acceleration effects. Thus we see that a shell can be so thin that its spherical geometry can be neglected in calculating its acceleration, while at the same time spherical effects are very important in determining the ablation pressure which derives that acceleration. It can, therefore, be incorrect to assume that a shell can be treated as planar because its aspect ratio is large.

C. $\tilde{g} = \infty$

When $\tilde{g} \to \infty$, Eqs. (9) and (10) are simplified by the absence of various spherical divergence corrections. Under these conditions the aspect ratio $A \to \infty$ (see Eq. (27)), and r_s can no longer be used as a scale length. Instead the length, x_g,

$$x_g \equiv v_s^2/g \quad (28)$$

must be used, so that the dimensionless length is $\tilde{x} \equiv r/x_g$. With these changes and the origin of $\tilde{x}$ taken to be the sonic point, Eqs. (9-12) become

$$\frac{d\tilde{v}}{d\tilde{x}} = -\frac{\frac{d\tilde{T}}{d\tilde{x}} - \tilde{g}}{\tilde{v}(1-\tilde{T}/\tilde{v}^2)} \quad (29)$$

$$\frac{d\tilde{T}}{d\tilde{x}} = \frac{M[\frac{1}{2}(\tilde{v}^2 - \tilde{v}_b^2) + \eta\tilde{T} + \tilde{\psi} - \frac{\tilde{W}}{2}]}{\tilde{T}^{\alpha}} \tag{30}$$

$$\frac{d\tilde{W}}{d\tilde{x}} = \frac{\tilde{\rho}}{\tilde{W}R_s} \tag{31}$$

$$M = \frac{x_g \rho_s v_s^3}{\kappa_s T_s} \tag{32}$$

This system is planar. If g is taken to be independent of position then $\tilde{\psi} = -\tilde{x}$ and $\tilde{g} = 1$ in this scaling. An approximate analytic solution to this system has been obtained by Felber[4]. Figure 8 shows the spatial profiles of the planar solution with $\tilde{\rho}_p = 10^2$, plotted log/linear because there is now no natural origin to the left of the shell. The $\tilde{g} = 1.0$, $\tilde{\rho}_p = 10^2$ profiles are included (dashed lines) in the x_g based units for comparison. Note that the sonic point is further from the shell, in units of $\Delta\tilde{x}$, and there is relatively more mass in the ablation region in the planar case. Figure 9 gives the ablation region parameters, which show these same features for the range of $\tilde{\rho}_p$ values, when compared to Fig. 5. Figure 10 shows the $\tilde{\rho}_c$ dependent parameters for the planar case and should be compared to Fig. 6.

The $\tilde{g} \to \infty$ limit is an appealing simplification and is sometimes useful for treating large aspect ratio shells. However, this limit neglects spherical divergence effects, and, as noted above in the discussions of aspect ratios, this is not always a good approximation.

D. Range of Validity of Stationary Flow Model of Shells

In order for the stationary flow model of an inward accelerating shell to be valid, the effects of the fictitious outward flow from inside the shell

should be small. Since the stationary model breaks down at the second sonic point, r_{s2}, where in general the density is much less than the maximum density at r_p, this point has been taken as the inside edge of the shell. A measure of the validity of the model is the ratio of the pressure at r_p to the pressure at r_{s2}, P_p/P_{s2}. If the ratio is large, the pressure at the inside edge, which should in reality be zero, has only a small effect on the inward acceleration and related structure of the shell. Figure 11 shows this ratio as a function of $\tilde{\rho}_p$ and $\tilde{g}$. The minimum values of P_p/P_{s2} that are acceptable depend on the particular application and the accuracy required; for most purposes the authors feel that the pressure ratio should satisfy $P_p/P_{s2} \gtrsim 4$. For $\tilde{g} = 1.0$ for example, it is seen from Fig. 11 that this is equivalent to saying that the model is only valid for $\tilde{\rho}_p > 10$. For smaller $\tilde{g}$ the minimum $\tilde{\rho}_p$ is seen to be larger.

Such restrictions on P_p/P_{s2} should not be applied to modeling those implosion situations in which $\tilde{g} = 0$ because there is a significant material density and pressure at $r = 0$. Such situations occur, for instance, in the compression of initially homogeneous solid spheres by highly shaped pulses[9]. The $\tilde{g} = 0$ solutions presented above and in Ref. 3 are a limiting case of this class of solutions.

E. Burn Through

Up to this point the removal of mass from a shell by ablation during an implosion has not been considered. As a measure of mass removal we define a burn through parameter, B,

$$B \equiv \frac{\Delta m_A}{m_p} = \frac{S\Delta t_I}{m_p} \tag{33}$$

where Δm_A and Δt_I are the mass removed from a shell by ablation during its implosion and the duration of the implosion respectively. Recall that $S = 4\pi r_s^2 v_s \rho_s$ is the mass flow rate and $m_p = m(r_p)$ is the shell mass. If it is assumed that the shell starts from the radius r_p and accelerates uniformly to the origin with an average acceleration g, then Δt_I is given by

$$\Delta t_I = \left(\frac{2r_p}{g}\right)^{1/2}. \tag{34}$$

Substituting Eq. (34) and the necessary scaling definitions including Eq. (23) into Eq. (33) gives

$$B = \frac{1}{\tilde{m}_p}\left(\frac{2\tilde{r}_p}{\tilde{g}}\right)^{1/2}. \tag{35}$$

Figure 12 shows B vs. $\tilde{\rho}_p$ for various values of $\tilde{g}$. The approximate constancy of B for large $\tilde{\rho}_p$ is a consequence of the approximate constancy of $\tilde{m}_p$ for large $\tilde{\rho}_p$ (see Eq. (27) and above).

Substituting Eq. (27a) for $\tilde{m}_p$ into Eq. (35) for B gives the asymptotic value of B for large $\tilde{\rho}_p$, and therefore large A;

$$B = \left(\frac{\tilde{g}}{\tilde{r}_p^2 \tilde{P}_p}\right)\left(\frac{2\tilde{r}_p}{\tilde{g}}\right)^{1/2} \tag{36}$$

Equation (36) can be seen to be in agreement with Fig. 12 when the weakly $\tilde{\rho}_p$ dependent values of $\tilde{r}_p$ and $\tilde{P}_p$ from Fig. 5 are taken into account.

There are many ways in which Eq. (34) can be refined and/or made more complicated, including in particular greater acceleration for a given incident power as the shell mass is reduced by ablation. Most of these will make Δt_I, and

therefore, B, smaller for a given $\tilde{g}$ and $\tilde{\rho}_p$, but most will not reduce B by much more than a factor of 2. The inclusion of values of B larger than 1 in Fig. 12 makes adjustment for such corrections possible by simply sliding the logarithmic B scale by an amount equal to the correction factor.

The efficiency of an ablatively driven implosion depends on the ratio of ablatively removed mass to final imploded mass in essentially the same way as the efficiency of a rocket depends on the fuel to payload mass ratio[10]. The greatest energy is given to the imploded shell if its mass is about 1/e times the total initial shell mass. This would be equivalent to B=1-1/e = 0.63, but when the various corrections to Δt_I including increasing acceleration as the shell mass decreases, the B scale may move up by as much as a factor of 2. The optimum would then be about where B = 1.0 on the scale in Fig. 12.

In any case within the range of likely implosion time histories, it is seen from Fig. 12 that values of $\tilde{g}$ larger than about $10^{\frac{1}{2}}$, and certainly as large as 10, correspond to too much mass removal, i.e., essentially complete burn through, for any $\tilde{\rho}_p \gtrsim 10$. Moreover, for $\tilde{\rho}_p \lesssim 10$ there appear to be no solutions with acceptably small values of B, which is consistent with the previous observation that stationary ablative behavior does not occur for $\tilde{\rho}_p \leq 10$.

If physical requirements are placed on A and B, the regions in $\tilde{\rho}_p$ and $\tilde{g}$ where acceptable solutions exist, if any, can be seen from comparing Figs. 7 and 12 or by use of Fig. 13 (see further discussion of Fig. 13 in Section VI) which give A and B as functions of $\tilde{\rho}_p$ and $\tilde{g}$. For example if Taylor stability considerations require that $A \lesssim 10$, while efficiency requires $0.5 < B < 1.0$, then there is a region near $\tilde{g} = 0.1$ and $\tilde{\rho}_p = 60$ where appropriate solutions are found.

IV. Solutions With Critical Surface Density Discontinuities

A. Jump Conditions, Existence of Solutions and Profile Modification

In addition to the continuous solutions discussed above, there are ablative stationary flow solutions which contain a discontinuity in density and velocity at the critical radius, r_c. These solutions can be derived from the continuous solutions above by invoking continuity of mass and momentum flow at the discontinuity. Since the discontinuity is at the critical surface and the laser light impinges from the right (large r), the density to the right of the discontinuity must be less than or equal to ρ_c and the density to the left must be equal to or larger than ρ_c. If the subscript 1 identifies quantities to the left (smaller r) of the discontinuity and subscript 2 to the right, then $\rho_1 \geq \rho_c \geq \rho_2$ and the continuity conditions are

$$\rho_1 v_1 = \rho_2 v_2 = S/a, \tag{37a}$$

$$\rho_1 v_1^2 + P_{p1} = \rho_2 v_2^2 + P_{p2} + P_R \tag{37b}$$

Here $a = 4\pi r_c^2$ is the surface area at r_c, S is the mass flow rate, P_p is the plasma pressure and P_R is the pressure of the incident laser radiation which is only non-zero on the low density side of r_c. By taking P_R to be discontinuous at r_c we are neglecting structure on the scale of the laser wavelength. The plasma pressure is

$$P_{p(1,2)} = \mathcal{R}\rho_{(1,2)} T_c = \rho_{(1,2)} C_c^2 \tag{38}$$

where C_c is the isothermal sound speed at r_c, and there is only one temperature, T_c, at r_c because T must be continuous where the thermal conductivity, κ, is non-zero. Substituting Eqs. (37a) and (38) into (37b) gives

$$v_1 + \frac{C_c^2}{v_1} = v_2 + \frac{C_c^2}{v_2} + \frac{P_R a}{S} . \tag{39}$$

Solving for v_2 gives

$$v_2 = \tfrac{1}{2}\left[\left(v_1 + \frac{C_c^2}{v_1}\right) - \frac{P_R a}{S}\right] \pm \left\{\left[\left(v_1 + \frac{C_c^2}{v_1}\right) - \frac{P_R a}{S}\right]^2 - 4C_c^2\right\}^{\frac{1}{2}} \quad (40)$$

In cases where P_R is negligible, this gives

$$v_2 = \begin{cases} C_c^2/v_1 \ (= RT_c/v_1), & (-\text{sign}) \\ v_1, & (+\text{sign}) \end{cases} \quad (41)$$

Since $\rho_2 < \rho_1$ and, $v_2 > v_1$, if $v_1 \neq v_2$, i.e., if a discontinuity does occur, then the root corresponding to the (-) sign, Eq. (41), applies, and $v_1 < C_c < v_2$. That is, in going from $r<r_c$ to $r>r_c$ the flow changes from subsonic to supersonic across any stationary discontinuity which occurs at r_c. Discontinuous supersonic to supersonic transitions are not possible under these conditions. When the laser wavelength, λ, is 1.06 μm of the Nd glass laser, the critical electron density is $n_{ec}=10^{21}\text{cm}^{-3}$. If the critical surface temperature is a typical 10^3eV, then the critical surface electron pressure is 1.6×10^{12} dynes/cm^2. By contrast, if the incident power is a typical 10^{15} W/cm^2, then (neglecting the plasma dielectric effects near r_c) $P_R \approx 3\times10^{11}$ dynes/cm^2, and the radiation pressure is small though not necessarily insignificant compared to P_p. However if λ=10.6 μm from a CO_2 laser, then $n_{ec} = 10^{19}\text{cm}^{-3}$ and under the same other conditions P_R is larger than P_p.

The value of v_2, given by Eq. (40) with the (-) sign, can be seen to be reduced by non-zero values of P_R, since P_R, S and a are all positive. Consequently for a given v_1 and ρ_1, the effect of increasing the radiation pressure, P_R, from zero is to reduce v_2 and increase ρ_2, i.e., to reduce the magnitude of the discontinuity.

It happens in many cases of interest where ρ_c is small enough to allow P_R to be important that the flow at the critical surface is far above sonic. In such cases it can be seen from Eq. (40) that stationary discontinuities which satisfy the necessary condition $\rho_2<\rho_1$ do not exist. The effect of non-zero P_R to the right of r_c in stationary solutions is to increase ρ, not to decrease it. Consequently, density profile modifications which are caused by radiation pressure to the right of a critical surface in the supersonic flow region and which introduce a sharp decrease in density with increasing r at the critical surface would seem to be transient. Since the instant effect of applying P_R to the right of r_c must be to decrease ρ there, and the position of r_c changes with changes in the profile of ρ, oscillatory transients should be expected when P_R is sufficiently large. When such density oscillations occur in a supersonic region, they must be convected with the flow to larger r and not be felt to the left of r_c. The profile modifications seen by Virmont[11] may be of this type.

B. Role of Discontinuous Solutions and Relationship of ρ_c to ρ_1 and ρ_2

A particular reason for interest in the discontinuous solutions is that situations can occur in which the isothermal sonic point density falls below the laser light critical density, ρ_c. This tends to occur when the mass ablation rate is decreased as a result of decreasing the incident power and/or decreasing the conductivity coefficient, G(Z), of the target by increasing Z. For example for a given target density, ρ_p, which might be the initial density multiplied by a shock jump ratio of about 4, consider a set of cases with the same critical density but progressively smaller incident laser power, W, or conductivity coefficient, G. The sonic density,

ρ_s, decreases with decreasing W or G. That is $\tilde{\rho}_p(\equiv\rho_p/\rho_s)$ increases with decreasing W or G. This can be seen from Figs. 2 and 3 or 5 and 6 above and will be discussed in more detail in the scaling laws section below. When W or G are sufficiently small, $\rho_s = \rho_c$. If W or G are decreased still further, no continuous stationary solutions exist because, as shown in Ref. 3, continuous stationary solutions do not exist with $\rho_s<\rho_c$. However, discontinuous solutions do exist with a given ρ_p and ρ_c and an arbitrarily small W or G. These solutions are, therefore, needed to complete the description of laser driven ablation phenomena.

In cases in which there is a stationary discontinutiy at r_c, P_R is usually small if not negligible compared with P_p. This may be seen from the particular examples of P_p and P_R given above by recalling from Ref. 3 that the critical surface pressure falls more slowly than the absorbed power. That is, the dependence of critical surface pressure on absorbed power is weaker than linear. On the other hand P_R is proportional to incident power which usually falls at least as rapidly as absorbed power because the absorption fraction tends to increase with decreasing power. Consequently as incident power decreases and the critical point approaches the sonic point, $P_R/P\ (r_c)$ decreases and P_R is, for example, even less important than in the 10^{15} W/m^2, λ = 1.06μm example above. This argument is stronger for longer wavelengths. In what follows the corrections introduced by the P_R terms in Eq. (40) will be dropped because the effect of P_R is usually small and because retaining P_R would introduce the complication of another scaling parameter. The jump conditions then reduce to Eq. (36) and Eq. (41) which give a relationship between (ρ_1,v_1) and (ρ_2,v_2) that depends only on C_c $(=\sqrt{RT_c})$.

At this point the problem appears to be ill posed. Equations (9) and (10) (momentum and energy respectively) can be solved with the jump conditions

Eqs. (36) and (41), replacing the treatment of the sonic singularity described in Section II. However, a definite relationship between ρ_c and ρ_1 or ρ_2 is needed to relate these solutions to physical problems, and all that is available is $\rho_1 \geq \rho_c \geq \rho_2$ (Section IV-A above). There are several approaches to obtaining this relationship. These include:

1) some minimization argument to indicate the relationship,

2) a microscopic treatment of the flow through the discontinuity, or

3) time dependent numerical simulation.

We will consider each of these three approaches in turn and see that a complete solution to the problem requires additional information about the laser energy deposition process.

1) Minimization arguments. It is interesting to ask what relationship between ρ_c and ρ_1 will support a given pressure and density on the high density side, P_1 and ρ_1, with the minimum input power W. Alternatively one could ask what relationship gives the greatest P_1 for a given ρ_1 and W. In either case the answer is $\rho_c = \rho_2$, that is, the critical density occurs on the low density side of the step. This can be seen by moving to the laboratory frame where the fluid to the left of r_c is static and that immediately to the right has the velocity U. Then, if T_c is the critical surface temperature, the pressure balance relationship across the discontinuity is

$$P_1 = R\rho_1 T_c = \rho_2 U^2 + R\rho_2 T_c = \rho_2 (U^2 + c_c^2). \qquad (42)$$

The power that must be supplied to produce the flow energy is

$$W = \frac{\rho_2 U^2}{2} = \frac{\rho_2}{2}\left(\frac{P_1}{\rho_2} - c_c^2\right) \qquad (43)$$

where the second equality comes from substituting Eq. (42). From Eq. (43), if P_1 is held fixed, $(\partial W/\partial \rho_2)<0$. The minimum value of W consistent with a given ρ_c is, therefore, obtained when ρ_2 has the largest possible value. Since it is necessary that $\rho_2 \leq \rho_c$ to have a discontinuous solution, the minimum W is required when $\rho_2=\rho_c$. By a similar argument it can be shown that the largest possible ρ_2 namely $\rho_2=\rho_c$, also gives the maximum possible pellet side pressure, P_1, for a given W. These arguments can be seen to be forms of familiar rocket impulse and efficiency relationships. Unfortunately, while they suggest that $\rho_2=\rho_c$ should be used, they do not prove it, and in fact the suggestion may be misleading in some cases.

2) Microscopic treatment of the flow through the discontinuity. The discontinuity is discontinuous because of the assumption that laser energy deposition occurs only where $\rho=\rho_c$. If instead the deposition is taken to occur over a small range on either side of r_c, then the discontinuity becomes a thin region with large but finite density and velocity gradients and with T essentially constant at $T=T_c$. In general part of the deposited laser power leaves this region by thermal conduction just as in the continuous solutions. However, the remainder of the deposited power is converted directly into streaming energy by doing work against the rapidly expanding fluid. This process, which occurs at almost constant temperature, converts this part of the absorbed laser energy directly into kinetic energy of streaming without first converting it into thermalized internal energy. This conversion must, therefore, occur on a length scale of the order of the mean free path of the primary electrons, those which initially acquire the absorbed energy. If because of relative length scales the absorption can be regarded as occurring only at $\rho=\rho_c$, then when viewed on the microscopic scale the discontinuity must have a thickness of the

order of a primary electron mean free path. This is clearly reminiscent of the role of mean free paths in shock front structure. On the other hand the thickness of the discontinuity could simply be determined by the spread about ρ_c of the values of ρ_c at which absorption occurs. A consequence of the direct conversion is lower values of T_c than would occur if absorbed energy were first converted into thermalized internal energy.
The reduction of T_c that accompanies discontinuity formation is discussed further in Section IV-C below. Because of the lower density of the discontinuity, ρ_2, can be no less than the lowest density at which direct conversion can occur, ρ_2 could be as large as ρ_c, depending on details of the absorption and direct conversion process. Thus $\rho_c=\rho_2$ is possible. However, it is clear that the finite range of primary electrons could require that $\rho_c>\rho_2$. To resolve the relationship between ρ_c and ρ_2, it will, therefore, be necessary to solve the microscopic transport problem in the vicinity of r_c.

3) Time dependent numerical simulation. Time dependent hydrodynamic and heat flow simulations have been done with parameter values which give discontinuous solutions.[12] These simulations do show a quasi-stationary discontinuity in the form of a step a few zones wide. Within zone structure resolution these solutions show $\rho_2 = \rho_c$. These calculations were done with the prescription which deposits the absorbed laser energy in the outer most zone with $\rho>\rho_c$ i.e., the first over dense zone encountered by the laser beam, which is the prescription used in most laser fusion codes. Consequently direct conversion in zones with $\rho\leq\rho_c$ is not possible in the simulation. Since the stationary solution requires $\rho_c\geq\rho_2$, $\rho_c = \rho_2$ is to be expected in such simulations if a quasi-stationary discontinuity does develop. What is significant from the simulations is that such discontinuous solutions are seen to develop and to be stable.

A different energy deposition procedure could be incorporated in the simulations which would allow direct conversion at densities below ρ_c, but this would need to be based on some microscopic model of transport processes near r_c. To illustrate the properties and scaling of the family of discontinuous solutions, solutions with $\rho_2 = \rho_c$ are shown in the next section. We expect that $\rho_2 = \rho_c$ will be a good approximation in most but not necessarily all cases of interest in laser fusion research.

C. Numerical Solutions and Scaling

Because the sonic velocity in discontinuous solutions occurs between v_1 and v_2 (see Eq. (41)), sonic point values of r, ρ and v are not natural values by which to scale the solutions. Instead we scale ρ, r, and v by r_c ρ_2 and v_2, and T by (v_2^2/R). That is, we define $\tilde{r} \equiv r/r_c$, $\tilde{\rho} \equiv \rho/\rho_2$, $\tilde{v} \equiv v/v_2$ and $\tilde{T} \equiv T/(v_2^2/R)$. T could have been scaled by T_c, but this could give the misleading impression that v_2 is the sonic velocity at r_c. That this scaling singles out the density ρ_2 is consistent with the view discussed above that ρ_2 is the most likely value of ρ_c. However, the solutions obtained here do not assume any particular relationship between ρ_c and ρ_2.

For a given g, r_c, ρ_2 and v_2, if P_R is neglected there is a two parameter family of discontinuous solutions. The two parameters are

1) The isothermal mach number, defined as $M_I \equiv v_2/(R\,T_c)^{\frac{1}{2}} = \tilde{T}_c^{-\frac{1}{2}}$.

2) The pellet surface density, $\tilde{\rho}_p$.

Notice from Eq. (41) that ρ_1/ρ_2 $(\equiv\tilde{\rho}_1)$ is determined by M_I. Combining the definition of M_I and Eqs. (36) and (41) gives

$$\frac{\rho_1}{\rho_2} = \frac{v_2}{v_1} = \frac{v_2^2}{RT_c} = M_I^2 = \frac{1}{\tilde{T}_c} \quad . \tag{44}$$

Note that $M_I \geq 1$. While $\tilde{\rho}_1$ is determined by M_I, $\tilde{v}_b^2$ in Eq. (10) can be varied and give different values of $\tilde{\rho}_p$ for a given $\tilde{\rho}_1$. M in Eq. (10) is not now determined by $\tilde{v}_b^2$ through the requirement of continuity at the sonic singularity. However, for $r<r_c$ the discontinuous solutions are the same one parameter family as the continuous solutions for $r<r_s$ because of the common physical requirement that the solution approach adiabatic flow with decreasing $\tilde{r}$. Consequently the relationship between M and $\tilde{v}_b^2$ is the same as in the continuous solutions.

Figure 14a shows two discontinuous solutions with $\tilde{g}=0$ and $M_I=2$ but different values of $\tilde{\rho}_p$. Note that the discontinuities in $\tilde{\rho}$ and $\tilde{v}$ satisfy Eq. (44). The family of solutions has only one parameter, M_I, for $r>r_c$ and two parameters, M_I and $\tilde{\rho}_p$, for $r<r_c$. By contrast the family of continuous solutions have one parameter, $\tilde{\rho}_p$, for $r<r_s$ and two parameters, $\tilde{\rho}_p$ and $\tilde{\rho}_c$ for $r>r_s$.

The shell solutions with $\tilde{g}\neq 0$ described in Section III above can be modified by a discontinuity at r_c just as shown here for $\tilde{g}=0$.

Figure 14b shows a dimensionless variable which is linear in T_c, as well as several quantities which characterize the discontinuity, including the step ratio, ρ_1/ρ_2, plotted as a function of a dimensionless variable which is proportional to $(G(Z)W^{4/3})$. This is done for two rather different values of ρ_p/ρ_c within the range of interest for laser fusion applications. It is seen from Fig. 14b that for values of the independent variable less than about 50 a discontinuity occurs. In making this figure it was assumed that when a discontinuity occurs, $\rho_2=\rho_c$. Hence the notation $\rho_{(c,2)}$. As explained above $\rho_2=\rho_c$ is possible but is nevertheless an arbitrary assumption. However, if instead $\rho_2<\rho_c$, then the variable that is proportional to T_c would fall even faster in the discontinuity region with decreasing values of the independent variable. Consequently, it will develop that the points which are made below with regard to Fig. 14b would only be strengthened if $\rho_2<\rho_c$.

Now take the view that the pellet radius, r_p, and $\rho_{(c,2)}$ are held constant while G(Z) and/or W change. The independent variable is then $(GW^{4/3})$, except for a constant multiplier, and the variable containing T_c becomes $(T_cW^{-2/3})$, except for a constant multiplier. It is then seen that, as discussed above in Section IV-A, as G(Z) and/or W decrease, $[T_cW^{-2/3}]$ increases, the critical

point approaches the sonic point until they coalesce, and a density discontinuity occurs. As $(GW^{4/3})$ decreases further, $(T_c W^{-2/3})$ at first continues to increase slightly and then decreases sharply.

If W is also held constant, then the situation is particularly simple, with increasing Z and, therefore, decreasing conductivity coefficient, G(Z), T_c increases until a discontinuity occurs and then, after a slight further increase begins to decrease rapidly. That the critical surface temperature, T_c, should increase at first as thermal conduction into the ablation region from the critical surface is restricted by decreasing G(Z) is not at all surprising. As G(Z) decreases further, T_c decreases and a discontinuity occurs in which direct conversion becomes significant, this is perhaps more interesting and may have important consequences in some applications.

If on the other hand, G(Z) is held constant while the laser power, W, is allowed to change, the relationships are a little more complicated because the W dependence in the dependent quantity $(T_c W^{-2/3})$ must be considered. It can be seen that T_c is everywhere an increasing function of W, as would be expected. In particular, on the right side of Fig. 14b in the $\rho_c<\rho_s$ regime where the curve representing $(T_c W^{-2/3})$ has the most negative slope, from the slope of this curve and the W dependence of the independent and dependent variables, the relationship between T_c and W is approximately $T_c \sim W^{1/3}$. Elsewhere, particularly in the density discontinuity regime, T_c is a more strongly increasing function of W.

Figure 14b shows, therefore, that T_c is a very strong function of laser power and the thermal conductivity coefficient, W and G(Z), in the range of parameters in which density discontinuities exist. In addition, while T_c is everywhere an increasing function of W when G(Z) is held fixed, when W is held

fixed T_c decreases with increasing G(Z) when there is no density discontinuity but increases with increasing G(Z) when there is a discontinuity of sufficient size. This latter result would mean, for instance, that increasing Z to decrease G(Z), and therefore, to increase T_c would only be effective to a point and T_c would reach a maximum and begin decreasing if Z were increased further.

V. Charged Particle Beam Driven Ablation

Profiles generated by charged particle beam driven ablation are shown in Fig. 15. Figures 15a, b, and c all have M chosen to give $\tilde{\rho}_p = 10^2$, have $\tilde{g} = 0$, and differ in having respectively $\tilde{\sigma}_\infty = .48$, .81 and .92 respectively. Recall from Section II that $\tilde{\sigma}_\infty$ is the charged particle range (in mass per unit area) at incident particle energy. In these three cases the terminal point of the particle trajectories, $\tilde{r}_R$, can be seen to be respectively a) outside the sonic point at about $\tilde{r}_R = 1.3$, b) approximately midway between r_ρ and r_s at about $\tilde{r}_R = 0.97$, c) very close to $\tilde{r}_\rho$ at about $\tilde{r}_R = \tilde{r}_\rho = 0.93$. In all cases the profiles of the laser and charged particle driven systems are identical at radii less than both r_c and r_R because the inward energy flow is transported entirely by thermal conduction. The case shown in Fig. 15c in which the beam penetrates all of the way through the ablation front to r_p is an example of the interesting limiting behavior described by Eq. (20) in which all inward energy flow is transported by the beam and thermal conduction plays no role. In such cases the scaling constraints imposed on implosion systems

by the temperature and Z dependence of thermal conductivity are removed. This, for instance, could allow design of systems of larger radius with lower temperatures than would be possible if electron thermal conduction were needed to transport energy into the ablation region. This limiting class of solutions would, therefore, seem to provide some potentially useful flexibility in the use of charged particle beam implosion drivers.

Notice also that the beam power, $\tilde{W}$, approaches larger values at large $\tilde{r}$ as $\tilde{r}_R$ increases. $\tilde{W}$ was defined in Section II to be $\tilde{W} \equiv 2W/Sv_s^2$. This is similar to the increase of $\tilde{W}_\infty$ with $\tilde{r}_c$ which was shown in Ref. 3 and in Section III above in the case of laser driven ablation. The basic cause in both cases is that input beam power deposited further from the ablation region must be transported further through outward flowing material before reaching the ablation region and contributing to the ablation process. The energy flow is attenuated along this transport path by conversion into hydrodynamic flow energy. Thus with increasing $\tilde{r}_c$ or $\tilde{r}_R$, the exhaust velocity, $\tilde{v}_\infty$, increases, as seen above in Fig. 3 and below in Fig. 16. Also, as can be demonstrated from the asymptotic solutions given by Eq. 21 above, there is a finite outward heat flow as $\tilde{r}\to+\infty$. This heat flow loss increases with increasing $\tilde{r}_c$ or $\tilde{r}_R$ and is responsible for the fact that $\tilde{W}_\infty$ increases faster than $\tilde{v}_\infty^2$ with increasing $\tilde{r}_c$ or $\tilde{r}_R$. (Recall that $\tilde{W}_\infty \equiv W_\infty/(Sv_s^2/2)$ and $\tilde{v}_\infty \equiv v_\infty/v_s$ so that if there were no internal energy or heat flow as $\tilde{r}\to\infty$, then energy conservation would require $\tilde{W}_\infty = \tilde{v}_\infty^2 - \tilde{v}_b^2$, which for most cases of interest $\tilde{v}_\infty^2 >> \tilde{v}_b^2$.). Consequently to support a given ablation region structure, more input beam energy must be supplied if the beam energy is deposited further from the ablation region.

The quantities $\tilde{W}_\infty$ and $\tilde{v}_\infty$, $\tilde{W}_s$, the value of $\tilde{W}$ at $\tilde{r} = 1$ ($r=r_s$) as well as, $\tilde{r}_R$ and the material flow velocity at ($\tilde{r}_R$, $\tilde{v}_R$) are shown as a function of $\tilde{\sigma}_\infty$ in Fig. 16. Curves are shown for two very different values of $\tilde{\rho}_p$, which show very little dependence of these quantities in $\tilde{\sigma}_\infty$, except at the longer

range end of the scale. Note that $\tilde{r}_R < 1$, i.e., that the particle trajectories terminate inside the sonic point, only for $\tilde{v}_\infty$ greater than about 0.7. Also, for the larger value of $\tilde{\rho}_p$, which is representative of cases of interest for inertial confinement fusion, the maximum possible value of $\tilde{v}_\infty$ is about 1.

The meaning of this maximum value of $\tilde{v}_\infty$ is that as the particle energy, and, therefore, range, is increased, while $\tilde{\rho}_p$ ($\equiv \rho_p/\rho_s$) is held fixed, the incident beam power, $\tilde{W}_\infty$, decreases as described above until the limiting, most efficient case is reached. If the range is increased then $\tilde{\rho}_p$ must decrease. If ρ_p is held fixed then ρ_s must increase. The decrease of $\tilde{\rho}_p$ with increasing range would continue until, as discussed in Ref. 3 and Section II, the flow could no longer be described as ablation.

VI. Scaling Laws and Applications

In order to apply the solutions obtained above to the interpretation and prediction of experiments and numerical simulations it is necessary to identify the solution that corresponds to a particular set of physical parameters. This can be done by calculating the parameter M, Eq. (12), with the values of physical parameters at the pellet surface, r_p, instead of the sonic point r_s. From Eq. (12) this dimensionless constant, M_p, is

$$M_p = \frac{r_p \rho_p^{1+\beta} v_p^3}{G(z)\, T_p^{1+\alpha}} = \frac{r_p \mathcal{R}^{(\alpha+1)} \rho_p^{(\alpha+\beta+1/2)}}{G(z)\, P_p^{(\alpha-1/2)}} \qquad (45)$$

$$= M \frac{\tilde{r}_p \tilde{\rho}_p^{(\alpha+\beta+1/2)}}{\tilde{P}_p^{(\alpha-1/2)}} .$$

M_p is plotted as a function of $\tilde{\rho}_p$ ($\equiv \rho_p/\rho_s$) for $\alpha = 5/2$, $\beta = 0$, and $g = 0$, 1, $10^{-1/2}$ and $10^{+1/2}$ in Figs. 2, 5a, 5b, 5c respectively. To identify a solution, substitute values of r, ρ and P at the pellet surface, and the gas constant $\mathcal{R}$ and conductivity coefficient G(Z) (Eq.(4)) of the target material into the second equality of Eq.(45). In those cases in which inward acceleration is negligible, which includes most solid ball cases,

$\tilde{g}$ can be taken to be zero and the corresponding stationary flow solution can be identified from Fig. 2 with the calculated values of M_p.

Note that as the conductivity coefficient G(Z) increases with r_p, ρ_p and P_p held fixed, from the second equality in Eq. (45), M_p decreases and from Fig. 2 $\tilde{\rho}_p (\equiv \rho_p/\rho_s)$ decreases. Therefore, since G(Z) decreases with increasing Z, for a given r_p, ρ_p and P_p the sonic density, ρ_s, decreases with increasing Z. While it can be seen similarly that v_s increases with increasing Z, the mass ablation rate, $S=4\pi r_s^2 \rho_s v_s$, also decreases with increasing Z, while T_s increases. This should be expected. As conductivity decreases with increasing Z, heat flow into the pellet is reduced and less material is removed for a given incident power. However, what mass is removed must convect away a greater energy per unit mass and must, therefore, have a higher velocity and temperature.

Similarly, Figs. 2 and 5 show that if the pellet radius, surface density and conductivity coefficient, r_p, ρ_p and G(Z), are held constant while the pellet pressure, P_p, is decreased, the sonic density ρ_s decreases. Consequently for fixed ρ_c, ρ_c/ρ_s increases, and it therefore follows from Figs. 3 and 6 (critical surface parameters) that both the dimensionless and the physical laser powers, $\tilde{W}$ $(\equiv 2W/4\pi r_s^2 \rho_s v_s^3)$ and W , decrease. That is, if pellet density and material type are held fixed while pellet pressure is decreased, then the sonic point density and the required laser power decrease. Looked at another way, if the pellet material and density are held fixed while the incident power is decreased, then the sonic density, ρ_s, decreases. Thus ρ_s decreases with either increasing Z or decreasing W .

As discussed above in Section IV on discontinuous solutions, this decrease in ρ_s with decreasing W or increasing Z can continue until $\rho_s=\rho_c$. At that point the solutions become discontinuous at r_c if W decreases or Z increases further. This behavior can be

expected to occur in practice with decreasing W or increasing Z because pellet surface density, ρ_p, is usually a weak function of these parameters. For instance ρ_p might be the initial material density multiplied by a hypersonic shock density ratio of about 4.

When ρ_s has been determined from Fig. 2, then from the critical density, ρ_c, ρ_c/ρ_s is obtained. With ρ_c/ρ_s and Fig. 3 for $\tilde{g}=0$, or Fig. 6 for $\tilde{g}\neq 0$, properties of the solution at the critical surface, as well as the exhaust velocity, v_∞, and the required laser power W, can be obtained. In this procedure values of ρ_s, T_s, v_s must first be obtained from Figs. 2 or 5 to be used in reading Figs. 3 or 6.

When accelerating shell solutions are to be identified, $\tilde{g}\neq 0$ an additional step is required in the identification procedure. The aspect ratio, A (Fig. 7), must be specified. Note that this is the in flight aspect ratio, which is not in general the same as the initial aspect ratio and is usually larger. By inspection of Fig. 7 and Fig. 5, the values of $\tilde{g}$ and $\tilde{\rho}_p$ are found which correspond to the given values of A and M_p. This will in general require interpolating between values of $\tilde{g}$. From these values of $\tilde{g}$ and $\tilde{\rho}_p$, Fig. 12 gives the value of the burn thru parameter, B, for the particular solution. At this point it can be seen if the specified shell parameters constitute a reasonable choice. As discussed above in Section III C, B should be near 1. Larger values indicate a tendency for ablation to burn thru the shell before the implosion is completed. Smaller values of B indicate small ablative mass removal and, therefore, low energy transfer efficiency.

With the values of v_s and $\tilde{g}$ obtained above the implosion velocity can be estimated. By the same constant acceleration approximation

that gave the implosion time, Δt_I Eq. (34), an approximate final implosion velocity, v_I is

$$v_I \equiv \frac{r_p}{\Delta t_I} = \left(\frac{g r_p}{2}\right)^{1/2} \cong v_s \left(\frac{\tilde{g}}{2}\right)^{1/2} . \qquad (46)$$

The last equality in Eq. (46) is approximate because $\tilde{r}_p \equiv r_p/r_s \cong 1$.

From a mathematical point of view the above procedure of identifying solutions by specifying the shell aspect ratio, A, and the shell M parameter, M_p Eq. (45), may be the most logical. However, the most effective way of determining target and laser parameters from target requirements and physical constraints, i.e., designing a target, is probably to start by specifying aspect ratio, A, and burn through parameter, B. From these parameters and Fig. 13, which is a composite plot of $\tilde{\rho}_p$ and $\tilde{g}$ vs. A and B, $\tilde{\rho}_p$ and $\tilde{g}$ can be obtained quite easily. For example, suppose that a shell aspect ratio of about A=30 is desired to obtain a sufficient compressed $\int \rho dr$, and B=1 is desired to give an efficient implosion. Then from Fig. 13, $\tilde{\rho}_p \simeq 70$ and $\tilde{g} \simeq 1$, which uniquely determines the dimensionless solution. From these parameters and Fig. 2 or 5 the various properties of the ablation region can be obtained. Also, as discussed above in the contexts of $\tilde{g} = 0$ solutions, if ρ_c/ρ_s is given then Figs. 3 and 6 can be used to determine critical surface properties of the solutions, including the required dimensionless laser power $\tilde{W}_\infty$. If, in addition the absolute value of the shell density, ρ_p, and the implosion velocity, v_I, are specified, then the physical values of all other quantities can be obtained. From $\tilde{\rho}_p$ and the absolute value of ρ_c, ρ_s, and, therefore, ρ_c/ρ_s are known. From v_I and Eq. (46), v_s is known, and, therefore, from the definition of $\tilde{W}$ and W_∞, the absolute value of the laser power, W_∞, is known.

With these parameters Eq. (45) for M_p constitutes a relationship between the shell density ρ_p, and the conductivity coefficient G(Z). That is, if the density of the imploding shell is chosen then the atomic number, Z, of the shell material is determined.

It is helpful to notice from Figs. 2 or 5 that for the large values of $\tilde{\rho}_p$ of usual interest, $\tilde{r}_p$, $\tilde{P}_p$ and M are essentially independent of $\tilde{\rho}_p$.

An important consequence of this near constancy of M, which was shown in Ref.(3) for $\tilde{g}=0$, can be seen from Eq.(12). If a particular implosion system, i.e., fixed ρ_p, A and B, is scaled up to larger dimensions, then either G(Z) or T_s must increase. If the implosion velocity is also held fixed in the scaling, then T_s is fixed and G(Z) must increase. That is, larger targets with the same implosion velocity must be made of lower Z materials. On the other hand the implosion velocity can be increased in a target of a given material by increasing the power with increasing dimensions so as to increase the surface temperature.

The discussion above of scaling laws and applications deals explicitly with laser driven ablation in which $\rho_c < \rho_s$. However, the same approach will apply to shells i.e., $g \neq 0$ solutions, driven by particle beams and, with some modification, to shells driven by lasers when $\rho_c = \rho_s$ and a density discontinuity occurs. Subsequent publications will present more details of both $\rho_c = \rho_s$ and particle beam solutions with $g \neq 0$.

VII. Acknowledgement

The authors acknowledge many helpful discussions of this work with Dr. S. J. Gitomer of Los Alamos. A helpful discussion of the charged particle beam problem with Drs. M. Widner and A. Farnsworth of Sandia Laboratories is also acknowledged.

This work was supported by a contract with the Division of Laser Fusion of the U. S. Department of Energy.

References

1. J. Nuckolls, L. Wood, A. Thiessen and G. Zimmerman, Nature 239 (1972); J. Clarke, N. Fisher, R. Mason, Phys. Rev. Lett. 30 (1973) 249.

2. G. Fraley, W. Gula, D. Henderson, R. McCrory, R. Malone, R. Mason, and R. Morse, Plasma Physics and Controlled Nuclear Rusion Research, Vol. II (1974), p. 543, IAEA, Vienna. Published as a 1975 supplement to Nuclear Fusion.

3. S. J. Gitomer, R. L. Morse and B. J. Newberger, Phys. Fluids, 20 (1977) 234, and Los Alamos Report LA-6079, (1975).

4. F. J. Felber, Phys. Rev. Lett. 39, 84 (1977).

5. C. E. Max and C. F. McKee, Phys. Rev. Lett. 39, 1336 (1977).

6. L. Spitzer, Physics of Fully Ionized Gases (Interscience, New York, 1965) Chapt. 5, p. 143. We have used Λ = const.

7. R. L. McCrory and R. L. Morse, Phys. Rev. Lett. 38, 544 (1977).

8. J. S. Pearlman, Rev. Sci. Instrum. 48, 1064 (Aug. 1977).

9. R. E. Kidder, Nuclear Fusion 14, 53 (1974).

10. K. Brueckner, Rev. Mod. Phys., April 1974.

11. J. Virmont, Private communications.

12. K. Matzen, private communication.

Fig. 1a. Steady flow profiles of the pellet and ablation region for the laser case with $\tilde{\rho}_p = 10^2$ and $\tilde{g} = 0$ for several values of $\tilde{\rho}_c$.

Fig. 1b Logarithmic profiles for the case $\tilde{\rho}_p = 10^2$, $\tilde{g} = 0$ and a range of values of $\tilde{\rho}_c$.

Fig. 1c Logarithmic profiles for the comparison case of $\tilde{\rho}_p = 10$ and $\tilde{g} = 0$.

Fig. 2 Flow variables at the pellet surface and values of $\tilde{v}_b^2$ and M as a function of $\tilde{\rho}_p$ for $\tilde{g} = 0$.

Fig. 3 The dimensionless laser power and the scaled flow variables evaluated at the critical surface as a function of $\tilde{\rho}_c$ for $\tilde{g} = 0$. The exhaust fluid velocity, $\tilde{v}_\infty$, is also given.

Fig. 4a A linear plot of the pellet and ablation front profiles for $\tilde{\rho}_p = 10^2$ and $\tilde{g} = 1$ with the pellet mass, $\tilde{m}_p$, and mass, $\tilde{m}_s$, within the sonic point, $\tilde{r} = 1$, shown.

Fig. 4b Logarithmic profiles of the laser case with $\tilde{\rho}_p = 10^2$ and $\tilde{g} = 1$. for several values of $\tilde{\rho}_c$.

Fig. 5a Values of the flow variables at the pellet surface, the mass of the pellet, the mass within the sonic point $\tilde{r} = 1$ and the values of $\tilde{v}_b^2$, M and M_p as a function of $\tilde{\rho}_p$ for $\tilde{g} = 1$.

Fig. 5b Various scaled quantities evaluated at the pellet surface and sonic point as a function of $\tilde{\rho}_p$ for $\tilde{g} = 10^{-\frac{1}{2}}$.

Fig. 5c The same quantities as shown in Fig. 5b plotted for the case $\tilde{g} = 10^{+\frac{1}{2}}$.

Fig. 6 The dimensionless laser power, $\tilde{W}_\infty$, and the scaled flow variables evaluated at the critical surface as a function of $\tilde{\rho}$ for $\tilde{g} = 1$.

Fig. 7 The aspect ratio, A, as a function of $\tilde{\rho}_p$ for a range of values of $\tilde{g}$.

Fig. 8 Steady flow profiles for the case $\tilde{g} \to \infty$ and $\tilde{\rho}_p = 10^2$ with a comparison case of $\tilde{g}=1$ and $\tilde{\rho}_p = 10^2$ plotted against x_g scaled units.

Fig. 9 Values of the flow variables and other quantities evaluated at the pellet surface and sonic point $\tilde{x} = 0$ for the planar case.

Fig. 10 The flow variables at the critical surface and the dimensionless power, $\tilde{W}_\infty$, as a function of $\tilde{\rho}_c$ for the planar case.

Fig. 11 The ratio of the pressure at the pellet surface to that at the inner sonic point as a function of $\tilde{\rho}_p$ for a range of values of $\tilde{g}$. This is used to determine the region of parameter space in which the model is valid.

Fig. 12 The burn-thru ratio, B, as a function of $\tilde{\rho}_p$ for various values of $\tilde{g}$.

Fig. 13 A composite plot of the burn thru parameter and aspect ratio for a range of values of $\tilde{\rho}_p$ and $\tilde{g}$.

Fig. 14a Discontinuous profiles with an isothermal mach number of 2 at $\tilde{r}_c=1$ for $\tilde{\rho}_p=10^2$ for (solid-line) and $\tilde{\rho}_p=10$ with (dashed line) and $\tilde{g}=0$.

Fig. 14b A dimensionless variable linear in T_c and other quantities which characterize the critical surface as a function of a dimensionless variable proportional to $(G(Z)W^{4/3})$. Values to the left of the vertical dashed line are from discontinuous solutions, while those to the right are from cases in which $\tilde{r}_c>\tilde{r}_s$.

Fig. 15a Logarithmic profiles of the charged particle beam deposition case for $\tilde{\rho}_p=10^2$, $\tilde{g}=0$, and $\tilde{r}_R>\tilde{r}_s$.

Fig. 15b Profiles of the charged particle beam deposit ion with $\tilde{\rho}_p=10^2$ and $\tilde{g}=0$ in which the beam penetrates within the sonic point but thermal conduction is important.

Fig. 15c A case which is similar to that shown in Fig. 15b except that $\tilde{r}_R>\tilde{r}_s$ and thermal conduction plays a very small role.

Fig. 16 The dimensionless particle beam power, $\tilde{W}_\infty$, necessary to drive the ablation, the exhaust flow velocity, $\tilde{v}_\infty$, and other computed quantities, as a function of the range, $\tilde{\sigma}_\infty$.

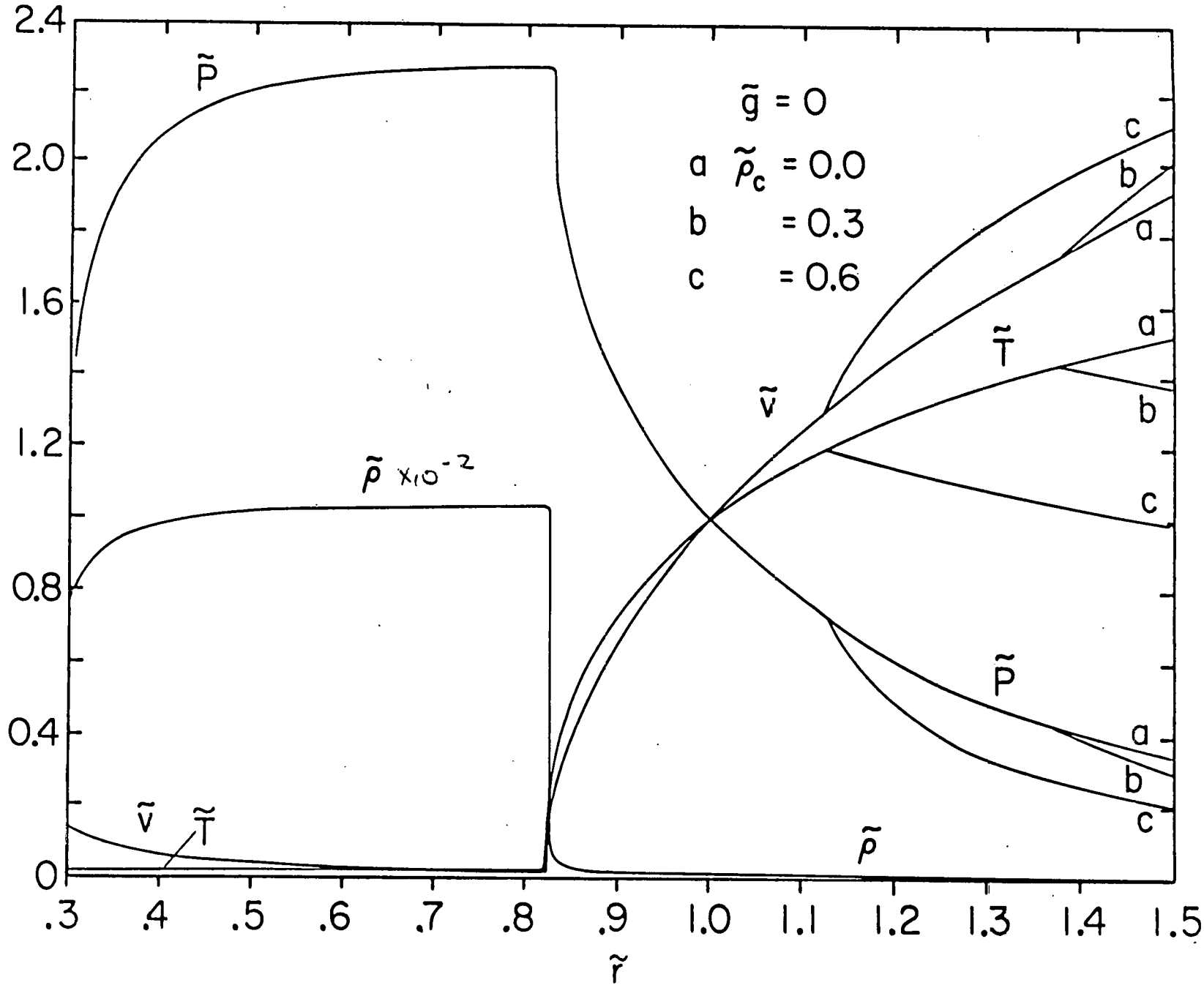
2.4
2.0
1.6
1.2
0.8
0.4
0
.3
.4
.5
.6
.7
.8
.9
1.0
1.1
1.2
1.3
1.4
1.5
r̃
P̃
ρ̃ x10⁻²
ṽ
T̃
ρ̃
g̃ = 0
a ρ̃c = 0.0
b = 0.3
c = 0.6
a
b
c

Fig 1a

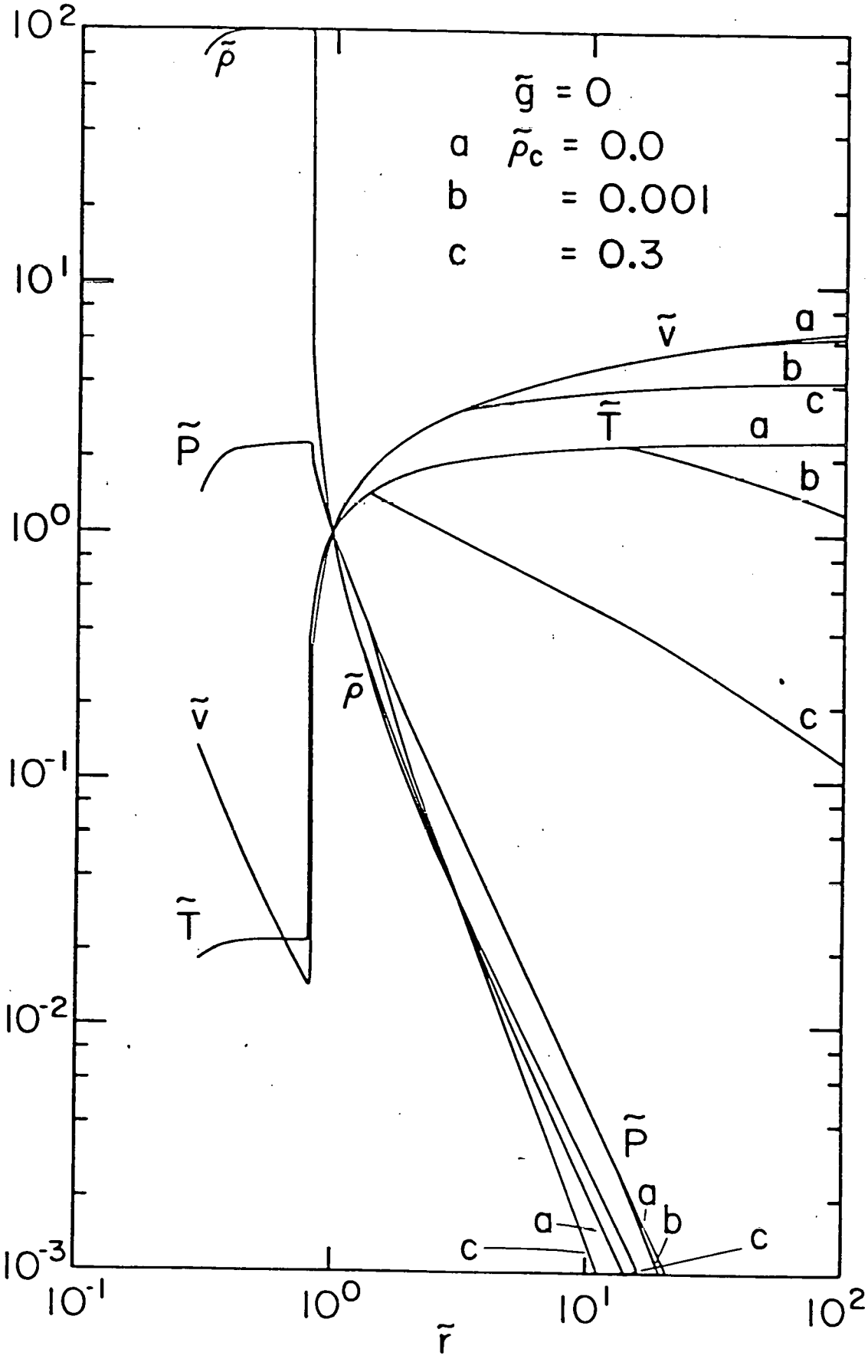
$\tilde{g} = 0$
a $\tilde{\rho}_c = 0.0$
b = 0.001
c = 0.3
$\tilde{\rho}$
$\tilde{v}$
$\tilde{T}$
$\tilde{P}$
a
b
c
10^2
10^1
10^0
10^{-1}
10^{-2}
10^{-3}
10^{-1}
10^0
10^1
10^2
$\tilde{r}$

Fig. 1b

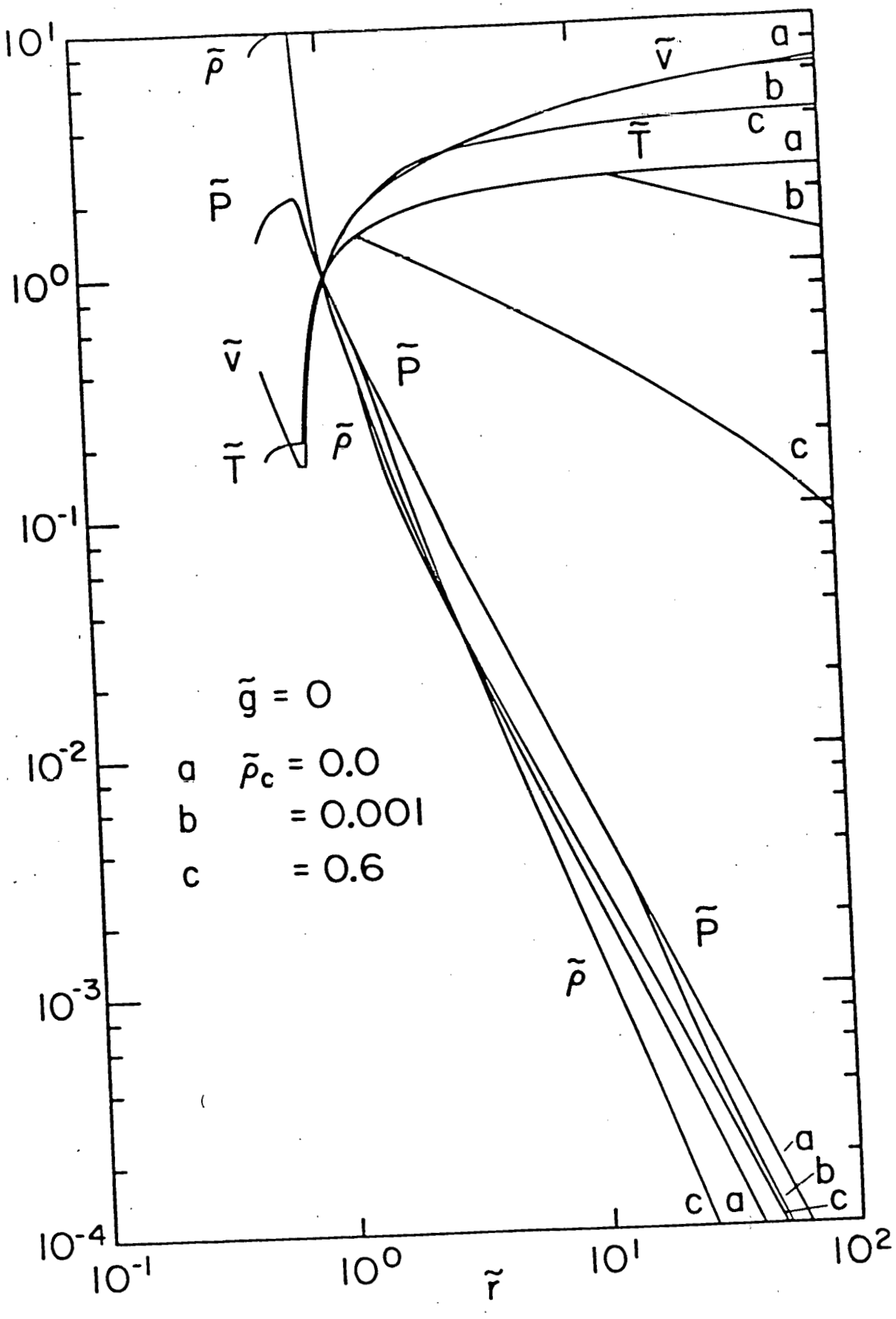
$\tilde{\rho}$
$\tilde{P}$
$\tilde{v}$
$\tilde{T}$
a
b
c
$\tilde{g} = 0$
a $\tilde{\rho}_c = 0.0$
b = 0.001
c = 0.6
10^1
10^0
10^{-1}
10^{-2}
10^{-3}
10^{-4}
10^{-1}
10^0
10^1
10^2
$\tilde{r}$

Fig. 1c

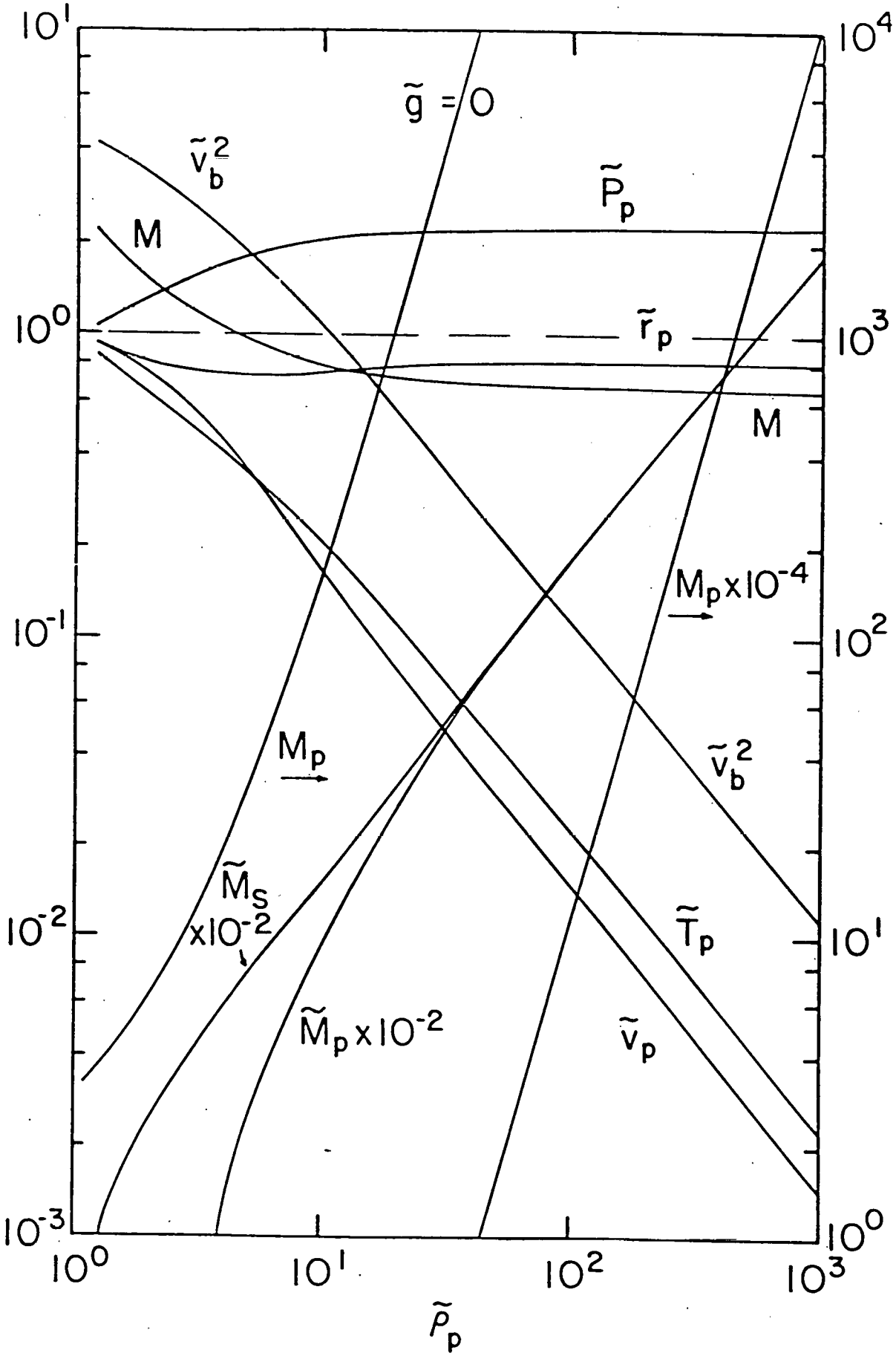
10^1
10^0
10^{-1}
10^{-2}
10^{-3}
10^4
10^3
10^2
10^1
10^0
10^0
10^1
10^2
10^3
$\tilde{g} = 0$
$\tilde{v}_b^2$
$\tilde{P}_p$
M
$\tilde{r}_p$
M
$M_p \times 10^{-4}$
M_p
$\tilde{v}_b^2$
$\tilde{M}_s \times 10^{-2}$
$\tilde{T}_p$
$\tilde{M}_p \times 10^{-2}$
$\tilde{v}_p$
$\tilde{\rho}_p$

Fig. 3

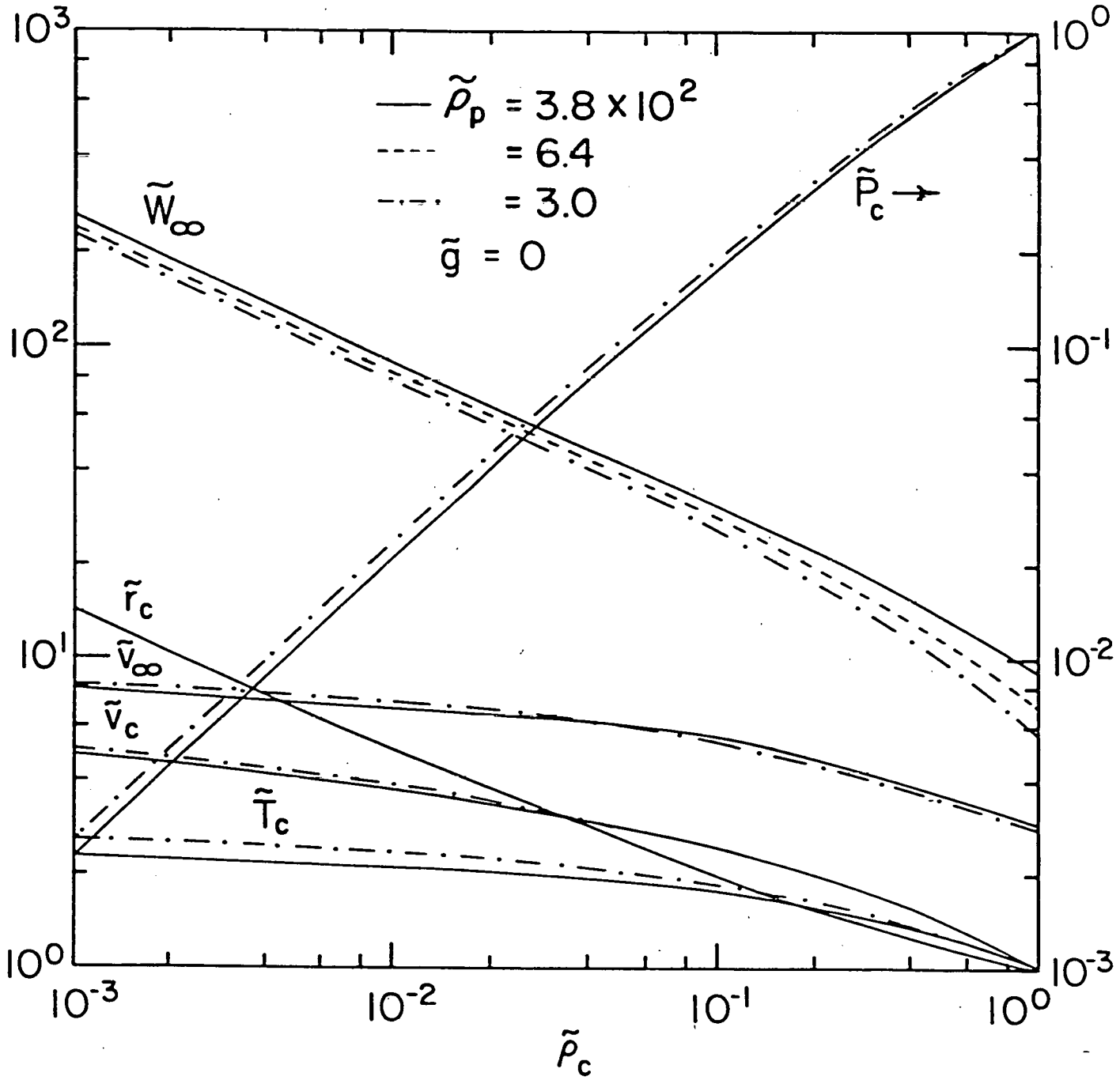
10^3
10^2
10^1
10^0
10^0
10^{-1}
10^{-2}
10^{-3}
10^{-3}
10^{-2}
10^{-1}
10^0
$\tilde{\rho}_c$
$\tilde{\rho}_p = 3.8 \times 10^2$
$= 6.4$
$= 3.0$
$\tilde{g} = 0$
$\tilde{W}_\infty$
$\tilde{P}_c \rightarrow$
$\tilde{r}_c$
$\tilde{v}_\infty$
$\tilde{v}_c$
$\tilde{T}_c$

Fig. 3

Fig. 4a

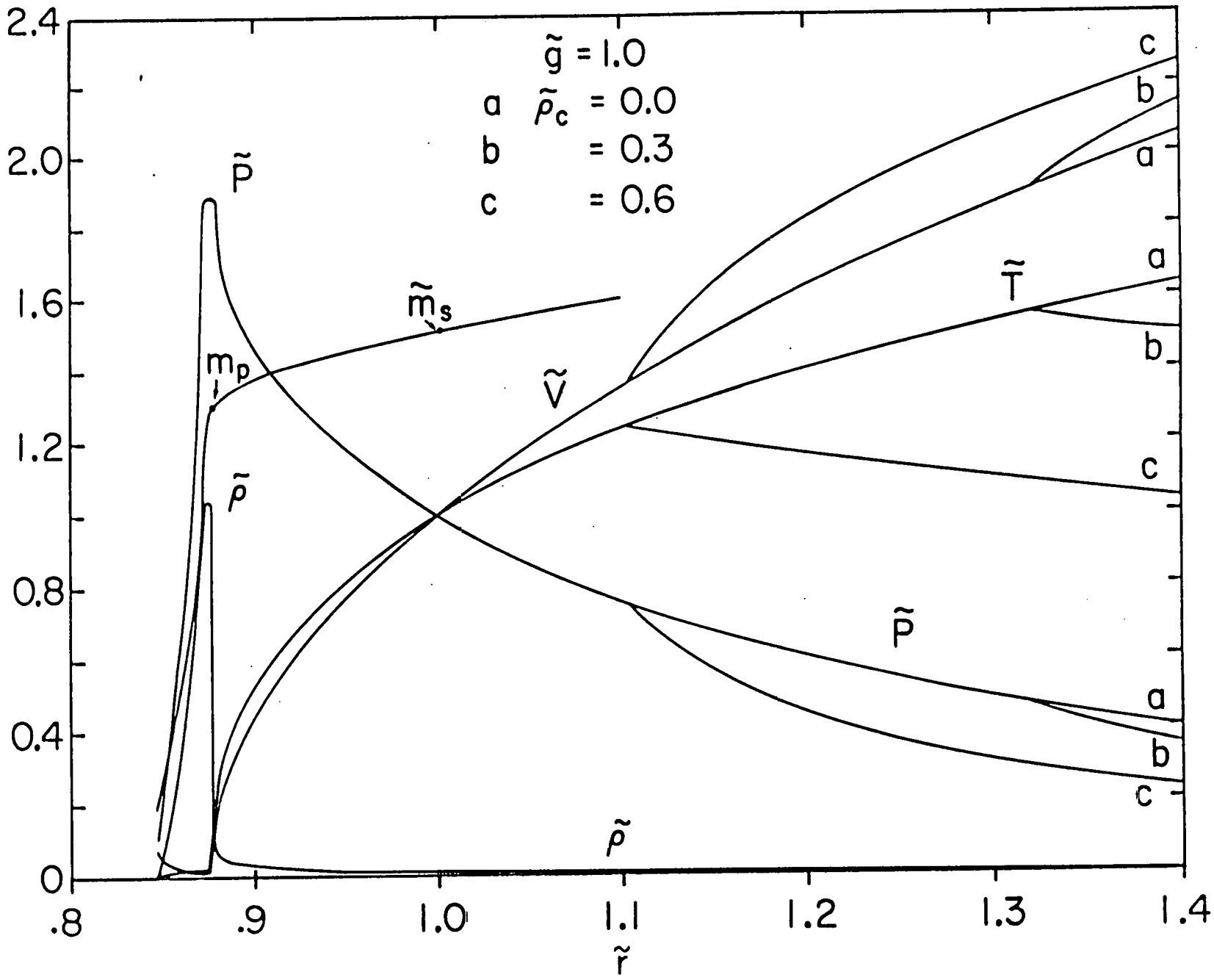
$\tilde{g}$ = 1.0
a $\tilde{\rho}_c$ = 0.0
b = 0.3
c = 0.6
$\tilde{P}$
$\tilde{m}_s$
m_p
$\tilde{V}$
$\tilde{T}$
$\tilde{\rho}$
$\tilde{P}$
$\tilde{\rho}$
a
b
c
2.4
2.0
1.6
1.2
0.8
0.4
0
.8
.9
1.0
1.1
1.2
1.3
1.4
$\tilde{r}$

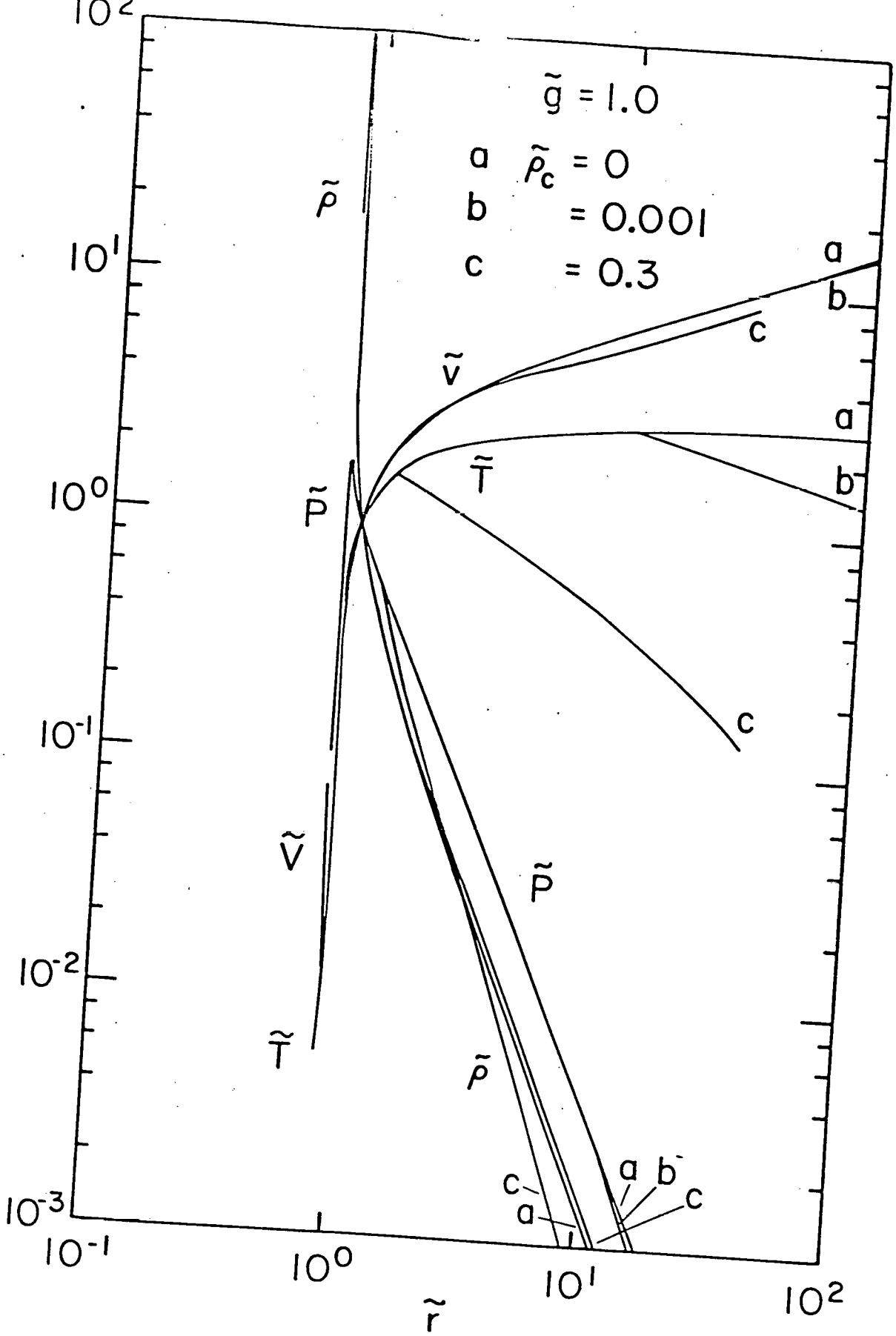
$\tilde{g} = 1.0$
a $\tilde{\rho}_c = 0$
b = 0.001
c = 0.3
$\tilde{\rho}$
$\tilde{v}$
$\tilde{T}$
$\tilde{P}$
$\tilde{V}$
$\tilde{P}$
$\tilde{T}$
$\tilde{\rho}$
10^2
10^1
10^0
10^{-1}
10^{-2}
10^{-3}
10^{-1}
10^0
10^1
10^2
$\tilde{r}$

Fig. 4b

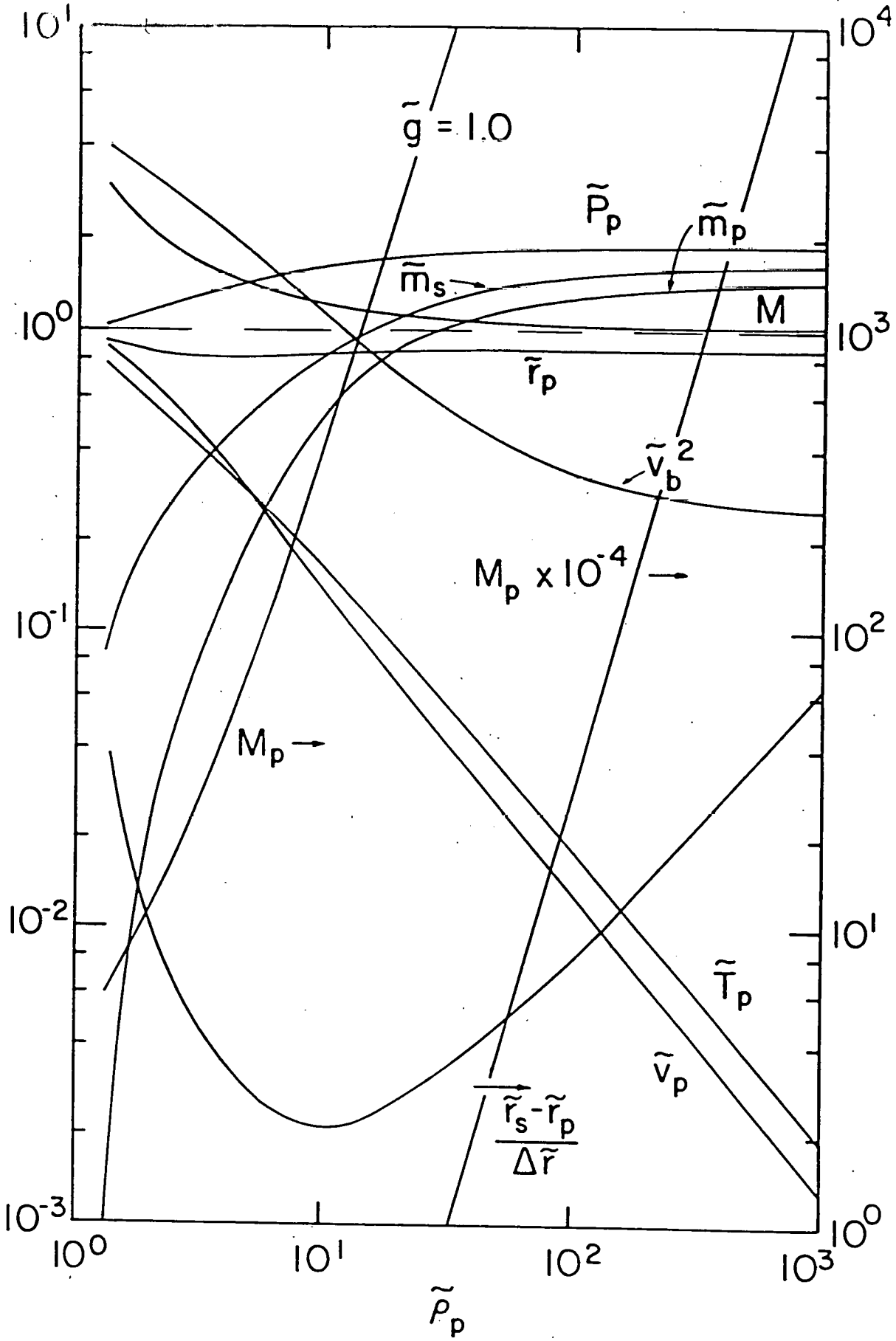
10^1
10^0
10^{-1}
10^{-2}
10^{-3}
10^4
10^3
10^2
10^1
10^0
10^0
10^1
10^2
10^3
$\tilde{g} = 1.0$
$\tilde{P}_p$
$\tilde{m}_p$
$\tilde{m}_s$
M
$\tilde{r}_p$
$\tilde{v}_b^2$
$M_p \times 10^{-4}$
M_p
$\tilde{T}_p$
$\tilde{v}_p$
$\frac{\tilde{r}_s - \tilde{r}_p}{\Delta \tilde{r}}$
$\tilde{\rho}_p$

Fig. 5a

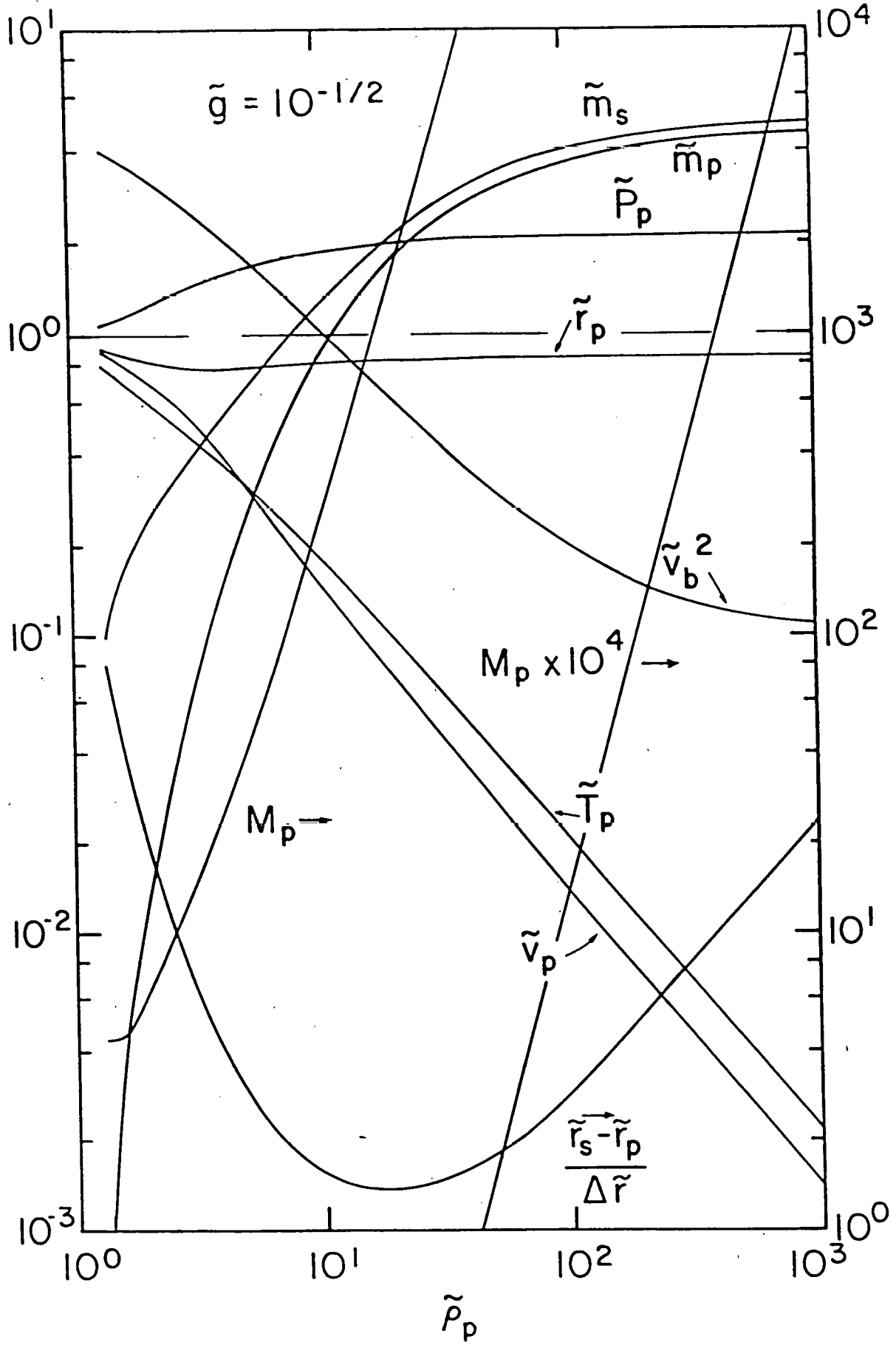
$\tilde{g} = 10^{-1/2}$
$\tilde{m}_s$
$\tilde{m}_p$
$\tilde{P}_p$
$\tilde{r}_p$
$\tilde{v}_b^2$
$M_p \times 10^4 \rightarrow$
$\leftarrow \tilde{T}_p$
$M_p \rightarrow$
$\tilde{v}_p$
$\frac{\tilde{r}_s - \tilde{r}_p}{\Delta \tilde{r}}$
10^1
10^0
10^{-1}
10^{-2}
10^{-3}
10^4
10^3
10^2
10^1
10^0
10^0
10^1
10^2
10^3
$\tilde{\rho}_p$

Fig. 5b

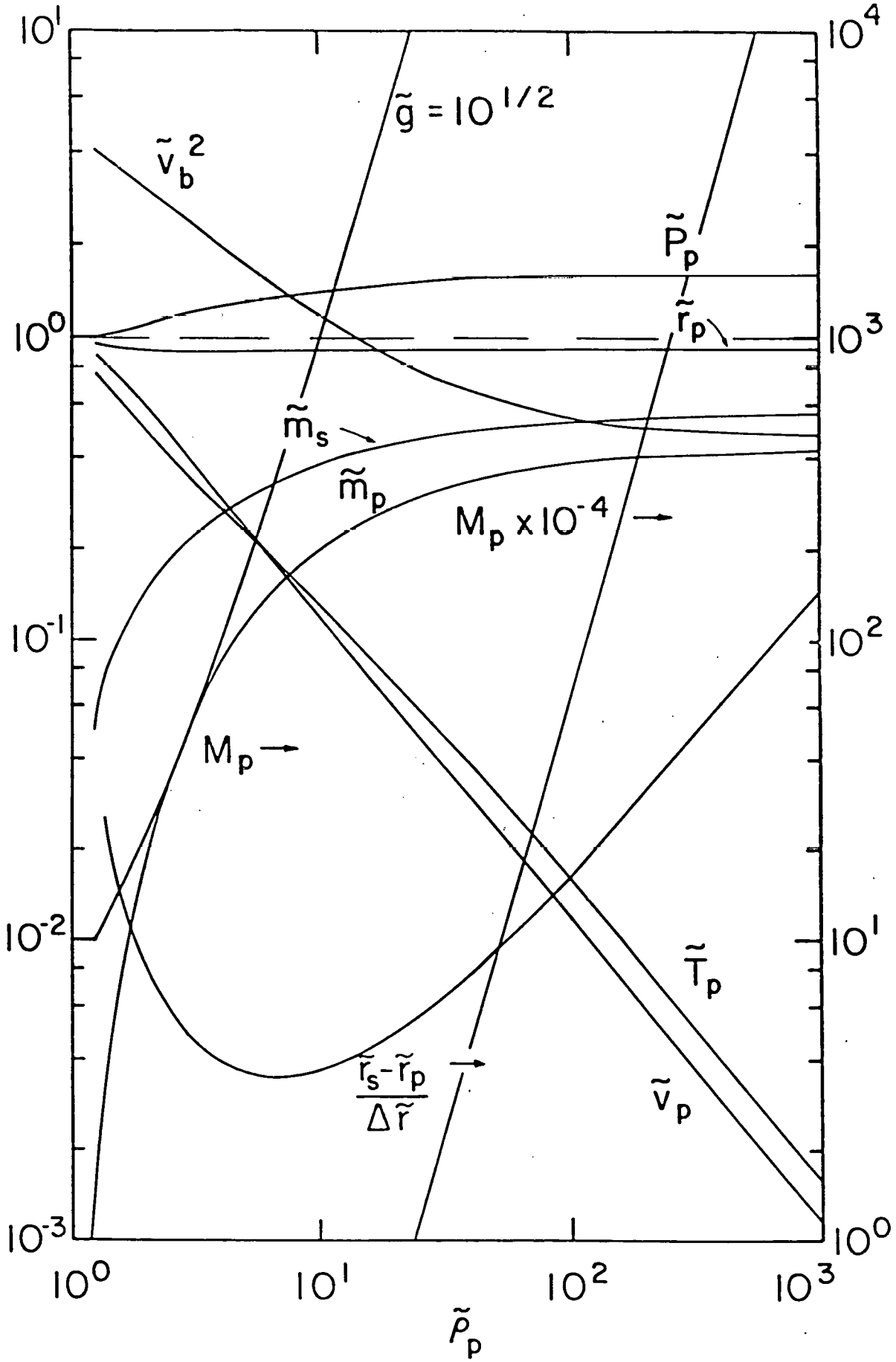
10^1
10^0
10^{-1}
10^{-2}
10^{-3}
10^4
10^3
10^2
10^1
10^0
10^0
10^1
10^2
10^3
$\tilde{\rho}_p$
$\tilde{g} = 10^{1/2}$
$\tilde{v}_b^2$
$\tilde{P}_p$
$\tilde{r}_p$
$\tilde{m}_s$
$\tilde{m}_p$
$M_p \times 10^{-4}$
M_p
$\tilde{T}_p$
$\frac{\tilde{r}_s - \tilde{r}_p}{\Delta \tilde{r}}$
$\tilde{v}_p$

Fig. 5c

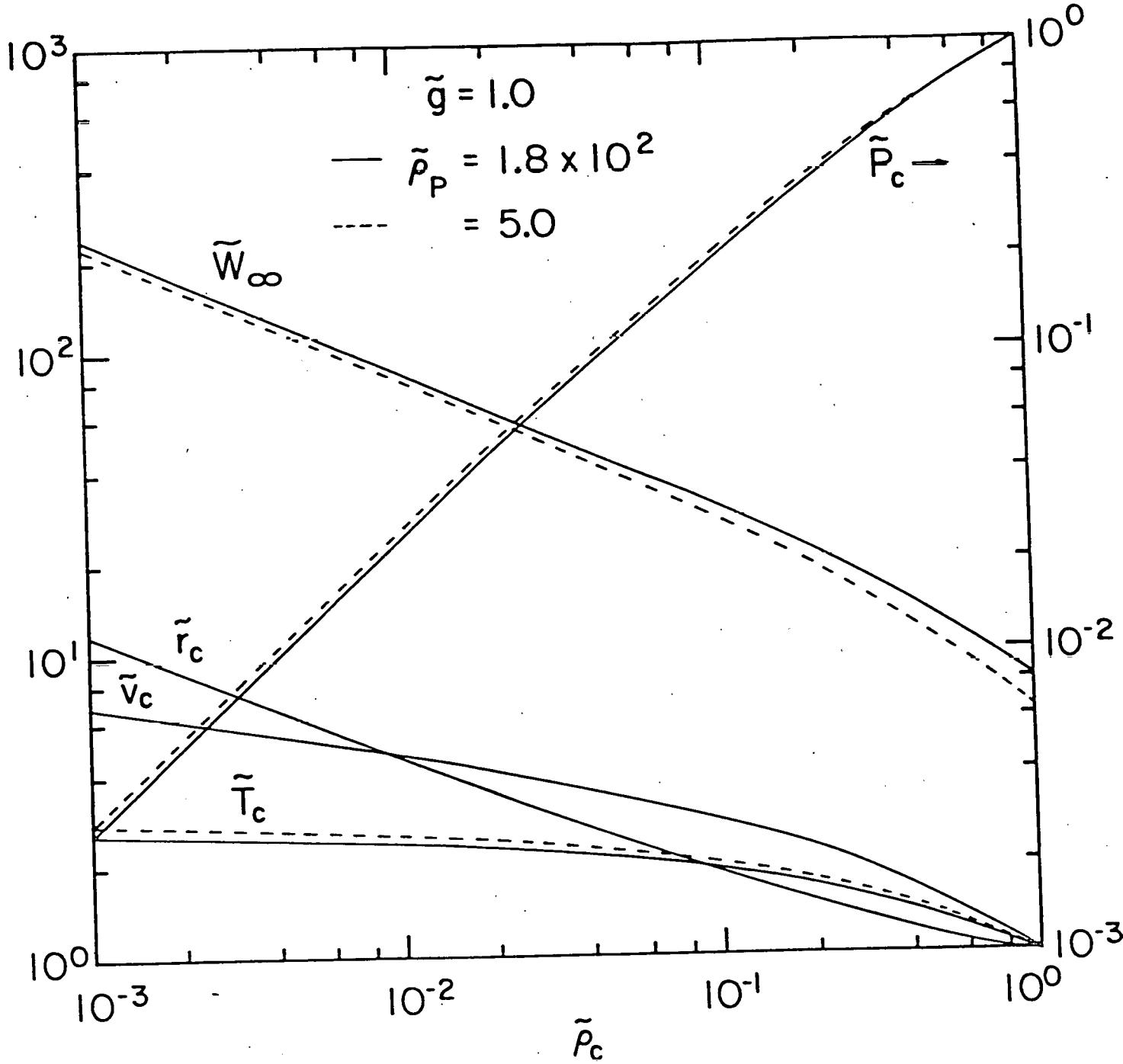
$\tilde{g} = 1.0$
$\tilde{\rho}_P = 1.8 \times 10^2$
$= 5.0$
$\tilde{W}_\infty$
$\tilde{P}_c$
$\tilde{r}_c$
$\tilde{v}_c$
$\tilde{T}_c$
10^3
10^2
10^1
10^0
10^0
10^{-1}
10^{-2}
10^{-3}
10^{-3}
10^{-2}
10^{-1}
10^0
$\tilde{\rho}_c$

Fig. 4

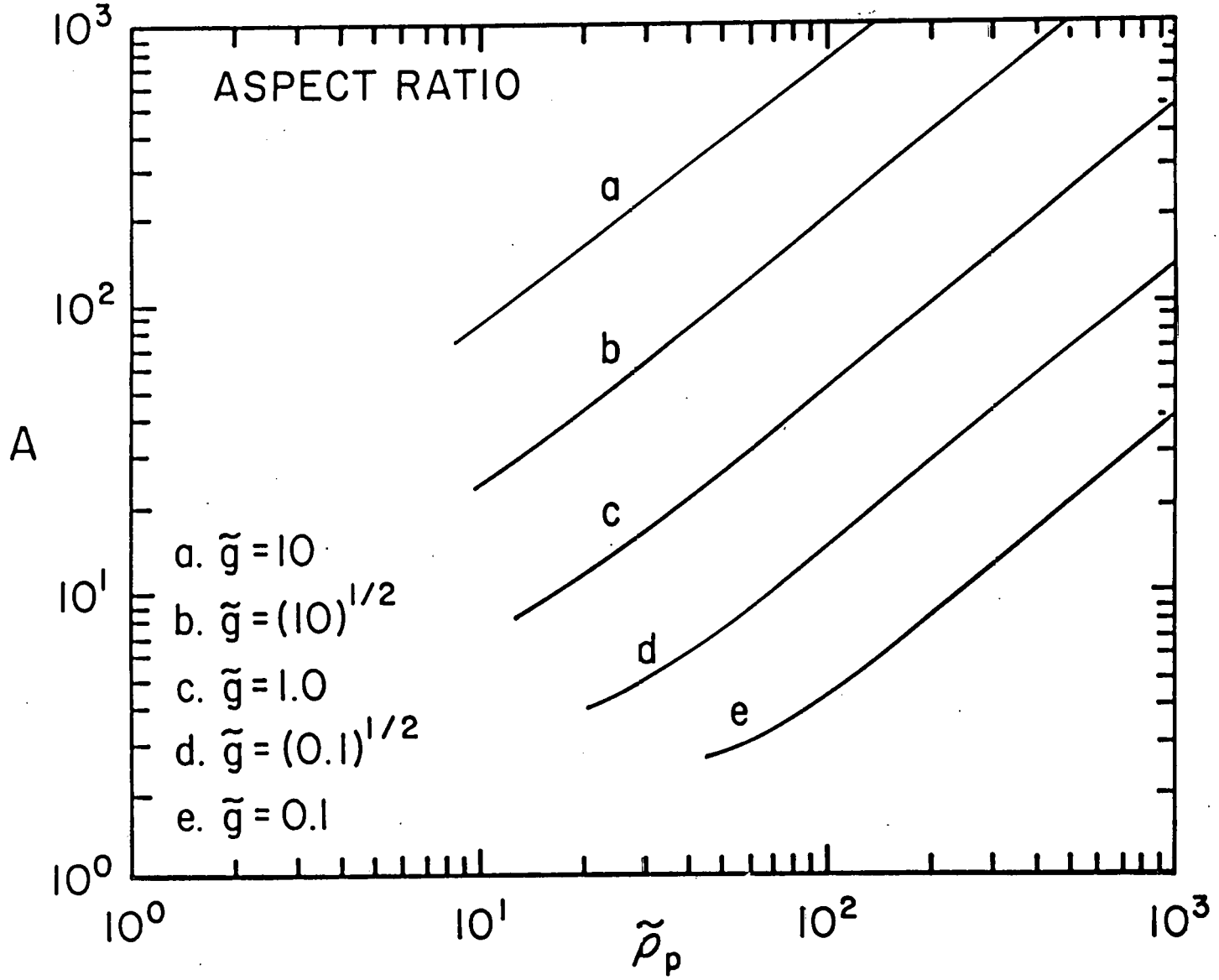
ASPECT RATIO
A
10^3
10^2
10^1
10^0
10^0
10^1
10^2
10^3
$\tilde{\rho}_p$
a
b
c
d
e
a. $\tilde{g} = 10$
b. $\tilde{g} = (10)^{1/2}$
c. $\tilde{g} = 1.0$
d. $\tilde{g} = (0.1)^{1/2}$
e. $\tilde{g} = 0.1$

Fig. 4

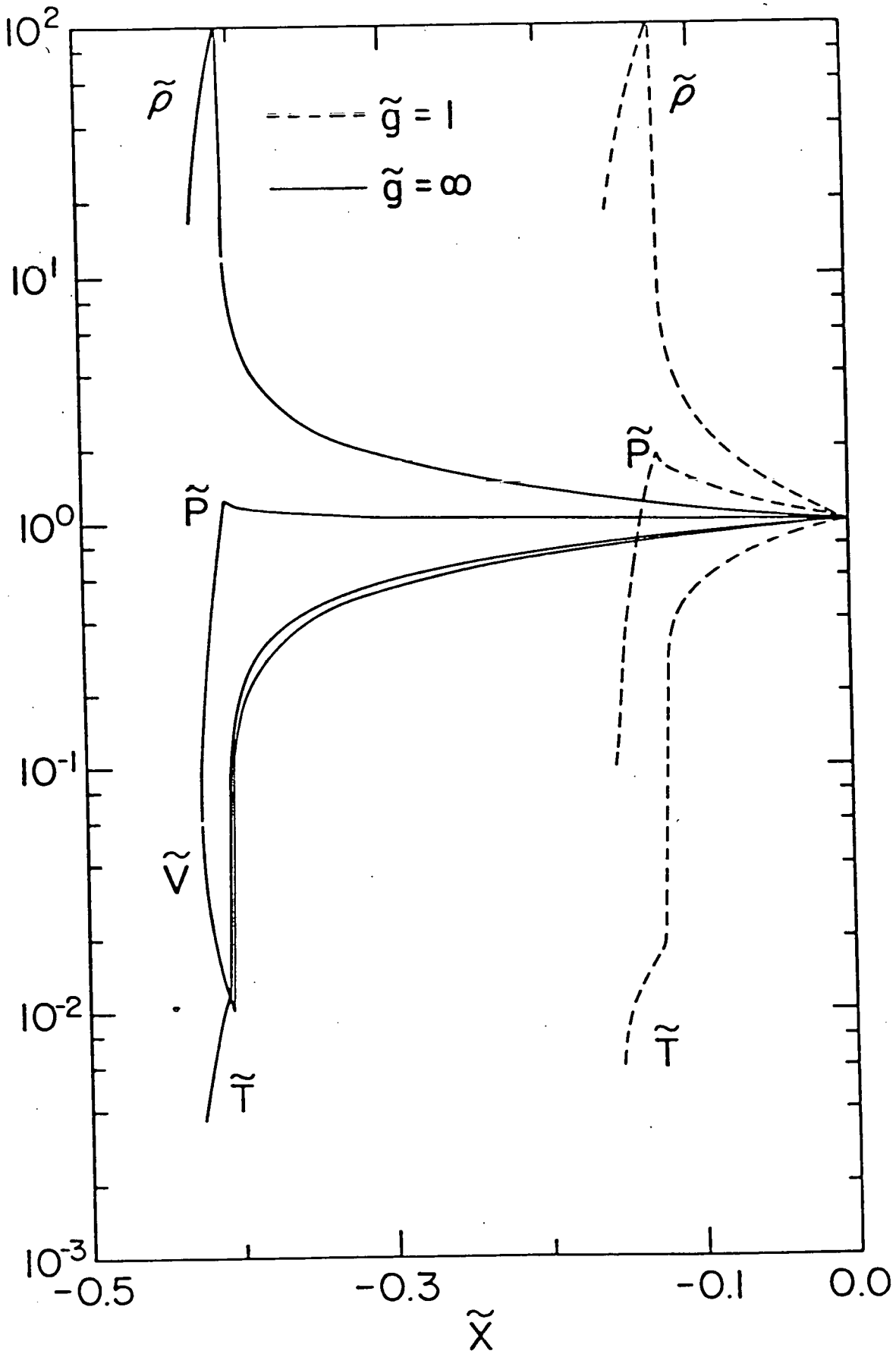
10^2
10^1
10^0
10^{-1}
10^{-2}
10^{-3}
$\tilde{\rho}$
$\tilde{g} = 1$
$\tilde{g} = \infty$
$\tilde{\rho}$
$\tilde{P}$
$\tilde{P}$
$\tilde{V}$
$\tilde{T}$
$\tilde{T}$
-0.5
-0.3
-0.1
0.0
$\tilde{X}$

Fig. 8

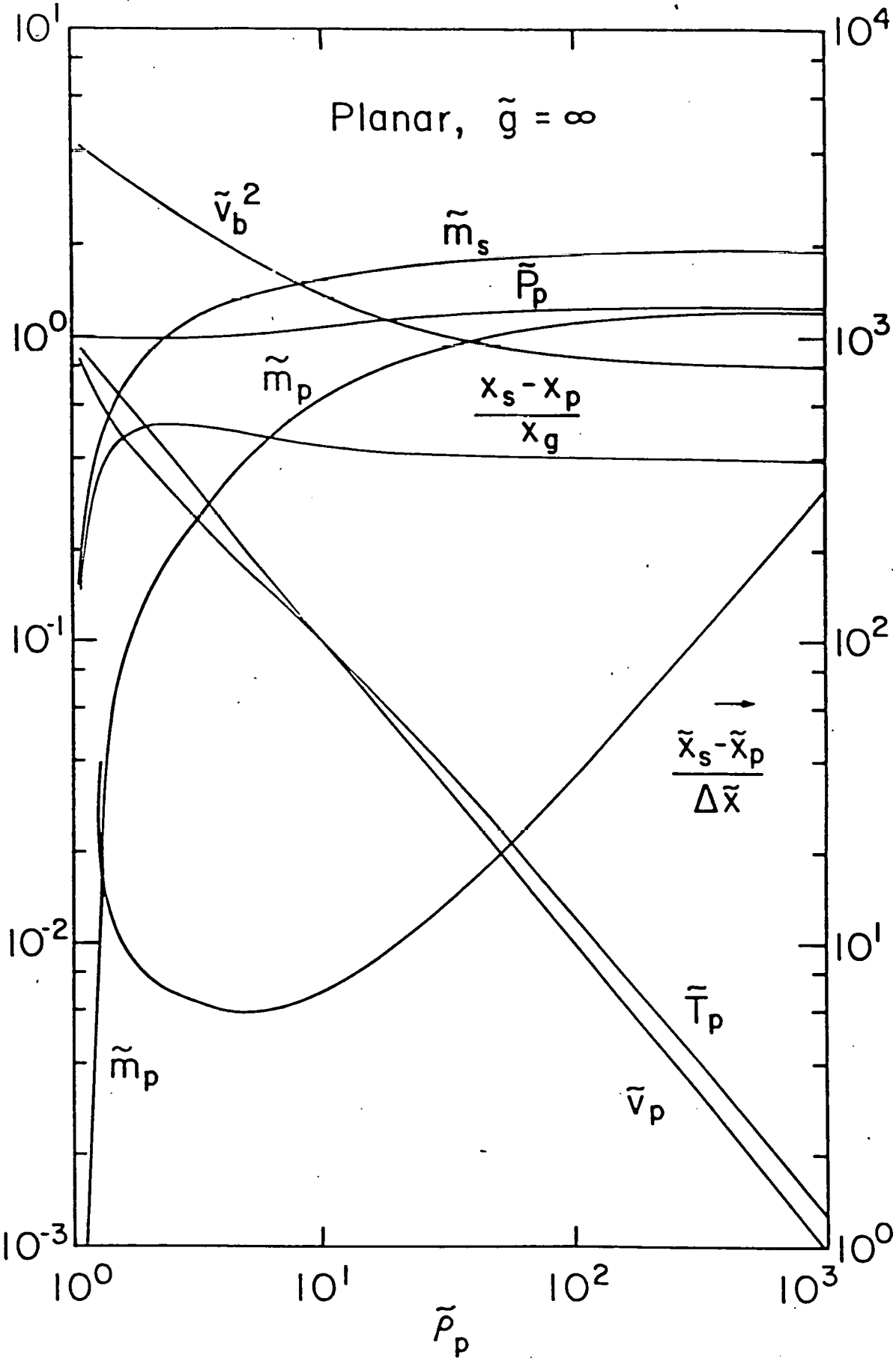
Planar, $\tilde{g} = \infty$
$\tilde{v}_b^2$
$\tilde{m}_s$
$\tilde{P}_p$
$\tilde{m}_p$
$\frac{x_s - x_p}{x_g}$
$\frac{\tilde{x}_s - \tilde{x}_p}{\Delta \tilde{x}}$
$\tilde{T}_p$
$\tilde{m}_p$
$\tilde{v}_p$
10^1
10^0
10^{-1}
10^{-2}
10^{-3}
10^4
10^3
10^2
10^1
10^0
10^0
10^1
10^2
10^3
$\tilde{\rho}_p$

Fig. 9

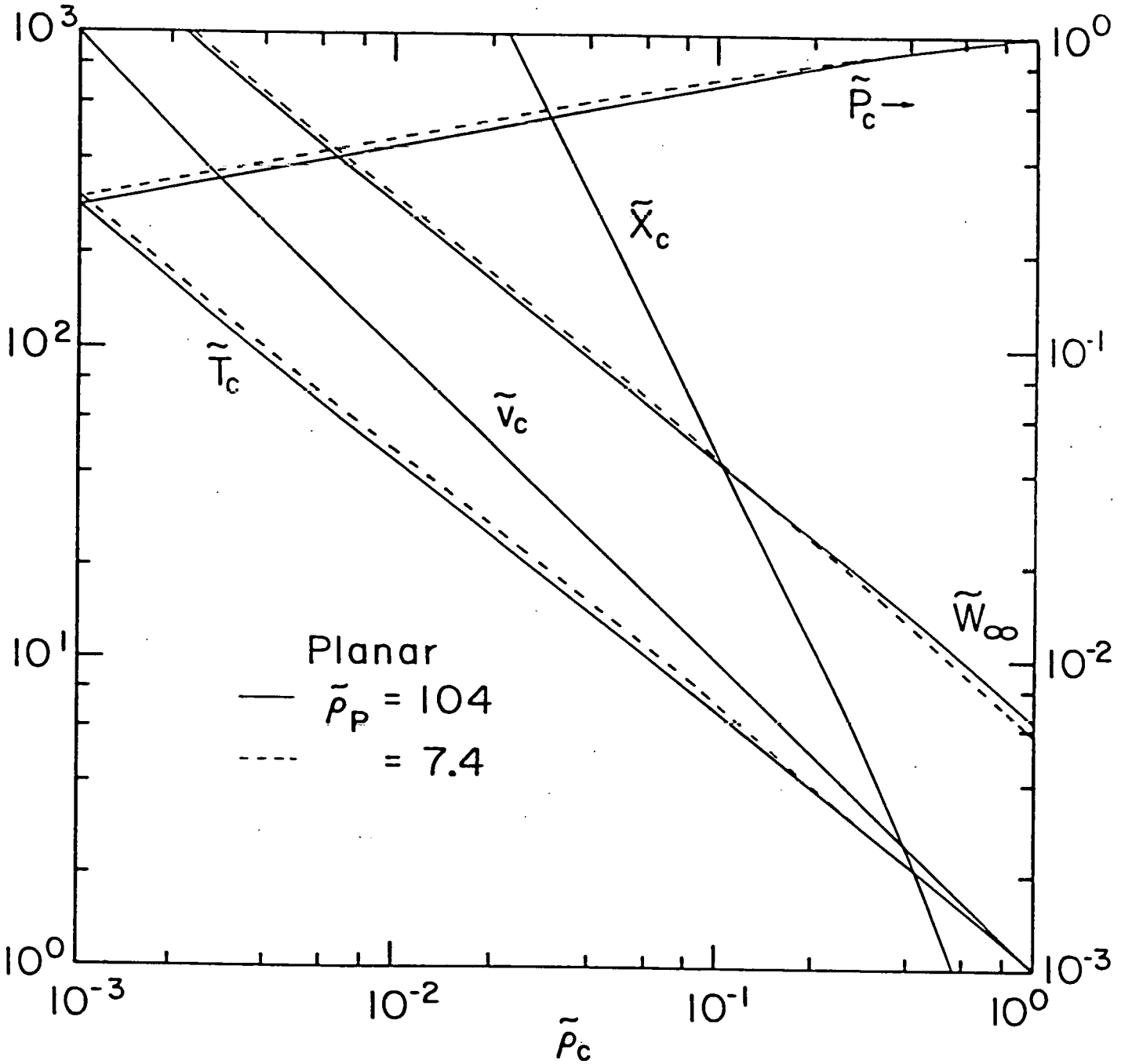
10^3
10^2
10^1
10^0
10^0
10^{-1}
10^{-2}
10^{-3}
10^{-3}
10^{-2}
10^{-1}
10^0
$\tilde{\rho}_c$
$\tilde{P}_c \rightarrow$
$\tilde{X}_c$
$\tilde{T}_c$
$\tilde{v}_c$
$\tilde{W}_\infty$
Planar
$\tilde{\rho}_P = 104$
$= 7.4$

Fig. 10

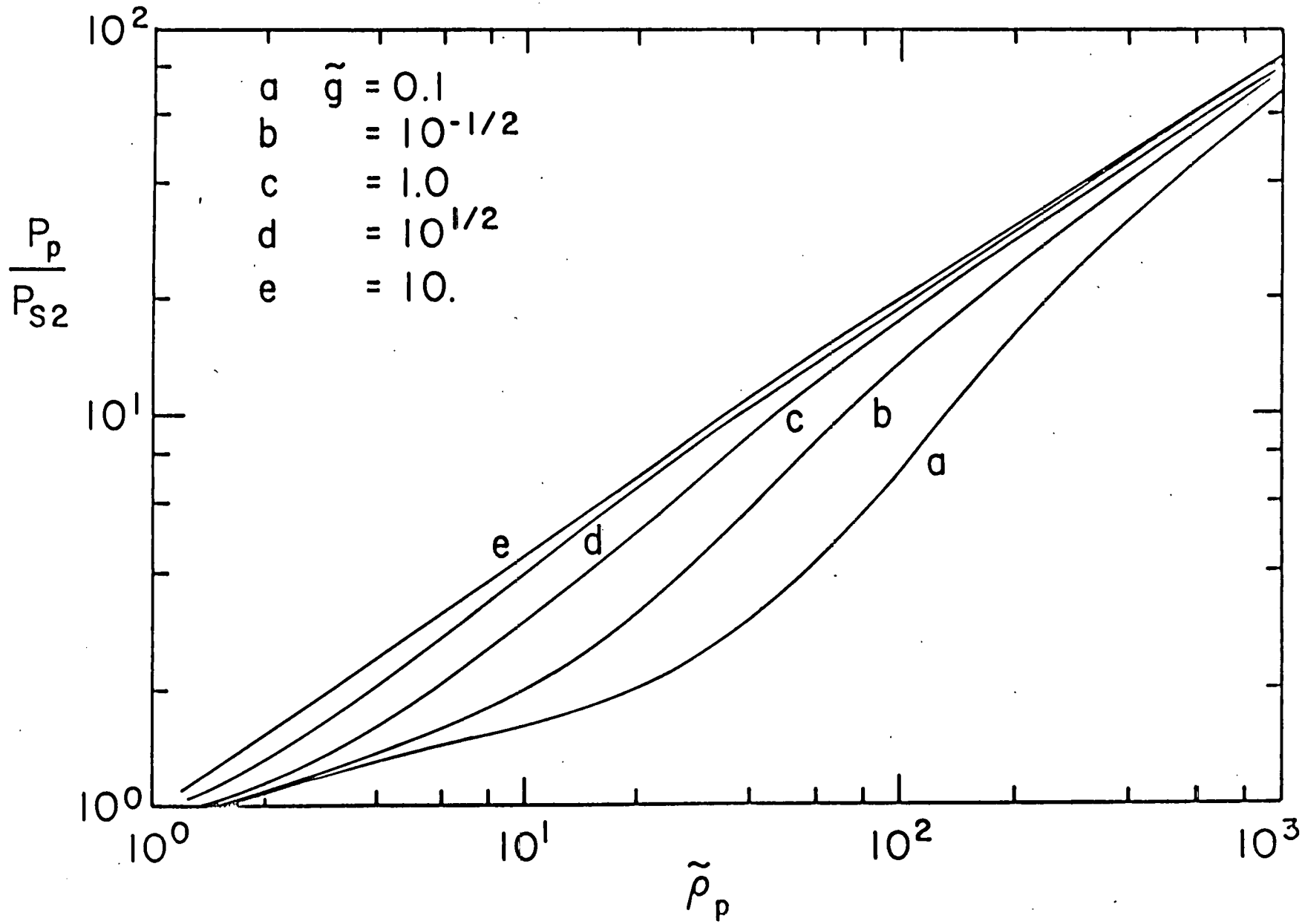
10^2
10^1
10^0
10^0
10^1
10^2
10^3
$\frac{P_p}{P_{S2}}$
$\tilde{\rho}_p$
a $\tilde{g}$ = 0.1
b = $10^{-1/2}$
c = 1.0
d = $10^{1/2}$
e = 10.
a
b
c
d
e

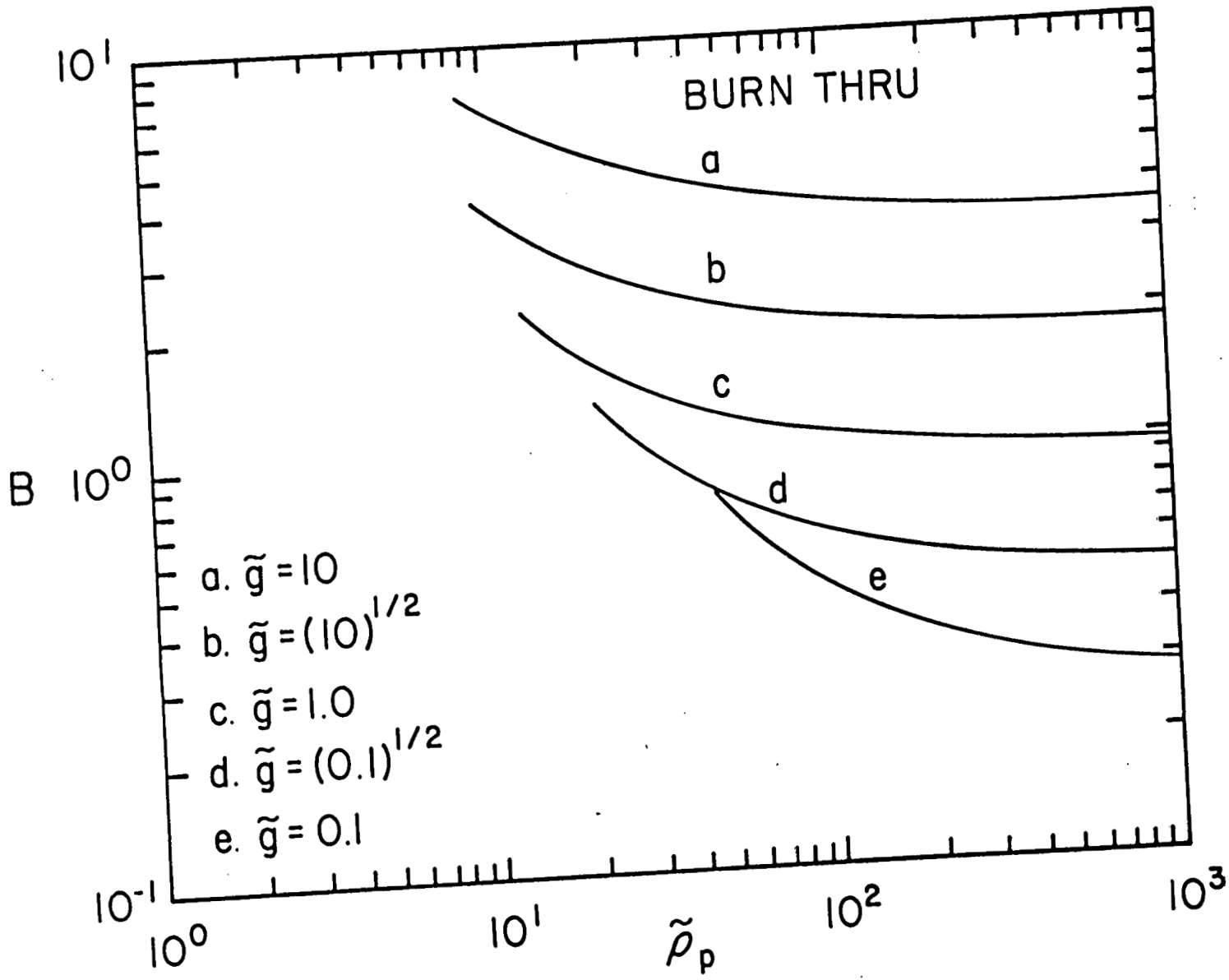
BURN THRU
a
b
c
d
e
B
10^1
10^0
10^{-1}
10^0
10^1
10^2
10^3
$\tilde{\rho}_p$
a. $\tilde{g} = 10$
b. $\tilde{g} = (10)^{1/2}$
c. $\tilde{g} = 1.0$
d. $\tilde{g} = (0.1)^{1/2}$
e. $\tilde{g} = 0.1$

Fig 5a

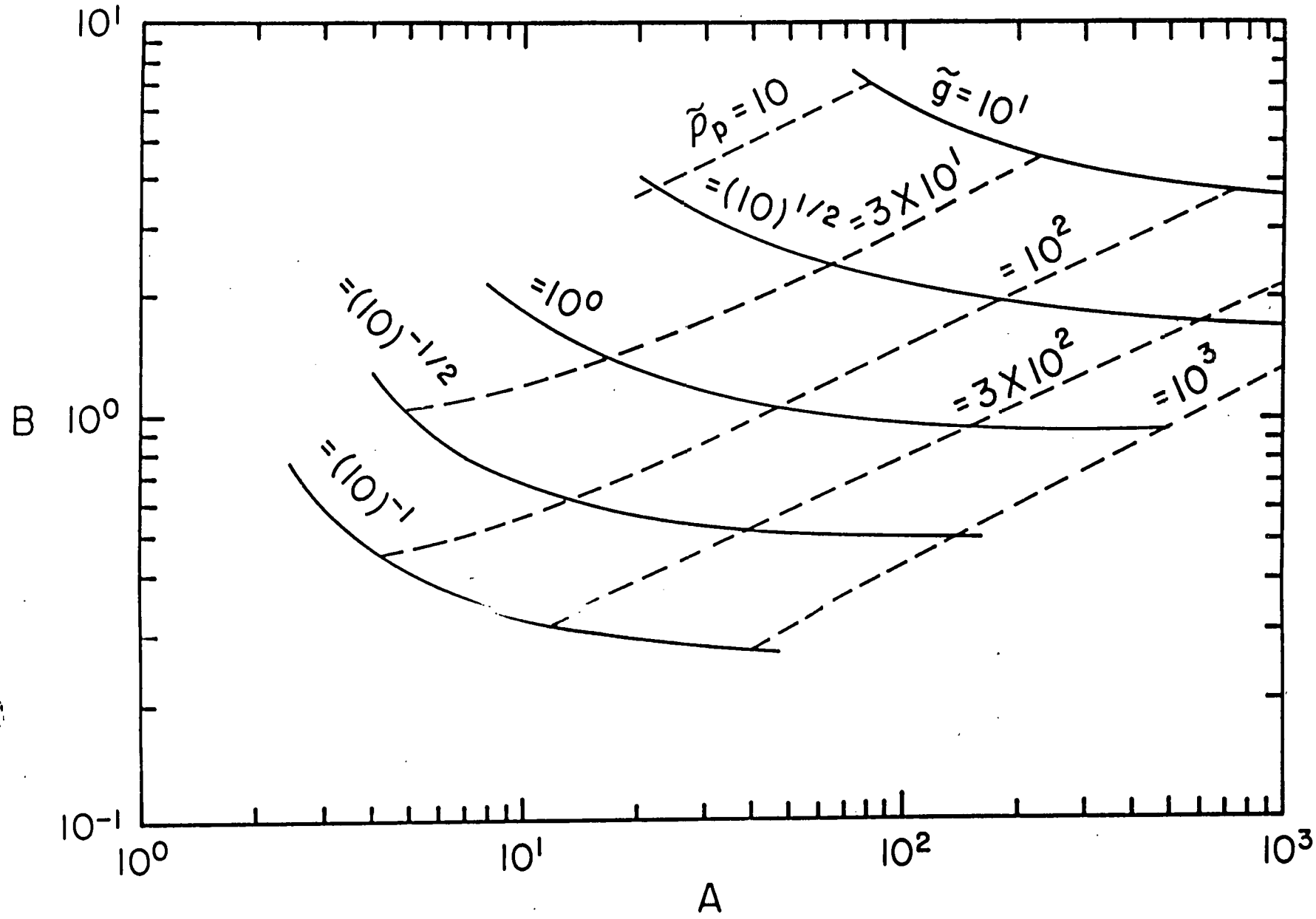
10^1
10^0
10^{-1}
B
10^0
10^1
10^2
10^3
A
$\tilde{p}_p = 10$
$\tilde{g} = 10^1$
$= (10)^{1/2} = 3 \times 10^1$
$= 10^2$
$= 10^0$
$= (10)^{-1/2}$
$= 3 \times 10^2$
$= 10^3$
$= (10)^{-1}$

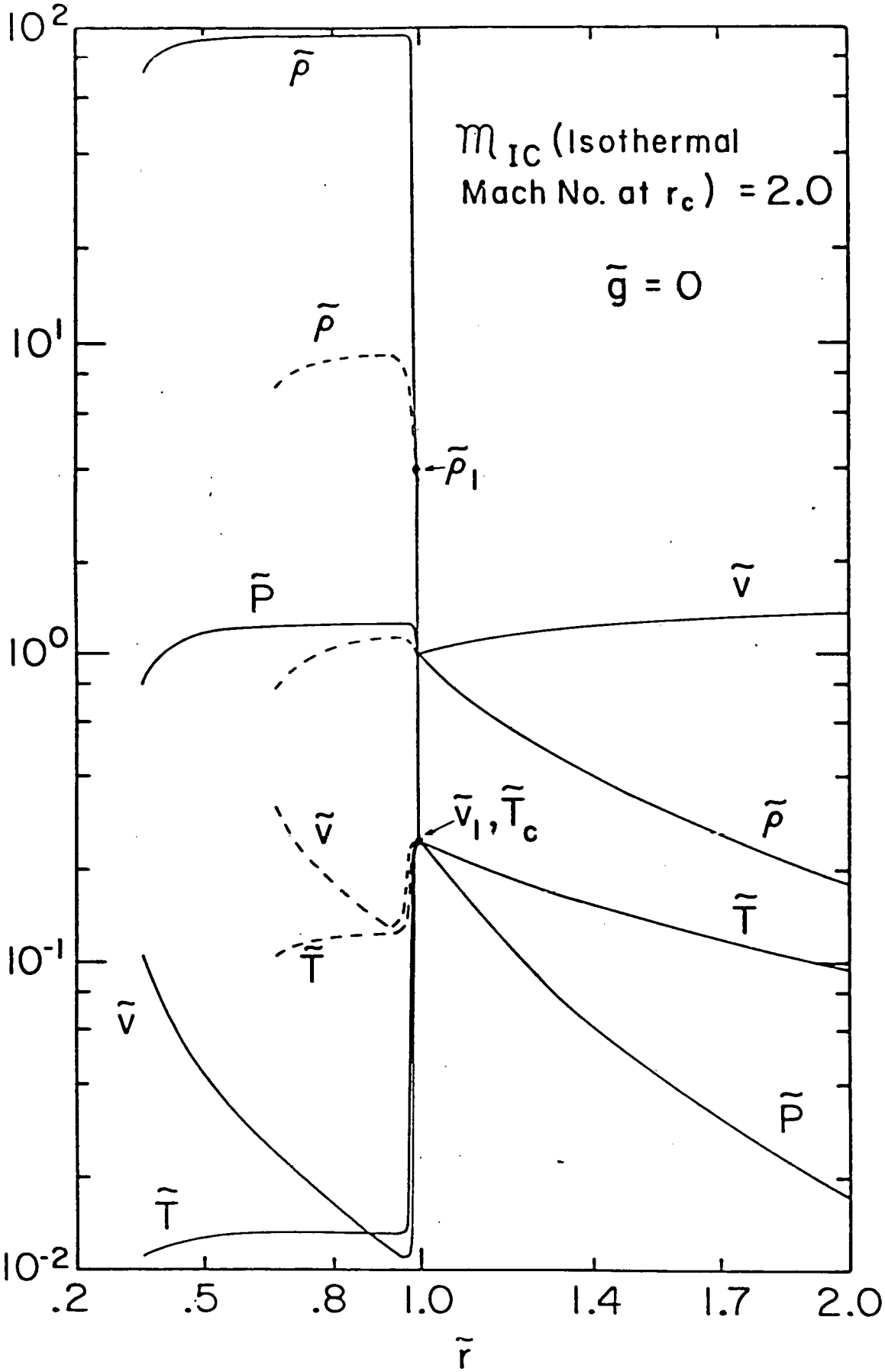
10^2
10^1
10^0
10^{-1}
10^{-2}
$\tilde{\rho}$
$\mathcal{M}_{IC}$ (Isothermal Mach No. at r_c) = 2.0
$\tilde{g} = 0$
$\tilde{\rho}$
$\tilde{\rho}_1$
$\tilde{P}$
$\tilde{v}$
$\tilde{v}$
$\tilde{v}_1, \tilde{T}_c$
$\tilde{\rho}$
$\tilde{T}$
$\tilde{T}$
$\tilde{v}$
$\tilde{P}$
$\tilde{T}$
.2
.5
.8
1.0
1.4
1.7
2.0
$\tilde{r}$

Fig. 14a

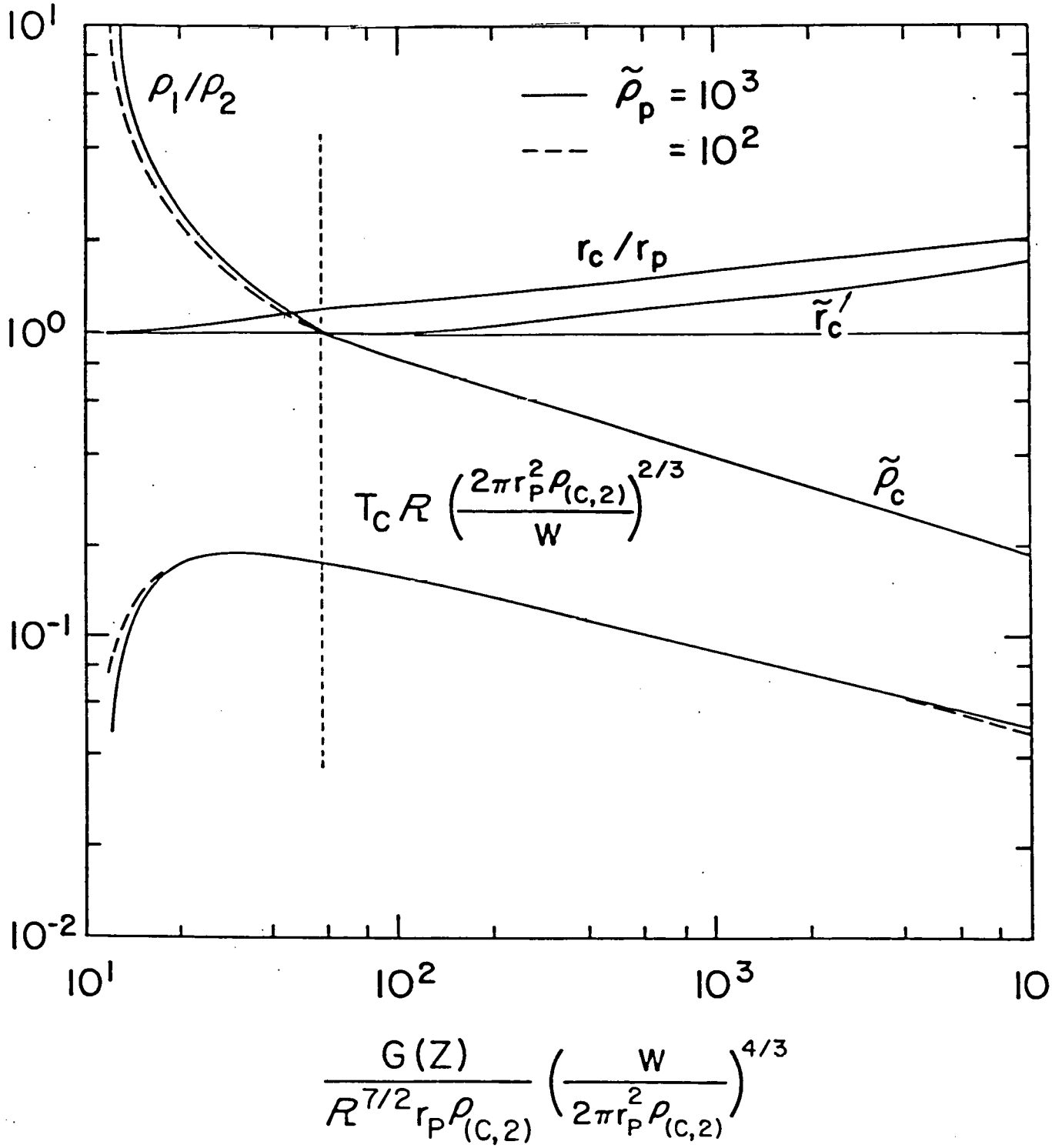
10^1
10^0
10^{-1}
10^{-2}
10^1
10^2
10^3
ρ_1/ρ_2
$\tilde{\rho}_p = 10^3$
$= 10^2$
r_c/r_p
$\tilde{r}_c'$
$\tilde{\rho}_c$
$T_c R \left(\frac{2\pi r_p^2 \rho_{(C,2)}}{W}\right)^{2/3}$
$\frac{G(Z)}{R^{7/2} r_p \rho_{(C,2)}} \left(\frac{W}{2\pi r_p^2 \rho_{(C,2)}}\right)^{4/3}$

Fig 19b

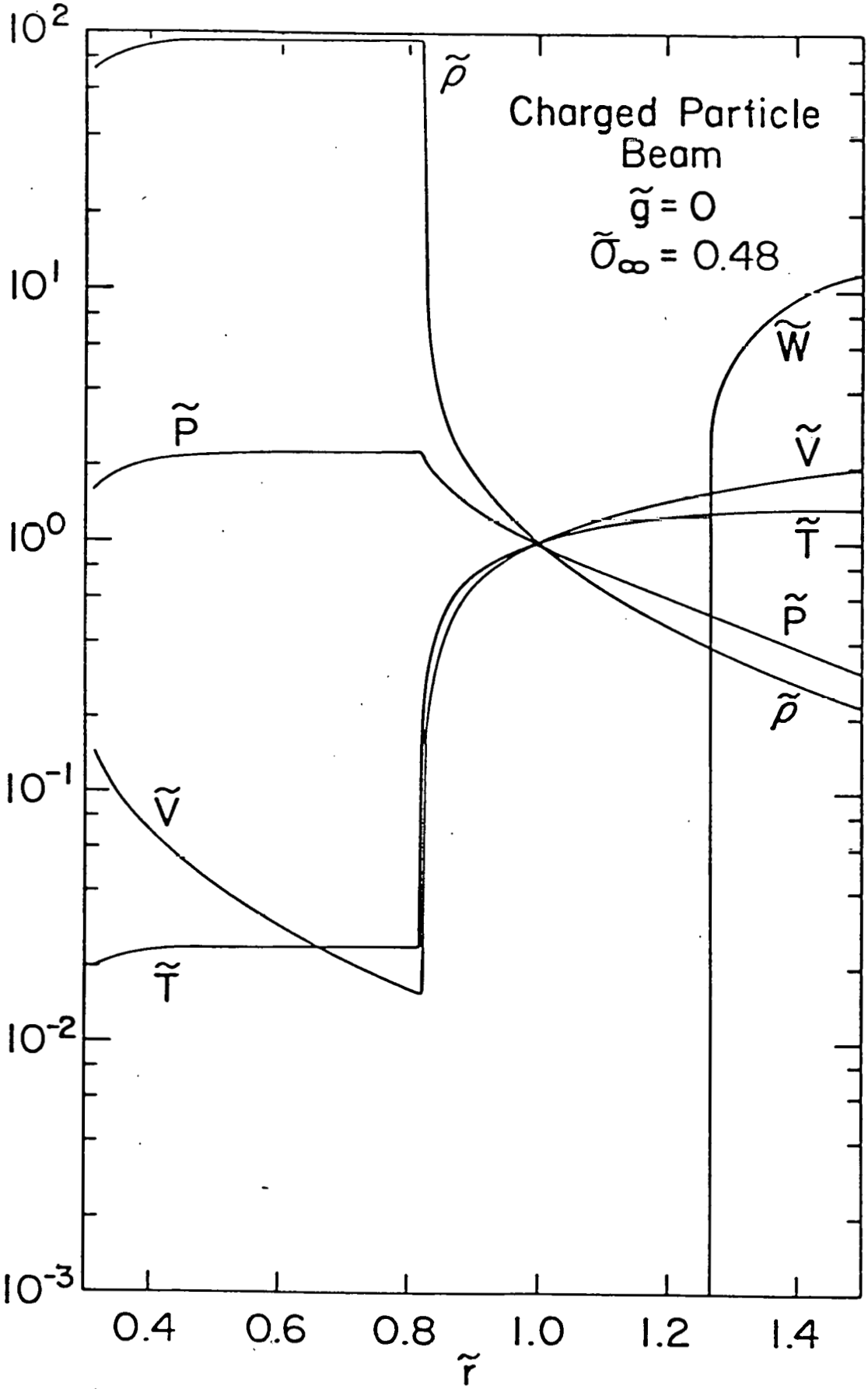
Charged Particle Beam
$\tilde{g} = 0$
$\tilde{\sigma}_\infty = 0.48$
$\tilde{\rho}$
$\tilde{P}$
$\tilde{V}$
$\tilde{T}$
$\tilde{W}$
$\tilde{V}$
$\tilde{T}$
$\tilde{P}$
$\tilde{\rho}$
10^2
10^1
10^0
10^{-1}
10^{-2}
10^{-3}
0.4
0.6
0.8
1.0
1.2
1.4
$\tilde{r}$

Fig 15a

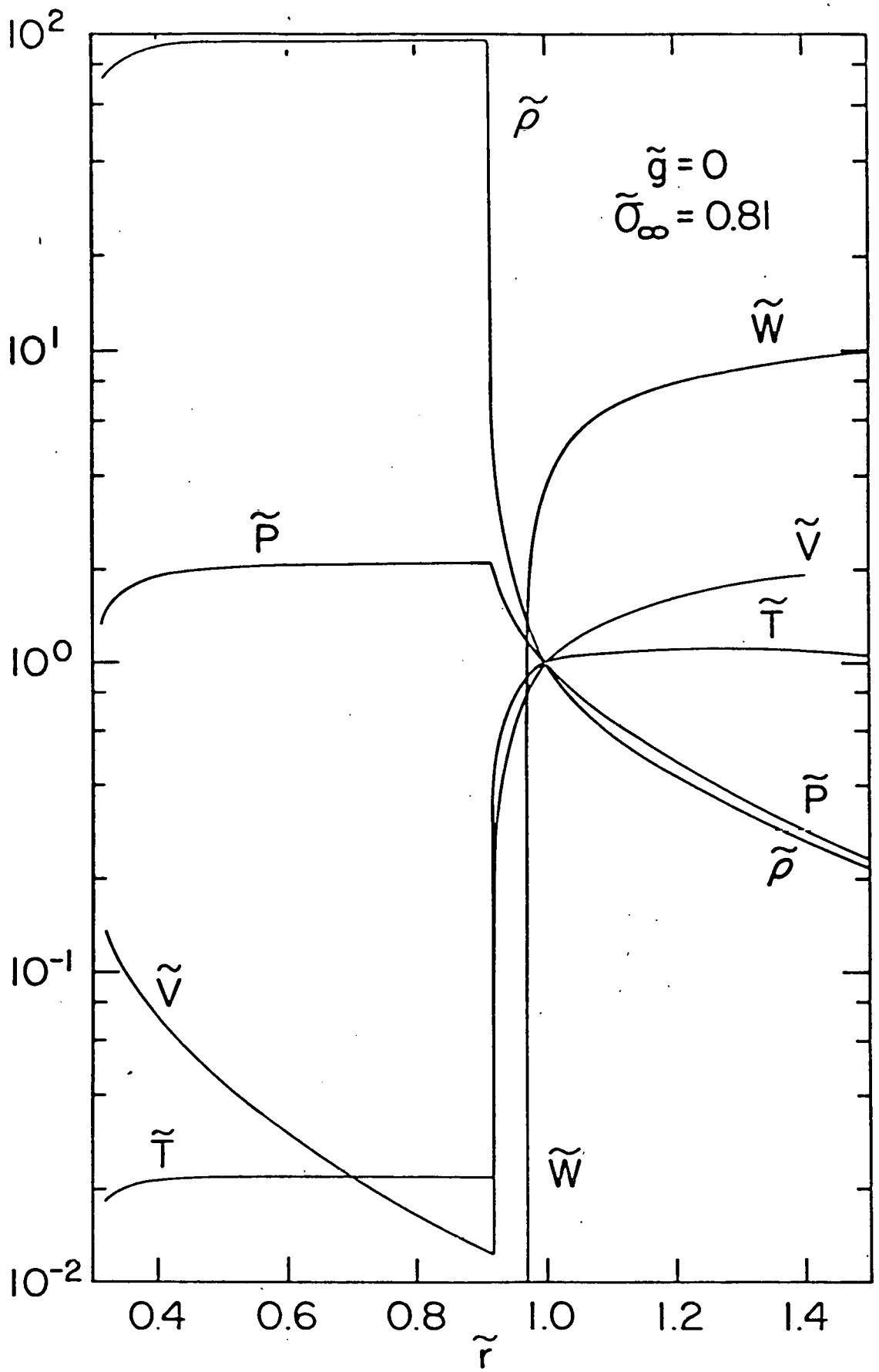
10^2
10^1
10^0
10^{-1}
10^{-2}
$\tilde{\rho}$
$\tilde{g} = 0$
$\tilde{\sigma}_\infty = 0.81$
$\tilde{W}$
$\tilde{P}$
$\tilde{V}$
$\tilde{T}$
$\tilde{P}$
$\tilde{\rho}$
$\tilde{V}$
$\tilde{T}$
$\tilde{W}$
0.4
0.6
0.8
1.0
1.2
1.4
$\tilde{r}$

Fig. 15b

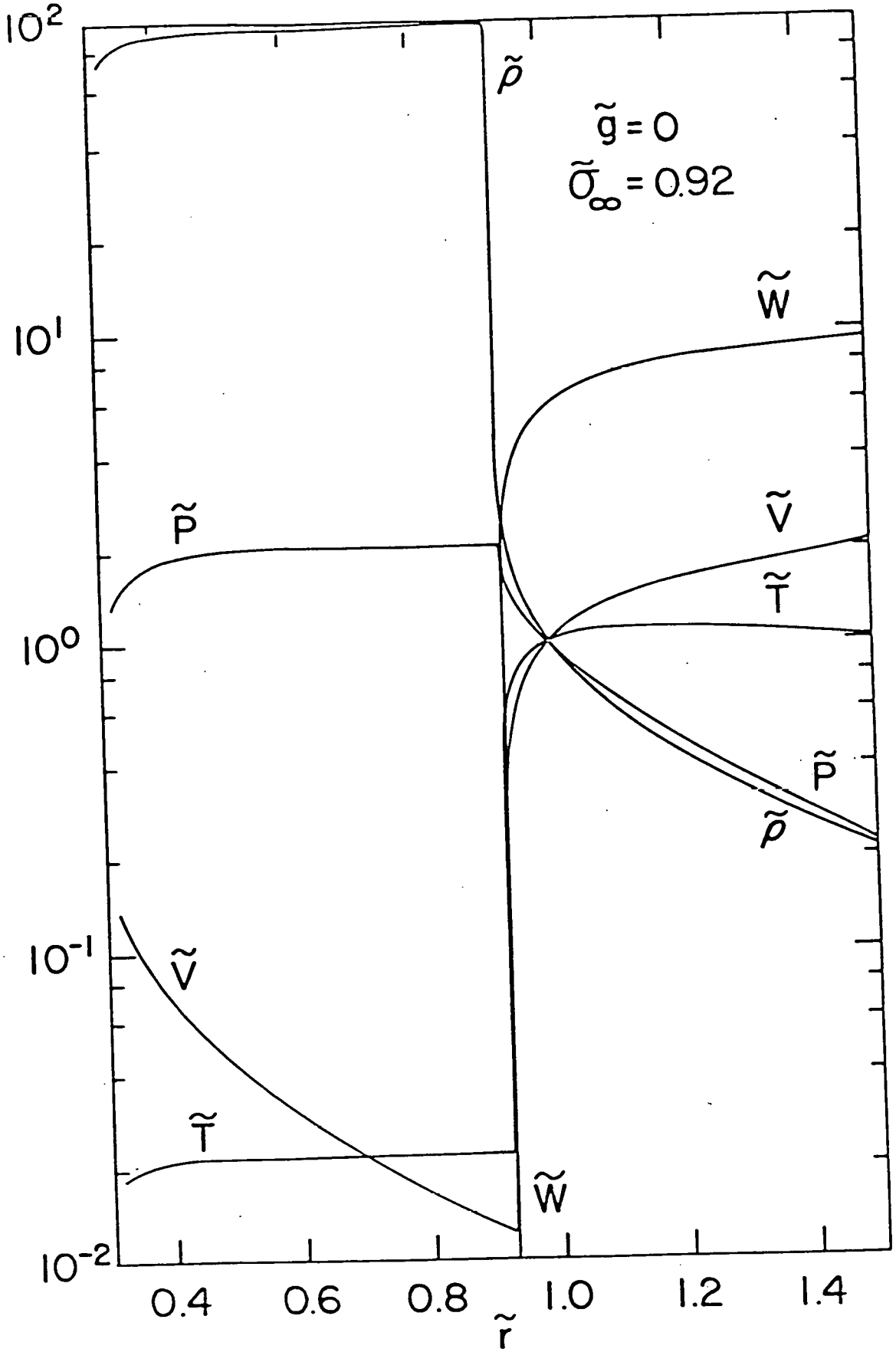
10^2
10^1
10^0
10^{-1}
10^{-2}
$\tilde{\rho}$
$\tilde{g} = 0$
$\tilde{\sigma}_\infty = 0.92$
$\tilde{W}$
$\tilde{P}$
$\tilde{V}$
$\tilde{T}$
$\tilde{P}$
$\tilde{\rho}$
$\tilde{V}$
$\tilde{T}$
$\tilde{W}$
0.4
0.6
0.8
1.0
1.2
1.4
$\tilde{r}$

Fig. 15a

Fig. 16

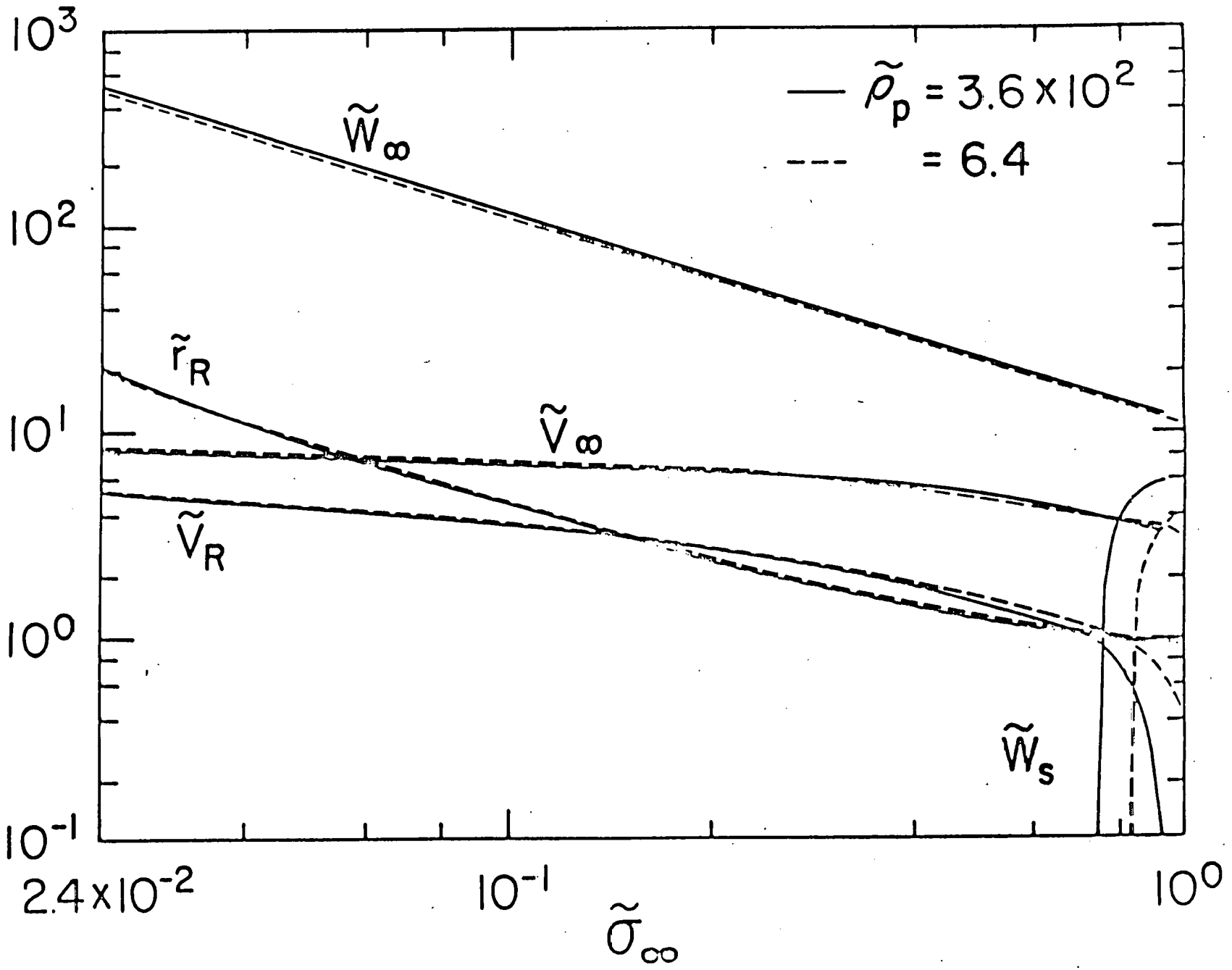
10^3
10^2
10^1
10^0
10^{-1}
$\tilde{W}_\infty$
$\tilde{r}_R$
$\tilde{V}_\infty$
$\tilde{V}_R$
$\tilde{W}_s$
— $\tilde{\rho}_p = 3.6 \times 10^2$
--- $= 6.4$
2.4×10^{-2}
10^{-1}
10^0
$\tilde{\sigma}_\infty$

Paper 3

TAYLOR INSTABILITY IN FUSION TARGETS

R. L. McCrory

University of Rochester, Laboratory for Laser Energetics
Rochester, New York 14623

L. Montierth
R. L. Morse
C. P. Verdon*

University of Arizona, Department of Nuclear Engineering
Tucson, Arizona 85721

ABSTRACT

Optimum performance in laser driven fusion targets is enhanced by the use of high aspect ratio shells in commonly employed spherically symmetric designs. Taylor instability occurs in these systems at (1) the ablation surface when the acceleration is in the same direction as the local density gradient, and (2) later in the implosion process when the fuel decelerates the pusher. Results for a linear stability analysis of the ablation-driven Taylor instability are obtained from a perturbation analysis of the two parameter stationary ablative flow model. The linear growth rates are shown to be in agreement with full two-dimensional numerical simulations. From the linear analysis, the potentially most damaging unstable mode is identified, and full two-dimensional numerical simulations are performed. The two-dimensional calculations determine the nature and saturation behavior associated with the unstable mode. Our results indicate that saturation of the ablatively driven Taylor instability does occur. This saturation occurs at an amplitude which is sufficiently large to be a possible cause of difficulty in using large aspect ratio shells in fusion targets, but is seen to prevent these shells from breaking up and becoming turbulent. It appears plausible that such distorted but laminar, i.e. non-turbulent, shells could be successfully employed in fusion targets.

*Present address: University of Rochester, Laboratory for Laser Energetics, 250 E. River Rd., Rochester, New York 14623

I. INTRODUCTION

Taylor instability is the instability which occurs at the interface of a heavier fluid superposed over a lighter fluid.[1] Gravity causes ripples at the interface to grow until the heavier fluid falls through the lighter, and in the end the heavier fluid comes to rest on the bottom of the container. A modified version of this instability occurs in spherical implosion systems in inertial confinement fusion (ICF) targets, with radial accelerations playing the role of gravity. The most effective implosion systems are particularly vulnerable to this type of instability because they consist of one or more relatively thin spherical shells which accelerate through many times their initial thickness during implosion.[2-7] Figure 1, adapted from Ref. 2, shows density profiles of the standard types of systems. Type IV with "levitated fuel", which is a more elaborate version of Type II, in general gives higher compressions for given constraints on the driver pulse, i.e., laser or particle beam pulse, than do Types I and III.

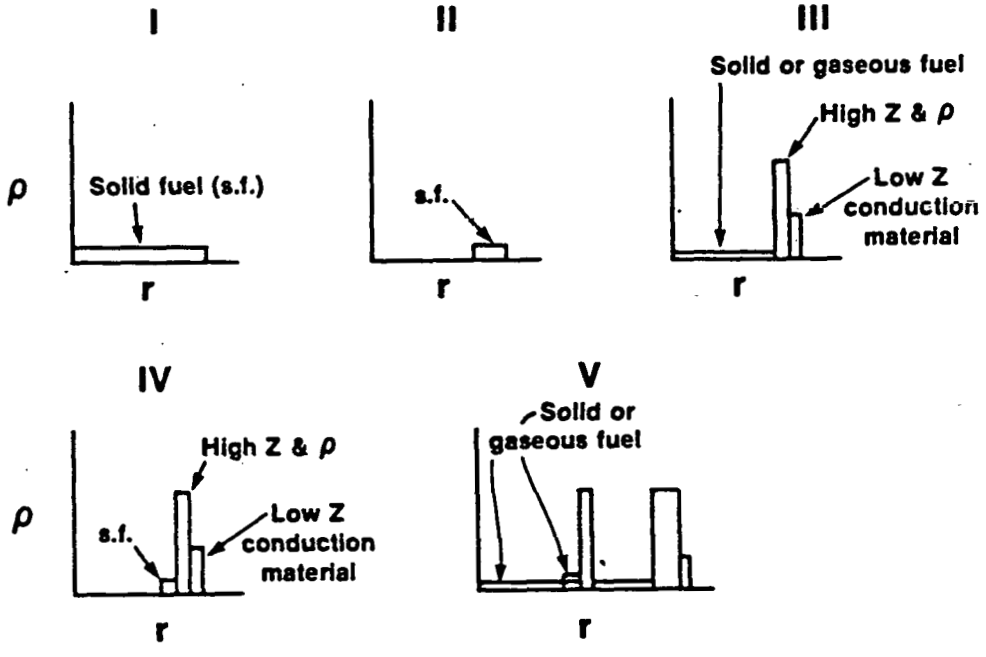

FIG. 1 Five common types of spherically symmetric inertial confinement fusion pellets. (Adapted from Ref. 2).

In general, the larger the initial aspect ratio, $A_o \equiv r_o/\Delta r_o$ (where r_o and Δr_o are initial shell radius and thickness), of the shells, the better the performance of the system. Typical desirable values of A_o are in the range $10 \lesssim A_o \lesssim 100$. The currently popular use of multiple high density shells, of which Type V is a typical example, makes possible various implosion timing improvements at some cost in efficiency, but does not introduce any instability phenomena which are qualitatively different from those found in Types III and IV.

Taylor instability occurs in these systems when and where acceleration is in the same direction as the local density gradient, so that in effect a heavier fluid is above a lighter one in the local gravitational field. This occurs first at the outside surface of the outer shell as illustrated in Fig. 2. The role of the lower density fluid is played by the material which has been heated directly by thermal conduction from the outer high-temperature corona region and is being ablated outwardly from the shell.

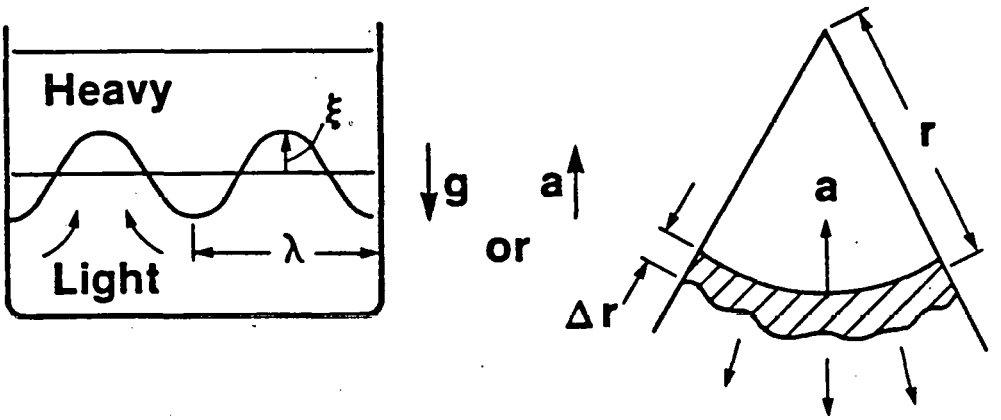

$$\xi = \xi_1 e^{\gamma t}$$

$$\gamma = \left(\frac{2\pi a}{\lambda}\right)^{1/2}$$

FIG. 2 Classical Taylor instability conditions are illustrated by the container of two fluids in a gravitational field, as illustrated in the sketch on the left. The analogous situation for the ablation driven Taylor instability is illustrated on the right.

The inward acceleration causes ripples in the ablation front region to grow unstably. Later, when the fuel has reached the center, the interface between the fuel and the high density pusher shell in Type III or IV systems also becomes unstable, because the pusher is decelerated by fuel pressure.[2]

When successful implosion systems are designed for optimum performance they will probably come as close as possible to failure from Taylor instability without failing. In the manner of failure that would be approached, outside instability could cause growth of shell distortions but not to the point of complete loss of shell integrity at the inner surface. The inside instability would then cause further growth until the interface between the fuel and the pusher shell became so distorted that fuel and pusher material would become intermixed; further fuel compression would cease, and ignition precluded or any thermonuclear burn in progress would be quenched. Because both the inside and outside instability contribute to this failure mode, it will eventually be necessary to calculate the behavior of both in detail to predict and to avert failure. However, at present the outside instability is in a sense more important, because much less is known about it, and because it appears possible that it may not be as troublesome in all cases as has previously been predicted from linear analysis.[2]

The inside instability is usually classical, i.e., ablative phenomena usually do not play a significant role. Classical analytic estimates of growth rates[1] are, therefore, approximately correct, and the nonlinear development can be anticipated from previous numerical simulations of the classical Taylor instability which show the bubble and spike structure.[8-10] In section II below we give a brief description of the analytic theory of these classical growth rates and their application to the implosion of shells. In contrast with the state of understanding of the approximately classical inside instability, there has been no complete systematic treatment of either linear growth rates or nonlinear development of the outside instability, which is more complicated because the heat flow and convection associated with ablation play an important role. Research done on linear growth rates[2,11-14] shows that in cases of interest, ablation phenomena reduce the linear growth rates significantly at shorter wavelengths, but that the growth rates are still large enough to cause serious difficulty.[2,11] There has also been an indication from numerical simulations that nonlinear saturation mechanisms may in some cases limit shell distortion enough to prevent failure.[14] This effect could be very important if it occurs over a sufficient range of parameters to make usable large aspect ratio systems which would be expected to fail from a simple extrapolation of linear theory.

Preliminary results are presented below from two separate sets of calculations of the behavior of ablation-driven Taylor instability. The first (Section III) is a parameter study of linear growth rates which is based on zero-order stationary ablative flow solutions. The second (Section IV) is a numerical simulation study of nonlinear development done with a two-dimensional, triangular zone, Lagrangian hydrodynamic and heat flow code which was developed for this purpose. From the linear growth rates, it will be possible to determine, for a given implosion system, the range of modes which grow enough that failure should be expected from extrapolation of linear theory. The two-dimensional simulations should then show which of these modes would be prevented by nonlinear effects from growing to sufficiently large amplitude to cause failure and, therefore, which systems should be expected to implode successfully.

II. CLASSICAL ESTIMATES OF SHELL INSTABILITY

Figure 2 shows the classical Taylor instability conditions in the container of the two fluids in a gravity, g, on the left and the analogous situation on the outside of the shell on the right, which is being given an inward acceleration, a, by ablation pressure at the outside surface. Suppose the amplitude of the ripple of the interface between the two fluids in the container has the form,

$$\xi = \xi_0 \exp(ikx + \gamma t), \tag{1}$$

where x is the coordinate parallel to the interface,

$k \equiv 2\pi/\lambda$, and

ξ_0 is the amplitude at $t = 0$.

If the fluids are incompressible and inviscid, the thicknesses of the fluid layers are great compared to the ripple wavelength, λ, and the heavy fluid is much more dense than the light fluid; then the growth rate, γ, is

$$\gamma = (gk)^{1/2} . \tag{2}$$

To the extent that classical theory is at all applicable to the ablative outside surface, the assumption that the heavy fluid is much more dense than the light is a good approximation. This is so, because typical density ratios across the ablation front from the shell, which is the heavy fluid, to the ablated material near the isothermal sonic point of the flow (which is a reasonable place to define the lower density) are of the order of 10^2.

Failure

From this classical theory, estimates can be made of the conditions under which shell failure would occur. The subject of failure is not well understood, but it is expected that failure would occur if the surface ripple amplitude became of the order of or larger than the shell thickness at the time of failure. If we accept this criterion for failure, then from the definition of aspect ratio, $A \equiv r/\Delta r$, the failure amplitude, ξ_f, is

$$\xi_f = \Delta r = r/A \ . \tag{3}$$

Here all quantities are taken not at initial time but at the time of t_f, when failure occurs. That is, t_f is the time when the failure criterion is first met, even though shell distortions may increase after this time. To obtain numerical estimates that indicate the magnitude of the problem, we must choose the values of k that will be most troublesome, and this we do according to the conventional wisdom, to which the authors at least partly subscribe. That is, the most troublesome mode is the fastest-growing mode that can cause the shell to break up. From Eq. (2) the growth rate increases with k. On the other hand, the e-folding depth of penetration of the k mode into the fluid from the interface is k^{-1}, and nonlinear calculations indicate that growth slows from exponential to linear, or in some cases, saturates turbulently and stops when the amplitude reaches this penetration length. Modes with values of k^{-1} less than the shell thickness, the conventional wisdom dictates will not cause the shell to break up and are not as troublesome as the slightly slower modes that can cause break up.

This worst value of k is then $k_w \approx \Delta r^{-1}$, or since for large ℓ $k \approx \ell/r$, we also have a corresponding worst ℓ, and, from Eq. (3)

$$\xi_f = k_w^{-1} = \frac{r}{\ell_w} = \frac{r}{A} \ . \tag{4}$$

Substituting Eq.(4) into Eq.(2) gives the growth rate for the "worst" mode:

$$\gamma_w = \left(\frac{Ag}{r} \right)^{\frac{1}{2}} \ . \tag{5}$$

It should be noted that A here is the in-flight aspect ratio, as discussed below, not the initial aspect ratio A_0. Substituting Eq.(5) into Eq.(1) gives the amplification of the "worst" mode,

$$\xi = \xi_0 \exp \left[\left(\frac{Ag}{r} \right)^{\frac{1}{2}} t \right] \ . \tag{6}$$

The larger t can be, that is, the longer the instability has to grow, the smaller ξ_0 must be to prevent failure, and practical

limits on surface finish put lower limits on ξ_o. The procedure to follow is then to estimate the minimum value of ξ_o and the maximum value of t and to ask if the resulting ξ exceeds ξ_f from Eq.(3). It is tempting to assume that failure can occur as late as the full implosion time, τ_I, defined as

$$\tau_I \equiv \left(\frac{2r_o}{g} \right)^{1/2} . \tag{7}$$

This is simply the time required for a shell to reach the origin if it implodes with a constant acceleration, g. This, however, is probably a bit pessimistic in the sense that it allows more time for the instability to develop than is actually available, for several reasons. First, the outer shell surface does not travel all the way to the origin, because the compression is finite. In high compression ICF systems, however, the outer surface does travel well over half way. Spherical convergence makes a further contribution to limiting growth time. In most cases of interest, as the shell moves toward the origin, its aspect ratio first increases rapidly because the shell is made thinner by shock and acceleration-induced compression. Typically A increases from A_o by a factor of 4 or a bit more. A then changes slowly for an intermediate period during which the effects of convergence and ablative mass removal roughly cancel. In cases of interest, which do not burn through, the convergence then finally wins; the shell thickens while the radius decreases, and A decreases again. It is during the intermediate period when A is largest and the shell is near its initial radius, r_o, that the shell is most vulnerable to break up by the larger ℓ (or k) faster growing modes. Thereafter, as A decreases, it is expected that further growth of the higher ℓ modes will have relatively less disruptive effects on the shell. For these reasons in applying Eq.(6), we choose $t_f = \tau_I/2$, $A = 4A_o$, and $r = r_o$. These choices of "round numbers" all appear to err a bit in the direction of underestimating growth of unstable modes. Substituting into Eq.(6) gives the initial perturbation amplitude, ξ_o, which would cause failure:

$$\xi_o = \frac{r_o}{4A_o} \exp \left[-\left(\frac{4A_o g}{r_o} \right)^{1/2} \frac{\tau_I}{2} \right]$$

$$= \frac{\Delta r_o}{4} \exp \left[-(2A_o)^{1/2} \right] . \tag{8}$$

Notice that the acceleration, g, has cancelled out. To see what this means, consider a typical case of interest: $A_o = 25$ and $r_o = 100$ μm. From Eq.(8) the requirement to avert failure is $\xi_o \leq 8.5 \times 10^{-8}$ cm. Without going into the particulars of the possible spectra of shell surface imperfections responsible for ξ_o, it can be seen that this requirement places severe

restrictions on the surface finish. If instead $A_0 = 10$, then the requirement is $\xi_0 \leq 2.8 \times 10^{-6}$, and if $A_0 = 5$, then $\xi_0 \leq 2.1 \times 10^{-5}$. Only the requirement for A = 5 represents a surface finish which seems clearly attainable.

Linearized calculations presented in Ref. (2), which include ablative effects, obtain amplifications which are a bit smaller than, but within an order of magnitude of those obtained from Eq.(6) above. From these more realistic calculations and slightly more conservative estimates of attainable surface finish, Ref. 2 also concluded that $A_0 \leq 5$ is required to avert shell breakup. Clearly if anything can be done to relax this restriction, it would be very desirable, because the performance expected from shells with $A_0 < 5$ is rather disappointing.

Compressibility Correction

There is a further correction to the classical linear growth rates that is caused by compressibility, which may be important, and should be pointed out before the ablative calculations are presented. In the classical calculations[1] it is assumed that the fluids are incompressible. For present purposes this is essentially equivalent to assuming that the linear growth time of a mode, $\tau \equiv \gamma^{-1}$, is greater than the acoustic transit time, τ_s, across the characteristic length of the mode structure. That is, since the characteristic length of a Taylor mode is k^{-1}, it is implicitly assumed that

$$\gamma \leq k C_s , \tag{9}$$

where C_s is the sound speed in the shell. A Taylor mode cannot in fact grow much faster than the upper limit given by the equality in Eq.(9), because the pressure differences that cause the flow cannot be transmitted across the mode structure on a shorter time scale. In ideal gases, the sound speed is

$$C_s = \left(\frac{5P}{3\rho} \right)^{1/2} , \tag{10}$$

where P and ρ are pressure and density, and the pressure in a shell at the outside, or ablation, surface is approximately given by the effective weight per unit area of the shell on the ablation surface,

$$P = (\rho a \Delta r_f) . \tag{11}$$

Here for consistency with the estimates of growth rates above, the final shell thickness, Δr_f, is used as an estimate of the in-flight thickness, Combining Eqs. (9), (10), and (11) gives

$$\gamma \leq k\left(\frac{5a}{3}\,\Delta r_f\right)^{1/2} = (ak)^{1/2}\left(\frac{5k}{3}\,\Delta r_f\right)^{1/2} = k\left(\frac{5}{3}\,\frac{ar_f}{A}\right)^{1/2} . \quad (12)$$

Comparison of Eq. (12) with (2) above, with $a = g$, shows that in the "worst case" discussed above, for which $k_w\,\Delta r_f = 1$, Eq. (12) places an upper limit on γ which is larger than the classical growth rate but only by a factor of $(5/3)^{1/2}$. For smaller values of k, it is seen that Eq. (12) limits γ to values which are smaller than the classical incompressible result. It will in fact be seen in section III that for a range of smaller values of k below k_w, Eq. (12) becomes approximately the correct expression for γ, instead of Eq. (2). If nonlinear saturation prevents shell breakup from modes with $k \leq k_w$, this reduction in linear growth rates for smaller k may then be important.

III. CALCULATION OF LINEAR GROWTH RATES USING THE STEADY FLOW MODEL

Exact calculation of amplification of linearly unstable Taylor modes during an implosion requires calculation of the development in time of first-order perturbations of a time-dependent zero order flow. The separation into modes occurs naturally through an expansion of the angle dependence in the spherical harmonics, $Y_\ell^m(\theta,\psi)$. The various first-order quantities then appear in the form $f_{1\ell}(r,t)\cdot Y_\ell^m(\theta,\psi)$, where $f_{1\ell}$ is one of the first-order quantities, $\rho_{1\ell}$, $T_{1\ell}$, the radial component of the perturbed velocity, $V_{1r\ell}$ or ξ_r, the perturbed displacement, or the divergence of the corresponding angular components of these two quantities, $\nabla\cdot\vec{V}_{1\Omega\ell}$ and $\nabla\cdot\xi_\Omega$. The system of coupled differential equations for these $f_{1\ell}$'s is degenerate with respect to m and decouples with respect to ℓ.[12-14] The different modes are, therefore, identified by their ℓ number. Solution consists of numerical integration in time of the system of equations for the $f_{1\ell}$'s for as many different ℓ's as are desired. The zero-order quantities, the $f_0(r, t)$'s, which describe the spherically symmetric implosion, appear as coefficients in the system of equations for the $f_{1\ell}$'s and can be computed simultaneously or computed previously and stored.

This exact method of solution has been applied successfully to implosions of shells[2,13,14] and will probably be necessary for detailed examination of specific fusion target designs in the future. However, the method in a sense gives too much information for making qualitative, i.e., order of magnitude, judgments about broad classes of implosion systems. Total amplifications of perturbations are obtained for a specific implosion system driven by a specific incident driver pulse. In practice, this solution space has so many parameters that extracting patterns of behavior and insight from it can be a bit tedious.

What is needed to complement these exact calculations of total linear amplifications is the instantaneous linear growth rates of the Taylor modes as a function of ℓ for the minimum number of fundamental parameters needed to describe the instantaneous state of an unstable region. The classical theory, of which Eq. (2) is a simplified form, fills this need for non-ablative unstable regions when, as discussed below, the compressibility corrections are added. The numerical calculations of growth rates of ablation-driven Taylor instability presented here are intended to fill the similar need for ablative regions where heat flow and convection are important.

An appropriate family of zero-order ablative flow solutions from which to derive instantaneous growth rates is obtained from the steady flow model.[15,16] In cases of interest, the instability growth time is short compared to the implosion time, i.e., the time for shell density, temperature, and velocity profiles to change significantly. However, the growth time is not necessarily shorter, and can be longer, than the characteristic time for a fluid element to flow through the ablation front region. By being stationary in time while including the effect of convection, the steady flow model meets the requirements of this ordering of times, but is simple enough that the family of solutions may be described by a two parameter family. A brief description of the steady flow model and solutions will be given next, before the stability calculations are presented.

Steady Flow Model

In this model, the flow is spherically symmetric, radially outward, and stationary. Stationary flow is a reasonable approximation in most cases of interest, because the time required to establish the flow between the pellet surface and the region where the absorbed energy is assumed to be deposited is less than the characteristic implosion time and, because the pressure gradient forces in the ablation region are larger than the forces associated with the average inward acceleration.

For our purposes, very little generality is lost and considerable simplicity is gained, by assuming a single temperature instead of separate electron and ion temperatures. The steady-state hydrodynamic equations are then:

Continuity:

$$\frac{d}{dr}(\rho v r^2) = 0 , \tag{13}$$

Momentum:

$$\rho v \frac{dv}{dr} = - \frac{dP}{dr} - \rho \frac{d\psi}{dr} , \quad \text{and} \tag{14}$$

Energy:

$$\frac{1}{2} v^2 + \frac{\gamma_c}{\gamma_c - 1} \frac{P}{\rho} + \psi - \Omega = \frac{1}{2} v_b^2 , \tag{15}$$

where ρ is the fluid mass density, v is the radial fluid velocity, r is the radius, P is the pressure, ψ is the gravitational potential, γ_c is the ratio of specific heats, and v_b is the Bernoulli energy flow constant. The gravitational potential, ψ, which is introduced to represent inward acceleration must be included to yield shell-like density profiles. The quantity Ω is defined to be $\Omega = (\sigma\kappa/S)(dT/dr)$, where $S = 4\pi r^2 \rho v$ is the mass flux, a constant of the motion by Eq. (13). κ is the thermal conductivity coefficient given by

$$\kappa = G(Z)\, T^{\alpha}\, \rho^{-\beta} . \tag{16}$$

Following Spitzer[17] we take $\alpha = 5/2$, $\beta = 0$, and $G(Z) = \kappa_0/Z$, where κ_0 is a constant, for most of what follows. We have ignored the weak temperature and density dependence in the $\ln\Lambda$ term which appears in the conductivity,[17] T is the temperature, and we have defined $\sigma = 4\pi r^2$. P is related to T through the fully ionized ideal gas equation of state $P = \rho RT/\mu$, where R is the gas constant, $\mu = \mu_0/(1 + Z)$, μ_0 is the atomic mass of the fluid, and Z its atomic number. After some manipulation, Eqs. (13), (14), and (15) become:

$$\rho v \sigma = S , \tag{17}$$

$$v\left(1 - \frac{RT}{\mu v^2}\right) \frac{dv}{dr} = \frac{RT}{\mu} \left(\frac{2}{r} - \frac{1}{T} \frac{dT}{dr}\right) - \frac{d\psi}{dr} , \tag{18}$$

$$\frac{1}{2} v^2 + \frac{\gamma}{\gamma - 1} \frac{RT}{\mu} + \psi - \frac{\sigma}{S} \kappa \frac{dT}{dr} = \frac{1}{2} v_b^2 . \tag{19}$$

Because transonic solutions are of particular interest to us, it is useful to scale the equations in the following way. Define $\tilde{\rho} = \rho/\rho_s$, $\tilde{T} = T/T_s$, $\tilde{v} = v/v_s$, $\tilde{\psi} = \psi/v_s^2$, and $\tilde{r} = r/r_s$, where ρ_s, T_s, and v_s are the values of the flow variables at the *isothermal* sonic point r_s; that is, at r_s, $v_s = (RT_s/\mu)^{1/2}$. Using this scaling, Eqs. (18) and (19) become:

$$\frac{d\tilde{v}}{d\tilde{r}} = \frac{1}{\tilde{v}} \frac{\tilde{T}\left(\frac{2}{\tilde{r}} - \frac{1}{\tilde{T}}\frac{d\tilde{T}}{d\tilde{r}}\right) - \frac{d\tilde{\psi}}{d\tilde{r}}}{\left(1 - \tilde{T}/\tilde{v}^2\right)} \quad , \text{ and} \tag{20}$$

$$\frac{d\tilde{T}}{d\tilde{r}} = \frac{M\left[\tfrac{1}{2}(\tilde{v}^2 - \tilde{v}_b{}^2) + \frac{1}{\gamma - 1}\tilde{T} + \tilde{\psi}\right]}{\tilde{r}^2(1 + \beta)\tilde{T}^{\alpha}\tilde{v}^{+\beta}} \quad . \tag{21}$$

The dimensionless quantity M is defined as

$$M = \frac{r_s \rho_s{}^{1+\beta} v_s{}^3}{G(Z) T_s{}^{1+\alpha}} = \frac{r_s \rho_s v_s{}^3}{k_s T_s} \quad , \tag{22}$$

and is the only place in the equations where dimensional parameters appear explicitly.

For use in Eq. (20), we define $\tilde{g} = -\partial\tilde{\psi}/\partial\tilde{r}$. The form of ψ that has been used is $\psi = -g(r - r_s)$, or $\tilde{\psi} \equiv -\tilde{g}(\tilde{r} - 1)$, where the dimensionless form of the gravity constant then becomes $\tilde{g} \equiv g r_s / v_s{}^2$.

The numerical solution of Eqs. (20) and (21) is accomplished by integrating inward ($\tilde{r} < 1$) and outward ($\tilde{r} > 1$) from the singularity of Eq. (20) at $\tilde{r} = 1$. We further restrict our attention to solutions which are subsonic for $\tilde{r} < 1$ and supersonic for $\tilde{r} > 1$. We require that $d\tilde{v}/d\tilde{r}$ be finite at $\tilde{r} = 1$. Thus, since the denominator of the right-hand side of Eq. (20) becomes zero at $\tilde{r} = 1$, the numerator must also be zero there. Values of the temperature and velocity derivatives at this singularity are determined as a function of M and $\tilde{g}$ by requiring that the solutions be continuous there. Limits on the range of values of M are also determined, as a function of $\tilde{g}$, by conditions at $\tilde{r} = 1$, i.e., $r = r_s$. These constraints, as well as the procedure for treating the laser energy deposition at a critical surface, and some asymptotic analytic solutions for $r \to \infty$ are derived in Ref. 15.

It is also shown that values of M near the lower limit of the allowed range correspond to larger values of the ratio $\tilde{\rho}_p \equiv \rho_p/\rho_s$ of the peak density at the outer shell surface ρ_p, to the sonic point density, ρ_s.

For present purposes, the driver energy is assumed to be deposited at larger radii than are directly involved in the stability calculations, i.e., at $r \to +\infty$. In other applications of the steady flow model, the driver energy is explicitly introduced at finite radii[15], such as the critical surface of laser light, and one or more additional parameters are introduced, which are not necessary for the present requirements here.

The solutions of Eqs. (21) and (22) form a two-parameter family. The two parameters are M and $\tilde{g}$, but M, whose physical meaning is not transparent, is equivalent to the ratio of peak shell density to the sonic density. That is, M is found to be equivalent to $\tilde{\rho}_p \equiv \rho_p/\rho_s$ where ρ_p is the peak density of the shell or pellet. Cases of interest for laser fusion applications have values of $\tilde{\rho}_p$ of the order of 10^2. All other things being equal, larger $\tilde{\rho}_p$ corresponds to smaller incident power. Values of $\tilde{\rho}_p$ of the order of 10 or less approach the rapid thermal burn through limit where exploding pusher behavior accurs. It may be interesting to the reader to note from Eq. (20) that $\tilde{g}$ (defined as $-\partial\tilde{\psi}/\partial\tilde{r}$) is effectively a measure of the relative importance of spherical divergence and acceleration in determining the flow in the sonic region. The limit $\tilde{g} << 1$ gives solutions in which acceleration is unimportant, and the shells are so thick that $A \lesssim 1$. As $\tilde{g} \to \infty$, $A \to \infty$, spherical curvature is not important, and flat slab solutions are obtained for this limit. For ICF applications, solutions with $\tilde{g}$ of order 1 are often most relevant, as we discuss below. Figure 3 shows the steady flow solution profiles for the particular case $\tilde{\rho}_p = 50$ $\tilde{g} = 1.0$, and represents one of the particular cases for which instability growth rates and mode forms are obtained by the procedures described in the following section.

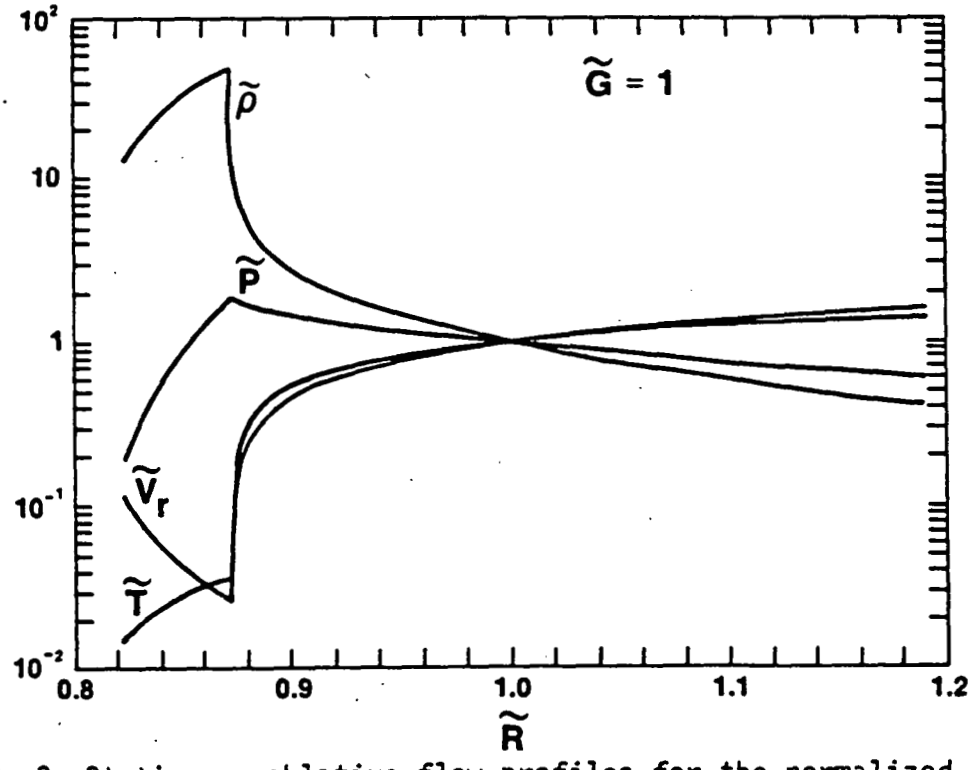

FIG. 3 Stationary ablative flow profiles for the normalized density ($\tilde{\rho}$), pressure ($\tilde{P}$), velocity ($\tilde{V}_r$), and temperature ($\tilde{T}$) obtained for the case $\tilde{G} = 1$. The flow variables are normalized at the isothermal sonic point ($\tilde{R} = r/r_s = 1$).

A further transformation of parameters is useful for applications of the steady flow solutions and their stability properties to implosion systems. The aspect ratio, A, defined in Section II above, is defined from each computed solution as the width of the shell density profile at half height. This is the first transformed parameter. The second parameter is the fraction of the shell mass that is removed by ablation during the implosion time τ_I, defined in Section II. If M and ΔM are the initial mass and the ablated mass increment respectively, this burn through parameter is then

$$B \equiv \frac{\Delta M}{M} = \frac{S\tau_I}{M} = \frac{(\rho_s r_s^2 v_s)\tau_I}{M} = \left(\frac{r_p}{r_s}\right) \frac{\tau_I}{\tilde{g}} \left(\frac{r_s^3 \rho_s}{M}\right). \qquad (23)$$

Figure 4 illustrates the dependence of A on $\tilde{g}$ and $\tilde{\rho}_p$. Note the linear dependence of A on $\tilde{\rho}_p$ and on $\tilde{g}$ for large $\tilde{g}$ and $\tilde{\rho}_p$. Figure 5 shows the full mapping from the solution parameters $(\tilde{\rho}_p, \tilde{g})$ to the parameters (A,B). Maximum energy transfer is achieved from the energy source driving the ablation to part of the imploding shell that is not ablated if $\Delta M/M$ is about 2/3, just as one would expect in analogy with a "rocket model"[18] to which this system is approximately equivalent. Taking into account the approximations involved, one then expects the optimum solutions to be in the range $0.5 < B < 1.0$. Other implosion system design constraints could, however, lead to the use of solutions outside of this range. From Fig. 5 it is seen that this range of B values and aspect ratios in the popular range $10 < A < 100$ requires solutions in the neighborhood of $\tilde{\rho}_p = 50$ to 100 and $\tilde{g} = 1.0$.

Method of Calculating Perturbations

The method used here is similar to that used in Refs. 12-14, and described briefly above, except that the equations for the time dependence of the perturbed quantities are written in Eulerian form and solved on a regular fixed grid instead of being written in Lagrangian form. This procedure was adopted because the zeroth order steady flow solutions are computed on a regular fixed Eulerian grid, as opposed to the procedure used when the exact zeroth order solutions of Refs. 12-14 are computed which employ a Lagrangian grid moving with the fluid. In either case, it is desirable, for simplicity and accuracy, to have the first and zeroth order computations done on the same grid. The first order equations are obtained by expansion of the angle dependence in spherical harmonics, $Y_\ell^m(\theta,\psi)$, and make use of the fact that the resulting system of equations decouple with respect to ℓ and are degenerate with respect to m. These equations are, therefore, the same as those derived in Ref. 12, except for the differences required by the change from Lagrangian to Eulerian coordinates and will not be written out here.

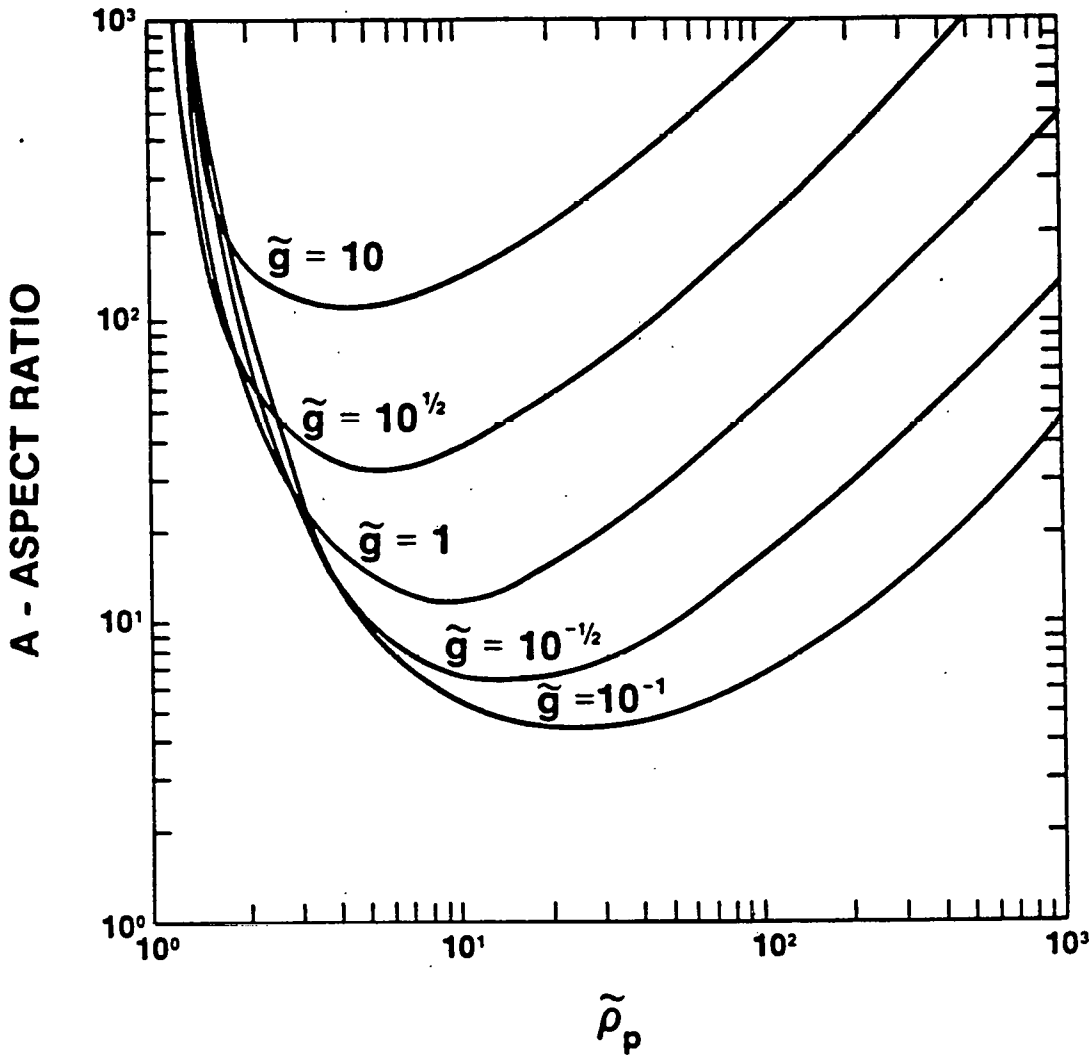

FIG. 4 Dependence of the aspect ratio, A, as a function of $\tilde{\rho}_p$ for various values of the normalized acceleration, $\tilde{g}$ obtained from the two parameter stationary ablative flow model. Note the linear dependence of aspect ratio on $\tilde{\rho}_p$ for large $\tilde{\rho}_p$, $\tilde{g}$.

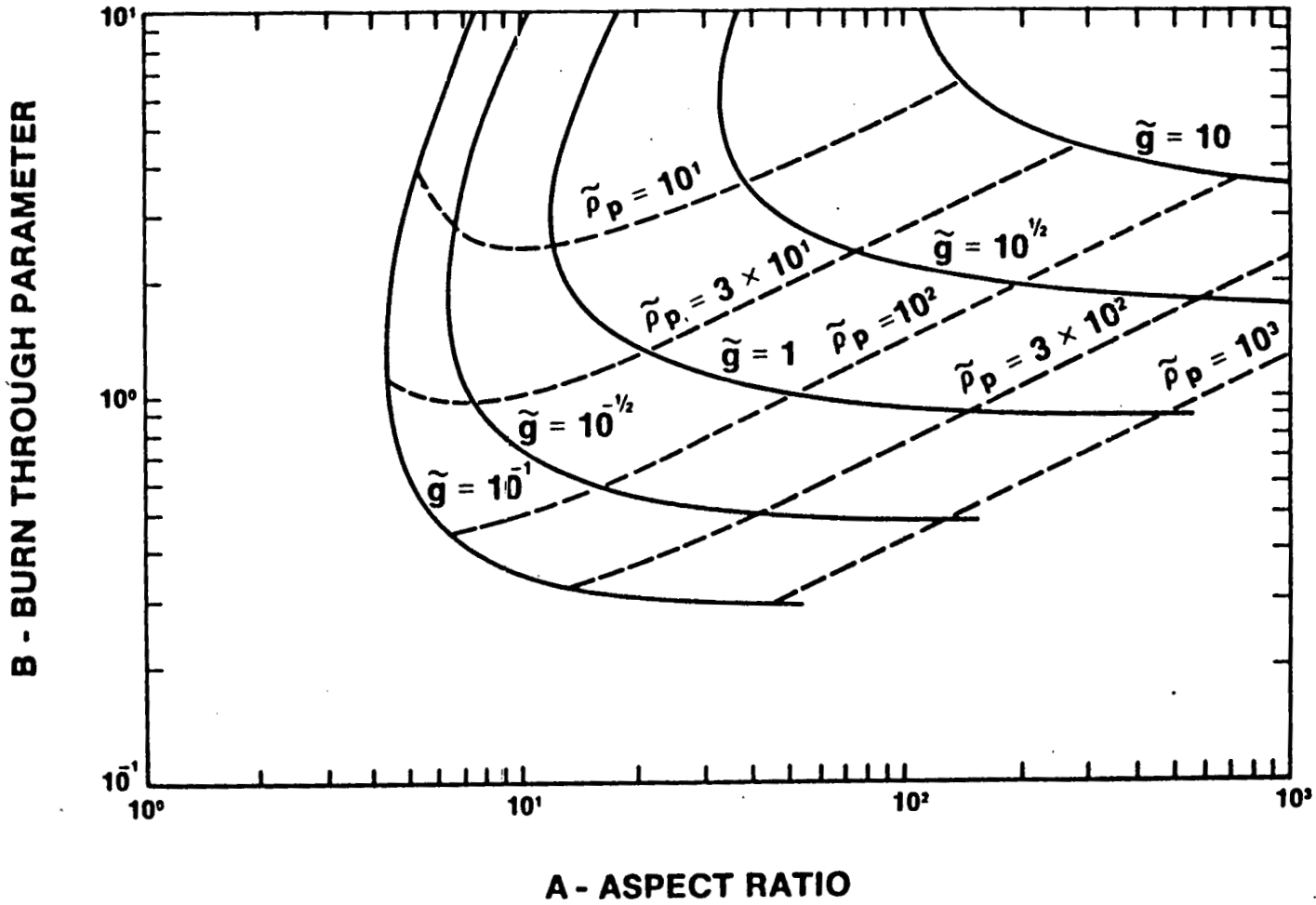

FIG. 5 Full mapping from the solution parameters ($\tilde{\rho}_p$, $\tilde{g}$) to the parameters (A,B) from the stationary ablative flow model. A is the shell aspect ratio, and B is the burn through parameter, defined in the text, (Eq. 23), $B = \Delta M/M$.

The first order variables are T_1, ρ_1, $\bar{v}_1$, and $\bar{\xi}$, the perturbed temperature, density, velocity, and displacement. All scalar quantities have the form $T_1 = T_1(r,t)Y_\ell^m(\theta,\psi)$ as described near the beginning of this section. The zeroth order quantities obtained from the steady flow model appear as coefficients in the equations of motion for the first order variables. The displacement, $\bar{\xi}$, is the distance between the perturbed and unperturbed positions of a fluid element and is introduced primarily as a diagnostic variable. $\bar{\xi}$ is a measure of shell distortion and is obtained by integrating

$$\frac{D\bar{\xi}}{Dt} \equiv \frac{\partial\bar{\xi}}{\partial t} + (\bar{v}_0\cdot\bar{\nabla})\bar{\xi} = \bar{v}_1 \ . \qquad (24)$$

The mode form and growth rates for a given ℓ are obtained from the equations of motion for the perturbations by introducing an arbitrary initial perturbation (in practice a Gaussian perturbation of $\rho_1(r)$ localized near the ablation surface of width $2\pi r/\ell$ was used) and integrating the equations in time until the form of the mode and the growth rate of its amplitude become approximately constant. In this way, the fastest growing mode with the given ℓ and its growth rate are obtained.

Results

Figure 6 shows the growth rates for three zero-order steady flow solutions with $\tilde{\rho}_p(\equiv \rho_p/\rho_s) = 50$. The zeroth order solution with $\tilde{g} = 1$ is the case shown in Fig. 3. These three zeroth order solutions can be identified in Figs. 4 and 5. Recall that the dimensionless growth rate is $\tilde{\gamma} \equiv \gamma\, r_s/v_s$. The scale time r_s/v_s, is a characteristic convection time for the ablative flow (although perhaps this time is a bit longer than is typical of flow through the ablation front because r_s is the full radius of the system). Consequently, solutions with $\tilde{\gamma} >> 1$ should not be greatly influenced by convection, while those with $\tilde{\gamma} << 1$ should be influenced by convection, in whatever way this influence expresses itself. It is interesting that there appears to be no qualitative change in the growth rate curves (see Fig. 6) from one side of $\tilde{\gamma} = 1$ to the other.

For larger ℓ, i.e., larger k, it is seen that ablative effects cause $\tilde{\gamma}$ to reach a maximum and then decrease to zero, instead of increasing indefinitely as classical, non-ablative inviscid, incompressible theory would predict. For smaller values of ℓ, it is seen from Fig. 6 that $\tilde{\gamma}$ becomes independent of $\tilde{g}$ and A and approximately proportional to ℓ. That $\tilde{\gamma}$ is approximately independent of A and $\tilde{g}$ for smaller ℓ is a consequence of the approximately linear dependence of A on $\tilde{g}$ for larger $\tilde{\rho}_p$ and $\tilde{g}$ (see Fig. 4). The

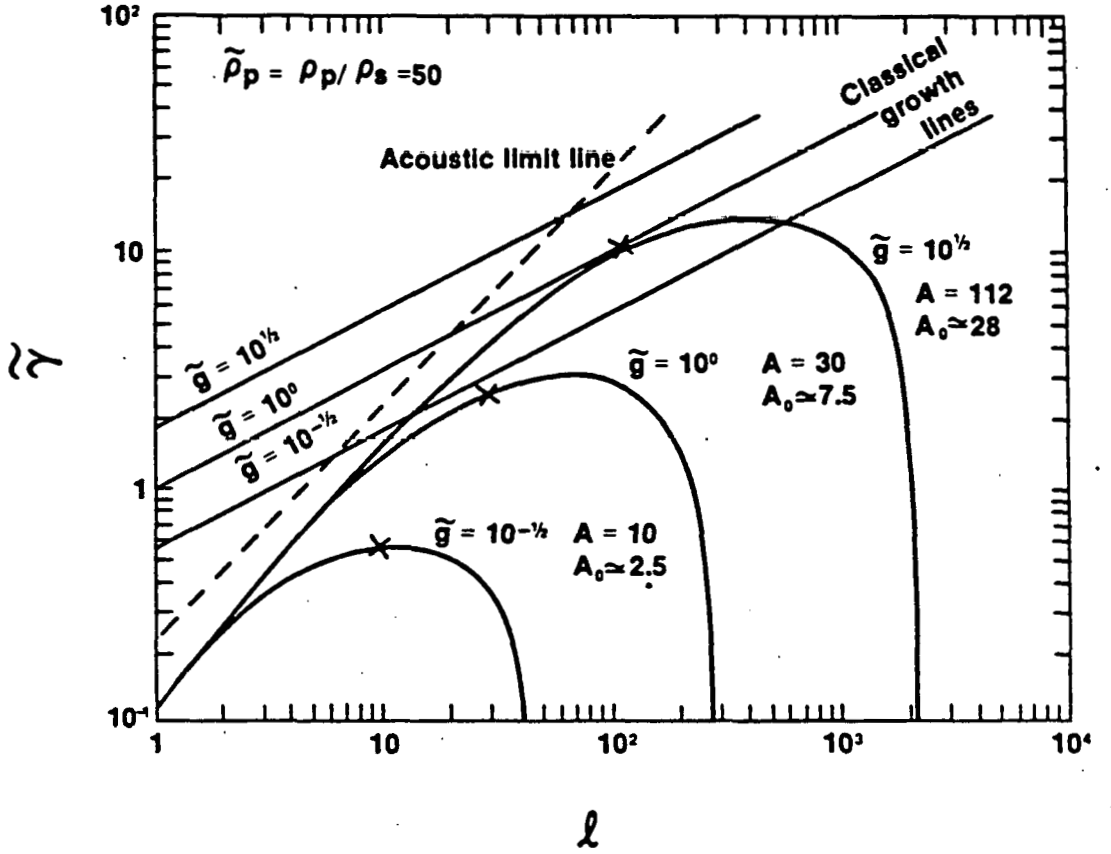

FIG. 6 Growth rates obtained for perturbation calculations performed for three stationary flow solutions with $\tilde{\rho}_p = 50$. The steady flow solution profiles for the $\tilde{g} = 1$ case are those of Fig. 3. The classic incompressible inviscid growth lines are given for the three cases; $\tilde{\gamma}(\text{classic}) = \sqrt{\ell \tilde{g}}$. The acoustic limit line, $\tilde{\gamma}(\text{limit}) = \ell\sqrt{.6(\tilde{g}/A)}$, is also shown. This line illustrates the effects of compressibility, important at low ℓ values, which is responsible for the large departure of the growth rates for these ℓ's from the classical value. The "worst case" ℓ values given by the approximate formula, $\ell = A$, are marked by crosses.

approximately linear relationship between $\tilde{\gamma}$ and ℓ seen in Fig. 6 is in approximate agreement with the equality in Eq. (12) and the limitation on $\tilde{\gamma}$ imposed by the acoustic transit time. Recall that for $\ell \gg 1$, $k \simeq \ell/r$. When numerical values from Fig. 4 are substituted into Eq. (12), the acoustic limit line of Fig. 6 is obtained. It is seen that $\tilde{\gamma}$ nowhere exceeds this limit but lies rather close to it for small ℓ, where it also appears that ablative effects have not significantly reduced $\tilde{\gamma}$. On the other hand, for these smaller values of ℓ, and therefore k, $\tilde{\gamma}$ lies far below the incompressible value given by Eq. (2), which further

indicates that compressibility is determining the growth rates for small values of ℓ. An additional effect, not treated in the above argument, occurs for small values of ℓ: $k \sim \ell/r$ is not applicable, because the wavelength of the mode is no longer small compared to the radius of the shell, and curvature effects must be considered. The lines with slope 1/2 on Fig. 6 are those given by Eq. (2) with $k = \ell/r_s$, for the different values of $\tilde{g}$. The "worst case" values of ℓ, at which $\ell = A$ are indicated in Figure 6. It is interesting that these classical "worst case" values of ℓ are quite close (within a factor of 2) to the values of ℓ at which the maxima of $\tilde{\gamma}$ occur. The values of these maxima $\tilde{\gamma}$ at these "worst case" values of ℓ are seen in all cases to be significantly less than the $\tilde{\gamma}$ one obtains from the classical estimate associated with that ℓ (see Fig. 6). From this result, we see it is possible to increase significantly the value of the lowest aspect ratio, A at which shell breakup should be expected to occur.

Figure 7 shows the form of the perturbed radial displacement

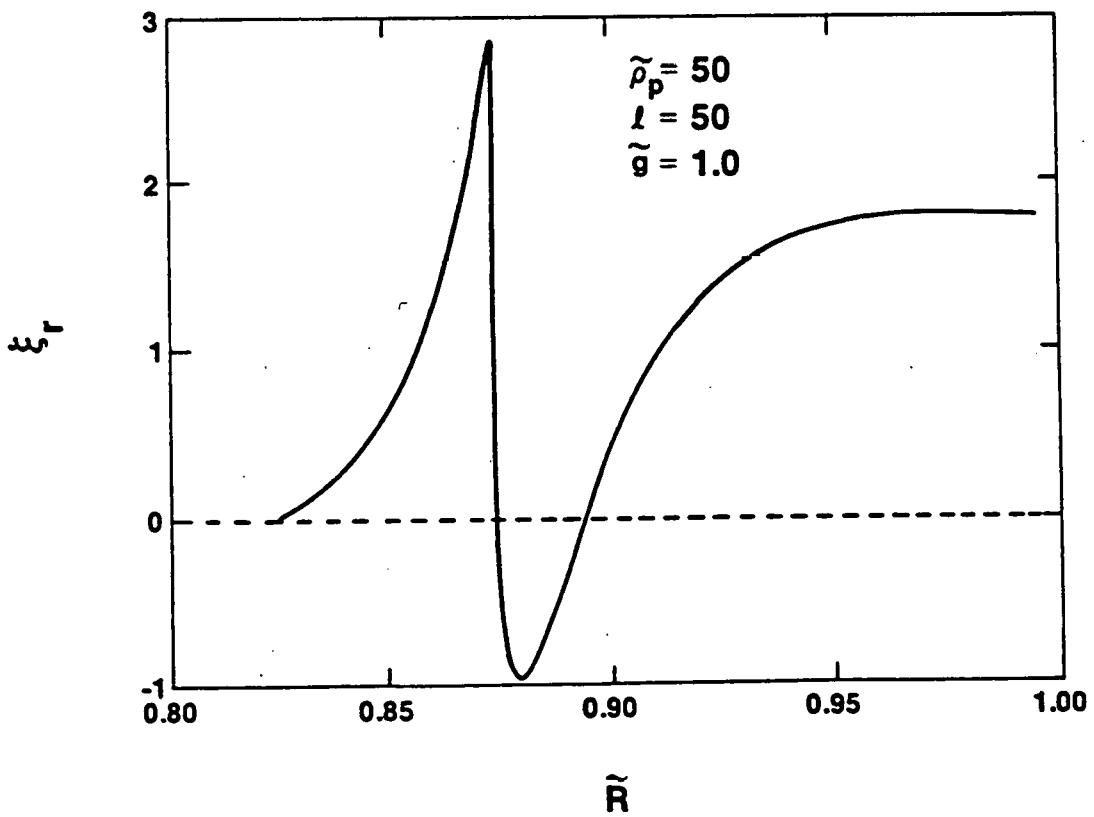

FIG. 7 Perturbed radial displacement ξ_r for the case $\tilde{\rho}_p = 50$, $\tilde{g} = 1$, and $\ell = 50$. This case has nearly the maximum growth rate (see Fig. 6). Note that ξ_r penetrates the shell to a depth $\sim \ell^{-1}$, and is extended by convection far into the exhaust region to the right.

ξ_r, for the case $\tilde{\rho}_p = 50$, $\tilde{g} = 1$, and $\ell = 50$. This case is seen from Fig. 6 to have approximately the maximum growth rate for $\tilde{g} = 1.0$ $\tilde{\rho}_p = 50$. It is seen that, as would be expected, the flow distortion, ξ_r, penetrates the shell to a depth of about k^{-1}, or ℓ^{-1}, and is extended by convection far into the exhaust or blow-off region to the right.

IV. NUMERICAL SIMULATION

In order to learn about nonlinear development of the ablation-driven Taylor instability, two-dimensional numerical simulations have been done. These have been done with a Langrangian hydrodynamic and heat-flow code named DAISY[19] which was written with triangular zones in order better to treat the highly distorted flows that occur during the large amplitude development of the instability.

It may be interesting to the reader to know that developing the numerical method for treating the heat flow was a much more challenging task than that presented by the hydrodynamics. The problem is that most of the schemes that come to mind give an inaccurate approximation to $\bar{\nabla}T$ when the shape of the zones are far from being equilateral triangles, and can even cause heat to flow "up hill" for some cases of highly irregular meshes. These problems also occur in codes employing quadrilateral zones, but only after the usually approximately rectilinear initial zoning has been distorted by the flow. In some ways, these problems are then more insidious in a quadrilateral code than they are in a triangular code in which many of the difficulties manifest themselves near the initialization time and therefore are more obvious. These additional difficulties encountered in a triangular code force one to devise a numerical scheme which, from the outset, gives an accurate approximation of ∇T, for highly irregular mesh configurations. The resulting method turns out to be more elaborate than those usually formulated for quadrilateral two-dimensional codes. The method that was developed to calculate heat flow on triangular grids has been found to be satisfactory for a variety of difficult (nonlinear) heat flow problems and was described in Ref. 19.

Initialization

The class of problems we have chosen for studying nonlinear development are flat slab targets which represent the limit of $A \to \infty$. In the context of the steady flow model discussed above this also corresponds to the limit $\tilde{g} \to \infty$. This limit was chosen for simplicity, because no particular finite aspect ratio seemed singularly interesting, and it is expected that almost all of the nonlinear ablative phenomena of interest should also be found to occur in the flat targets.

To initialize the two-dimensional code DAISY, an equivalent one-dimensional code is run until approximately steady accelerating ablative flow develops. The resulting one-dimensional temperature and density profiles are transferred to the two-dimensional code in a planar configuration; a perturbation is then applied that is localized near the ablation surface, and the two-dimensional simulation is begun. This procedure not only reduces the amount of computing required, but also minimizes certain types of transients[9,20] which can obscure interpretation when the problem is begun with a perturbation, and facilitates comparisons with the steady flow model.

The family of cases presented here was begun with a carbon slab 3 μm thick. Dimensionless, rather than physical variables, could have been used in this presentation of the two-dimensional results, but it was felt that representative physical values would make it easier for the reader to relate the cases presented to other experience with laser driven ablation. The absorbed laser irradiation has a constant value of 10^{15} w/cm^2 absorbed at a critical density of $ne_c = 10^{21}$ cm^{-3}. That is, we have assumed a step function pulse of 1.06μm light. Simulations with 2.5 and 5.0 x 10^{14} w/cm^2 have also been done and will be discussed elsewhere. Figure 8 shows a sequence of temperature and density profiles generated by the planar one-dimensional calculation. Transfer of the results to initialize the two-dimensional code was performed at 60 psec.

Results

In discussing these flat targets it is useful to use a burn through time, defined as

$$\tau_B \equiv \left(\frac{1}{M}\frac{dM}{dt}\right)^{-1} , \qquad (25)$$

because we no longer have an implosion time, τ_I from which to obtain the burn through parameter, B, discussed above. In practice, in order to maximize transfer of energy to kinetic energy of an imploding shell, one would choose $\tau_B \simeq \tau_I$, which is equivalent to $B \simeq 1$. In thinking about the relevance of flat target cases to spherical shells, it is therefore useful to think of τ_B as being equivalent in this sense to τ_I. A flat target is then more unstable (according to the classical theory discussed above), in the sense that the amplification of perturbations is larger, if in the time τ_B it accelerates through distances which are correspondingly greater multiples of its thickness.

From Fig. 8, it is seen that, if the slab remained planar, burn through would occur around 130 psec. when the peak density is beginning to decrease and the slab has moved about 25 μm from its

position at t = 0 or about 20 μm from its position at 60 psec. when initialization of the perturbation was performed. This latter distance of 20 μm is about 20 times the shell thickness at t = 60 psec. (about 1 μm). If we consider t = 60 psec. to be the beginning of the instability calculation then $\tau_B \approx 70$ psec.

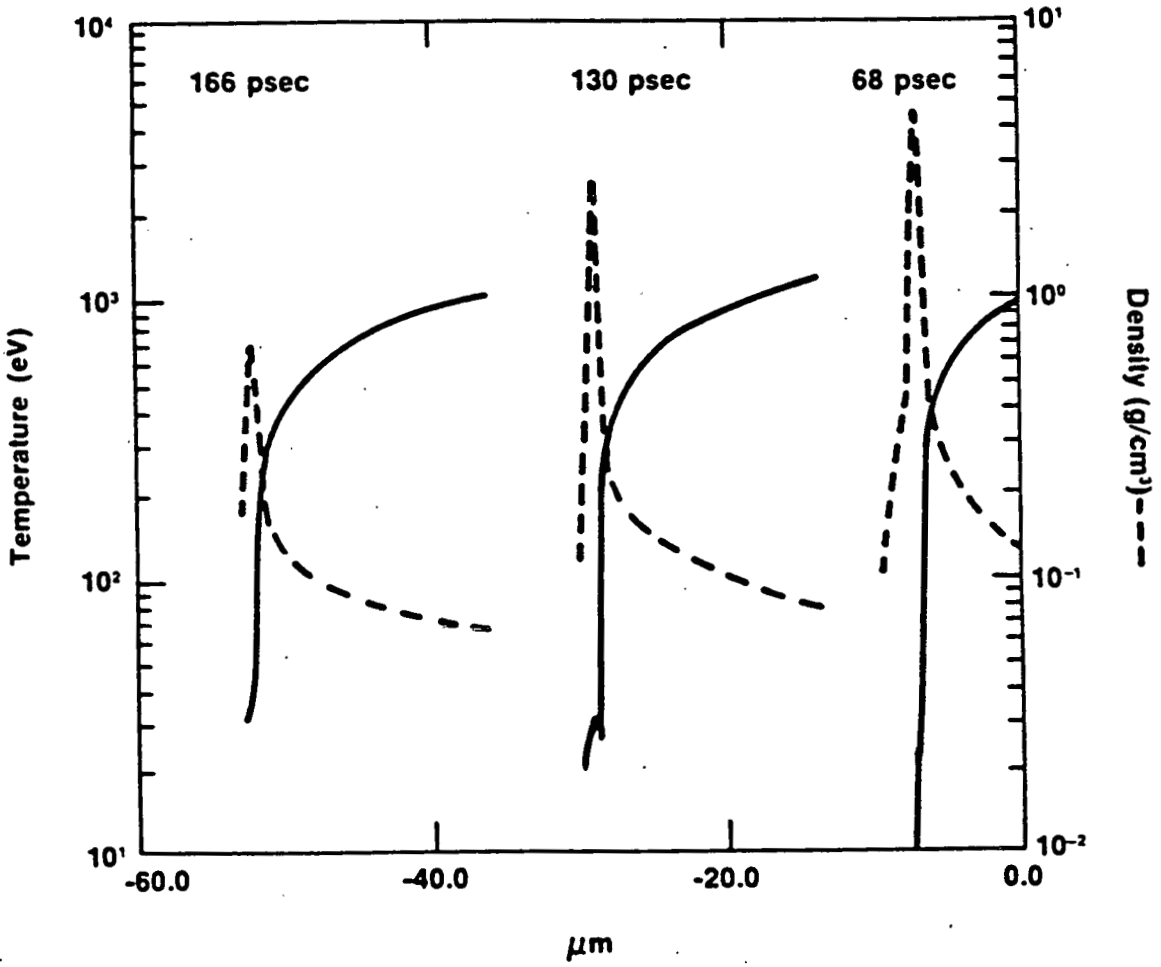

FIG. 8 A time sequence of temperature and density profiles generated by a one-dimensional planar simulation of the laser driven ablation of a 3 μm carbon slab. The laser irradiance, incident from the right, was 10^{15}W/cm^2.

The applied perturbation $\vec{\xi}$, is made to be incompressible by choosing it to have the form:

$$\vec{\xi} = \nabla \times \vec{A} \text{ , where } \vec{A} \text{ is a vector potential.} \qquad (26)$$

The problem is done in Cartesian geometry with the unperturbed target surface planes of y = constant, the laser is incident in the x-direction from the right, and the acceleration is in the negative x-direction. The form of $\bar{A}$ chosen is

$$A_x = 0 , \quad A_y = 0$$

$$A_z(x,y) = (\xi_0/k_y)\cos(k_y y)\,\mathrm{sech}[k_y(x-x_m)] , \qquad (27)$$

where k_y is the wave number of the mode in y, the coordinate parallel to the surface and X_m is the point of maximum density, which is approximately the left edge of the ablation front and where the density is almost discontinuous. For $|k_y(x-x_m)|>>1$ Eq. (27) has the standard form of the classic Taylor mode at a density discontinuity[1] and is a smooth function of x at smaller $|k_y(x-x_m)|$. Of the forms of A_z that have been used, Eq. (27) appears to be the most physical in the sense that for a given value of the initial amplitude number, $k_y\xi_0$ this form causes the least transient disturbance immediately after initialization.

Figure 9 shows the triangular grid at t = 60 psec. after initialization of a perturbation of the form given by Eq. (27) with $k_y\xi_0 = \pi/10$ and $k_y = 2\pi/(2.5 \times 10^{-4}$ cm). The two-dimensional computation is done in a region which is infinite in x and bounded by rigid slip surfaces in y. These surfaces are separated in y by one half wavelength of the perturbation, i.e. by a distance $\Delta y = \pi/k_y$.

Both in Fig. 9 and Fig. 10 discussed below we illustrate the results by showing one and one half wavelengths which are obtained by folding over (and thereby periodically reproducing) the computational grid two more times in the y direction to help visualize the results. That the mode being considered is a typical mode of interest can be seen from Figs. 9 and 10. The characteristic structure length of the mode is approximately equal to the shell thickness. This mode might, therefore, be expected to be capable of causing shell breakup, and moreover, at least to be in the range of the fastest growing mode capable of doing so. In fact the growth rates obtained from this simulation and others with different k_y's are in agreement with planar steady flow stability calculations and show this case to have a growth rate near the maximum for all modes, i.e. for all k_y. We illustrate this point below in Fig. 12. This mode, being both in the range of the fastest growing mode and of sufficiently long wavelength to cause breakup is, therefore, one of the most interesting cases to consider.

Figure 10 shows a sequence in time of grid plots from the simulation done with both the initial conditions and boundary conditions described above. In contrast with Fig. 9, only those grid lines ("i" lines in the DAISY calculation) are shown in Fig. 10 which

were initially in the plane of the unperturbed slab target and therefore, initially vertical. These lines show the distortion of the slab and are made easier to follow, at the expense of omitting some information, by omitting the other two families of grid lines.

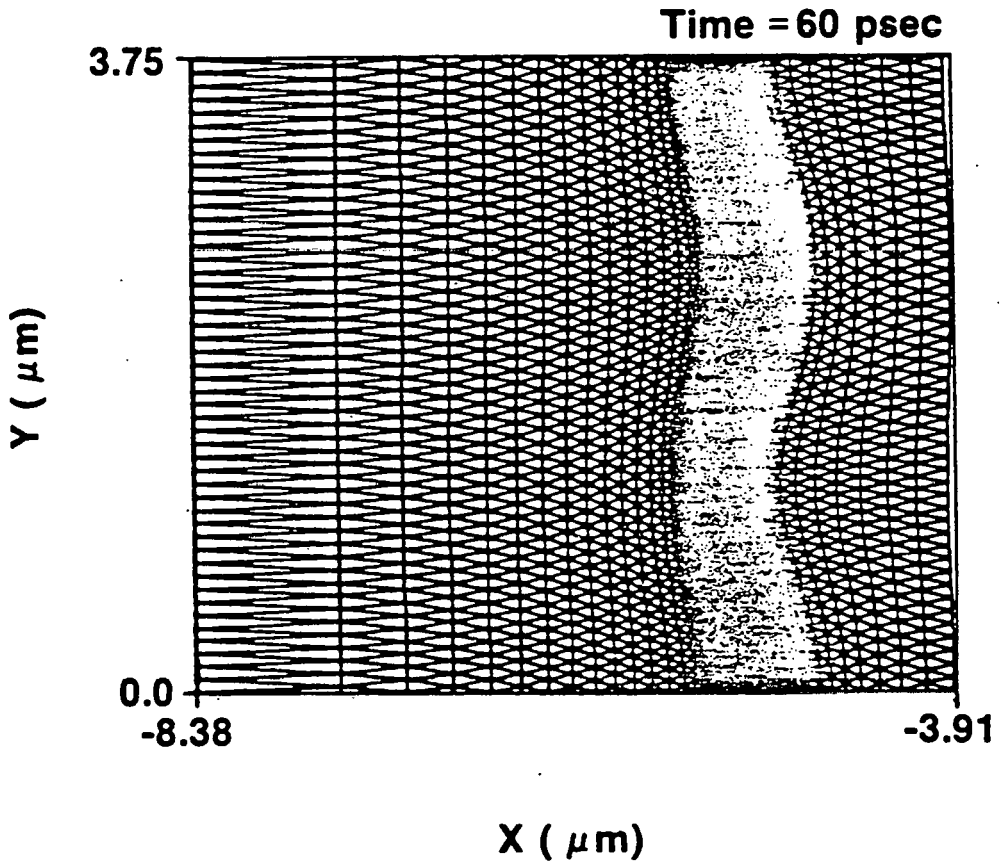

FIG. 9 Mesh plot from the two-dimensional Lagrangian hydrodynamic/heat-flow code DAISY. The mesh distortion illustrates the $k_y\xi_0 = \pi/10$ mode initialized at the shell surface for a 2.5 μm wavelength disturbance at t = 60 psec. The simulation involves approximately 4000 zones with a y-resolution of 72 points per wavelength.

As the amplitude of the distortion increases, its form is seen from Fig. 10 to resemble the bubble and spike structure seen in two-dimensional incompressible simulations of the classic Taylor instability.[8,9] The bubbles are relatively smoothly varying protrusions of the distorted shell to the left. The spikes are the pointed protrusions to the right, toward the incident laser beam and in the direction of the effective gravity and the ablative flow. In the nonlinear simulations of the classic instability, the spikes are seen to extend to the right until the fluid in the spike is essentially in free fall, and then continue to extend

indefinitely. Here we see a different behavior. The amplitude of the shell distortion, and in particular, the length of the spikes, does become of the order of k_y^{-1} or larger, certainly large enough to cause concern about loss of symmetry of the final compression of fuel in an implosion system. However, the spikes do not grow indefinitely. Instead, it appears that when the spikes have become sufficiently long and thin, heat flow ablates material from the tips sufficiently rapidly to prevent them from any larger growth. At the same time, as the amplitude increases, the rate of growth of the bubble-like structure also appears to decrease.

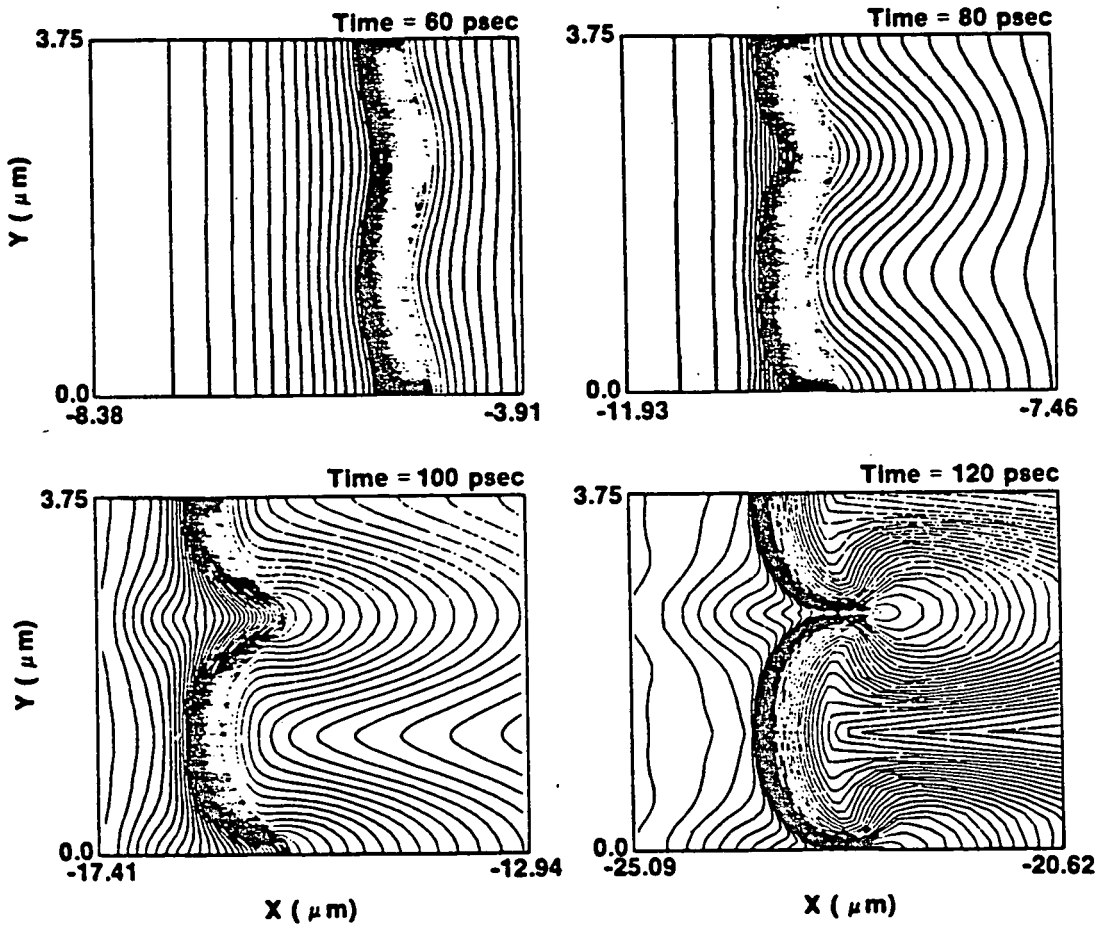

FIG. 10 Time evolution of the unstable 2.5 μm wavelength case (see Fig. 9) until burn through (t ≈ 130 psec.) from the DAISY simulation. The amount of mass between each line (i-line) is a constant throughout the calculation.

Some insight into the nonlinear development can be acquired from the RMS (root mean square) deviation of (initially vertical) grid lines (i-lines) shown in Fig. 10. This measure of distortion is

defined as

$$\langle \Delta x \rangle_i \equiv [\, (x_i - \langle x_i \rangle)^2 \,]^{\frac{1}{2}} , \qquad (28)$$

where i is the index of a grid line and the averages are taken over the position of the mass points in the i^{th} line. Figure 11 shows the time histories of these $\langle \Delta x \rangle_i$'s. Only a group of lines are shown which were near the ablation surface during the time of interest. At t = 60 psec. the largest value of $\langle \Delta x \rangle$ is seen to be 10^{-1} μm which is the RMS amplitude of the maximum of the initial perturbation described above. The line on Fig. 11 passing through 10^{-1} μm and at t = 60 psec. is, therefore, the time history of the grid line nearest the point of maximum density at this time. (Recall that the point of maximum perturbation, x_m, was chosen to coincide with the maximum density of the one-dimensional profile at initialization time.) All other grid lines have smaller $\langle \Delta x \rangle_i$ at this time. A dip is seen in the maximum $\langle \Delta x \rangle$ between 60 and 70 psec. which is caused by a transient response to imperfections in our assumed form of perturbation, Eq. (27). Introducing initial perturbations of velocity as well as density would probably be more nearly correct and reduce this transient effect, and will be tried in future simulations. The behavior in which we are interested begins at about 70 psec.

In Fig. 11 can be seen a locus of inflection points of the time history curves, which has been shaded to call attention to it. Each curve passes through this inflection as the grid line to which it corresponds passes through the ablation surface. This inflection, or change in slope, occurs because the rate of change of $\langle \Delta x \rangle$ is greater on the downstream side of the ablation surface. This can be understood from Fig. 10 where it is seen that the largest distortions occur on the right of the ablation surface, particularly near the tip of the spikes where the ablation rate is greatest. The large flow velocity of the low density ablated material convects it rapidly through this region of large and changing distortion and, therefore, causes a larger rate of change of $\langle \Delta x \rangle$ for a given i grid line than that same i-line experiences on the higher density upstream side of the ablation surface. All points on an i-line do not pass through the ablation surface at the same time, but the times of passage, particularly in the tip region, are near enough to being simultaneous to give the clear inflections that are seen. This locus of inflections in Fig. 11 is, therefore, the history of the amplitude of distortion of the ablation surface. In addition, the slope of the locus of inflection points on this log-linear graph gives, therefore, the growth rate of the instability. The curves below the ablation surface locus at anytime after 70 psec. correspond to i-lines that are interior to the dense shell material that has not yet been ablated. The slopes of these curves are slightly greater than the slope of the ablation surface locus, because the corresponding i-lines are being convected toward the ablation surface where distortion is greater,

as well as experiencing the local rate of growth of the mode. That is, there is a convective as well as a local growth contribution to the growth rate of $\langle \Delta x \rangle_i$ in the frame of a given i-line.

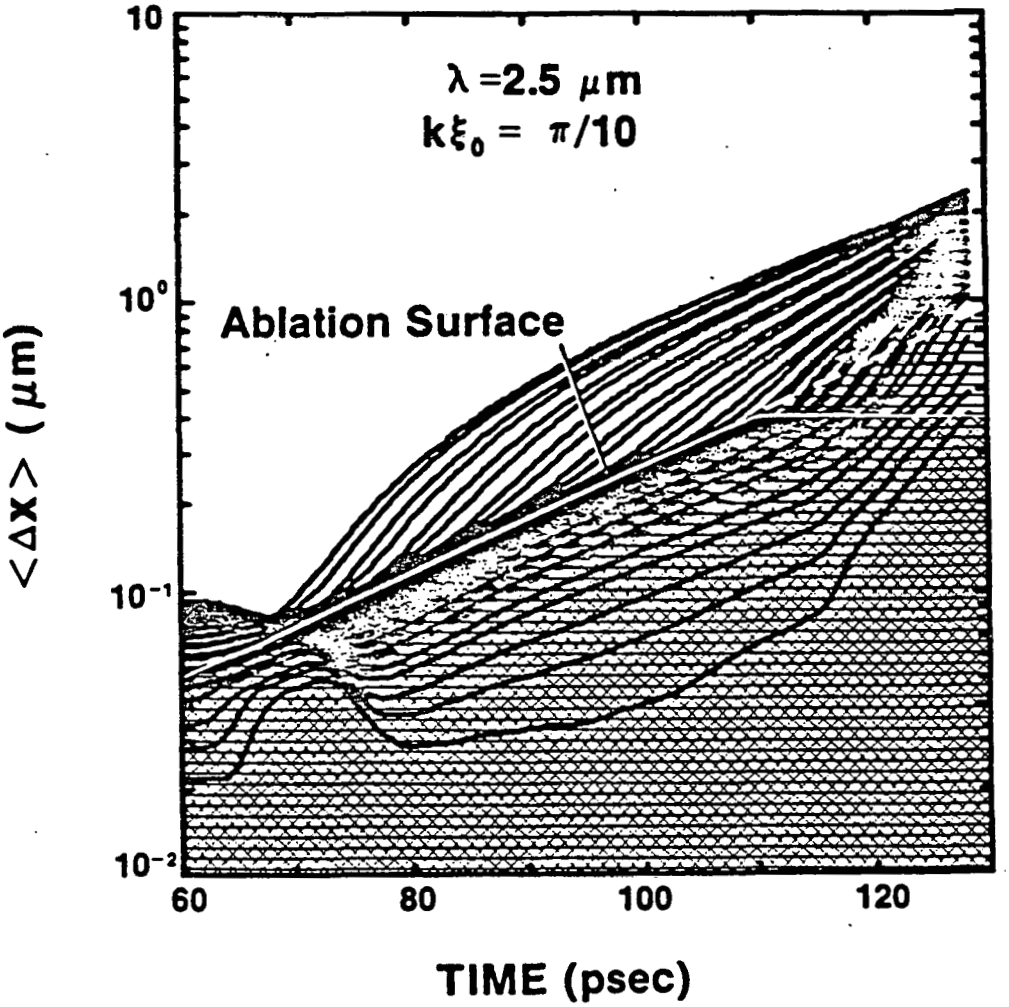

FIG. 11. Time history of the RMS distortion ($\langle \Delta x \rangle$) for various DAISY Langrangian markers (i-lines). Each curve shows a change of slope (inflection) as the grid i-line to which it corresponds passes through the ablation surface. The locus of these inflection points corresponds to the ablation surface time history. The decrease in the growth rate due to saturation accounts for the change in slope of the ablation surface line near t ≈ 110 psec.

Figure 12 shows growth rates for different values of k_y obtained from the slope of the ablation front locus from a set of simulation runs. These runs were done with a small initial amplitude, $k_y\xi_0 = \pi/50$, so that the mode growth would be in the linear regime. To identify the case shown in Figs. 9 and 10 on this graph, recall

that k_y of the initial perturbation in that case is $k_y = 2\pi/(2.5 \times 10^{-4}\,\text{cm}) \approx .25 \times 10^5\ \text{cm}^{-1}$. For comparison with the simulation growth rates, linear growth rates calculated with the planar stationary ablative flow model are also shown for two values of $\tilde{\rho}_p$ ($\equiv \rho_p/\rho_s$, see section III); viz. $\tilde{\rho}_p = 27$ and $\tilde{\rho}_p = 50$. These values of the density ratio $\tilde{\rho}_p$ approximately bracket the values seen in the one-dimensional simulation at the initialization time, t = 60 psec. The agreement between the growth rates obtained these two different ways has given us some confidence in both techniques. It is seen from Fig. 12 that, as stated above, the linear growth rate of the mode $k_y \sim .25 \times 10^5\ \text{cm}^{-1}$, from which the run shown in Fig. 10 was initialized, is near the maximum. From Fig. 12 and the one-dimensional burn through time (Eq. (25)), $\tau_B \approx 70$ psec, obtained above, it can also be seen that $\gamma\tau_B \approx 3$ for this mode.

At approximately 100 psec. in Fig. 11 it can be seen that the slope of the ablation surface begins to decrease and is almost horizontal by 120 psec.: that is, by 120 psec. the RMS distortion of the shell near the ablation surface is no longer growing. This behavior corresponds to the indications of saturation seen above in Fig. 10. Of course, the mode cannot become completely stationary because of ablative removal of mass from the shell. Similar saturation behavior has been seen for other values of k_y and $\gamma\tau_B$, including larger values of both.

Conclusions

The quasi stationary form that the Taylor mode is seen to have acquired in Fig. 10 discussed above is quite distorted and, therefore a potential source of disruption of the final fuel compression. However, at 120 psec. in Fig. 10, the side of the shell away from the laser, which would correspond to the inside of a spherical shell, is seen to be much less distorted than the outside. This only moderately distorted inner surface, while not as desirable as a perfectly flat (or spherical) surface, would probably not be mixed with lower density fuel inside it and might give somewhat better final fuel compression than would the inner surface of a shell that had clearly lost its integrity due to turbulent mixing.[3] It appears plausible that future successful high aspect ratio ICF implosion systems may, therefore, be designed to operate with shell distortions of the kind (and amplitude) like that illustrated in Fig. 10.

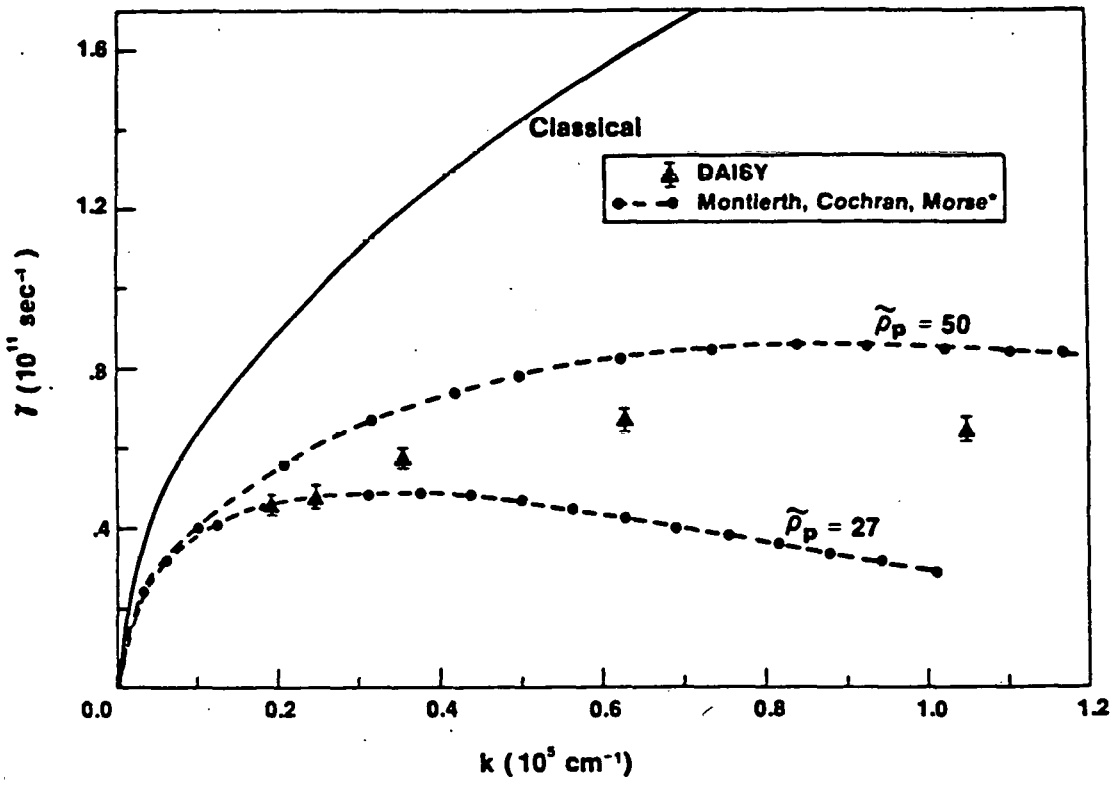

*(L. Montierth, F. L. Cochran, R. L. Morse, BAPS, 24 (1979), 945)

FIG. 12 Growth rate as a function of wave number for small initial amplitude ($k_y \xi_0 = \pi/50$) modes where linear theory is expected to hold. The DAISY simulations used an absorbed laser irradiance of 10^{15}W/cm^2 on a carbon slab. Observed simulation density profiles were approximately stationary in time with an observed ratio of ablation surface density to density at the isothermal sonic point of approximately 35. Note the agreement between the simulations and the perturbation results from the two parameter stationary ablative flow calculations which bracket our simulation results in this linear regime. The "classical" growth rate, $\gamma = \sqrt{ka}$, where the acceleration is determined from the simulation, is given for reference.

Acknowledgement

This work was partially supported by the following sponsors: Exxon Research and Engineering Company, General Electric Company, Northeast Utilities Service Company, the Standard Oil Company (SOHIO) and Empire State Electric Energy Research Corporation.

In addition, this work was also partially supported by the United States Department of Energy (USDOE).

Such support does not imply endorsement of the content of any of the above parties.

REFERENCES

1. S. Chandrasekhar, Hydrodynamic and Hydromagnetic Stability, Chapter X, 428 (Oxford: 1961).
2. G. Fraley, W. Gula, D. Henderson, R. McCrory, R. Malone, R. Mason, and R. Morse in Plasma Physics and Controlled Nuclear Fusion Research, 543, International Atomic Energy Agency (Vienna: 1974).
3. R. L. McCrory and R. L. Morse, Phys. Fluids 19, 175 (1976).
4. L. Montierth, F. L. Cochran, and R. L. Morse, Bulletin of the American Physical Society, 24, 945 (1979).
5. J. R. Freeman, M. J. Clauser, and S. L. Thompson, Nuc. Fusion 17, 223 (1977).
6. R. J. Mason, Nuc. Fusion 15, 1031 (1975).
7. J. D. Lindl, Lawrence Livermore Laboratories Report, UCRL-79735 (1979) unpublished.
8. B. J. Daly, Phys. Fluids, 10, 297 (1967).
9. F. H. Harlow and J. E. Welch, Phys. Fluids 9, 842 (1966).
10. G. Birkhoff, Los Alamos Scientific Laboratory Report LA-1862 (1955) and LA-1927 (1956) unpublished.
11. S. E. Bodner, Phys. Rev. Lett., 33, 761 (1974).
12. D. B. Henderson and R. L. Morse, Phys. Rev. Lett., 32, 355 (1973); see also J. N. Shiau, E. B. Goldman, and C. I. Wong, Phys. Rev. Lett., 32, 352 (1973).
13. D. B. Henderson, R. L. McCrory, and R. L. Morse, Phys. Rev. Lett. 33, 205 (1974).
14. R. L. McCrory, R. L. Morse, and K. A. Taggart, Nuc. Sci. Eng. 64, 163 (1977).
15. S. J. Gitomer, R. L. Morse, and B. S. Newberger, Phys. Fluids 12, 234 (1977).
16. L. Montierth, F. L. Cochran and R. L. Morse, Bulletin of the American Physical Society, 24, 945 (1979).
17. L. Spitzer, Physics of Fully Ionized Gases, Interscience (Princeton: 1961).
18. K. A. Brueckner, Siebe Jorna, Rev. Mod. Phys. 46, 325 (1974).
19. C. P. Verdon, R. L. McCrory, and R. L. Morse, Bulletin of the American Physical Society, 24, 945 (1979) and R. L. McCrory, R. L. Morse, and C. P. Verdon, Bulletin of the American Physical Society, 24, 945 (1979).

L. A. Elliott, Proc. Roy. Soc. A, 284, 397 (1965).